Master Thesis

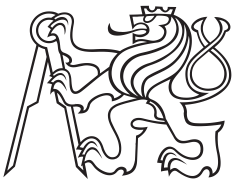

Czech Technical University in Prague

F4

Faculty of Nuclear Sciences and Physical Engineering
Department of Physics

Structure of the lunar wake with alpha particles not neglected in the solar wind

Bc. Daniel Procházka

Supervisor: Dr. Ing. Pavel Trávníček
January 2023

ČESKÉ VYSOKÉ UČENÍ TECHNICKÉ V PRAZE
FAKULTA JADERNÁ A FYZIKÁLNĚ INŽENÝRSKÁ
PRAHA 1 - STARÉ MĚSTO, BŘEHOVÁ 7 - PSČ 115 19

Katedra: fyziky *Akademický rok:* 2021/2022

ZADÁNÍ DIPLOMOVÉ PRÁCE

Student: Bc. Daniel Procházka

Studijní program: Aplikace přírodních věd

Obor: Fyzika a technika termojaderné fúze

Název práce: (česky) Struktura lunárního chvostu bez zanedbání přítomnosti alfa částic ve slunečním větru

Název práce: (anglicky) Structure of the lunar wake with alpha particles not neglected in the solar wind

Pokyny pro vypracování:

Cílem práce je zkoumat:

1) Vliv rychlosti vzájemného driftu protonů a alfa částic ve slunečním větru na strukturu lunárního chvostu

2) Vliv teplotní anizotropie iontů na vznik nestabilit a jejich šíření v lunárním chvostu a jeho okolí

3) Vliv vodivosti měsíčního jádra na vlastnosti a strukturu chvostu za přítomnosti dvou iontových spécií

Doporučená literatura:

[1] W. Baumjohann and R. A. Treumann: Basic space plasma physics. Imperial College Press, 2006

[2] R. A. Treumann and W. Baumjohann: Advanced space plasma physics. Imperial College Press, 2001

[3] H. Zhang et al.: Three-dimensional lunar wake reconstructed from ARTEMIS data. J. of Geophys. Res. Space Phys. 119, 5220 (2014)

[4] L. Gomberoff and J. A. Valdivia: Ion cyclotron instability due to the thermal anisotropy of drifting ion species. J. Geophys. Res. Space Phys. 108, A1 (2003)

Jméno a pracoviště vedoucího diplomové práce:

Dr. Ing. Pavel Trávníček, Ústav fyziky atmosféry AV ČR, v.v.i.

Datum zadání diplomové práce: 20.10.2021

Termín odevzdání diplomové práce: 02.05.2022

Doba platnosti zadání je dva roky od data zadání.

.....
garant oboru

.....
vedoucí katedry

ČESKÉ VYSOKÉ UČENÍ TECHNICKÉ V PRAZE
Fakulta jaderná a fyzikálně inženýrská
-1-

.....
děkan

V Praze dne 20.10.2021

Acknowledgements

I thank my supervisor, Dr. Ing. Pavel Trávníček, for the supportive supervision of this thesis and for his providing of the STW simulation library, without which this would not be possible.

I also acknowledge the use of NASA/GSFC's Space Physics Data Facility's OMNIWeb service, and OMNI data.

Declaration

Prohlašuji, že jsem svou diplomovou práci vypracoval samostatně a použil jsem pouze podklady (literaturu, projekty, SW, atd.) uvedené v přiloženém seznamu.

Nemám závažný důvod proti použití tohoto školního díla ve smyslu §60 Zákona č. 121/2000 Sb., o právu autorském, o právech souvisejících s právem autorským a o změně některých zákonů (autorský zákon).

V Praze dne 5. ledna 2023

Bc. Daniel Procházka

Abstract

The effect of alpha particle presence in the solar wind interaction with the Moon was investigated using a 2.5 dimensional hybrid model. The negligence of alpha particles does not have a strong effect on the general structure of the lunar wake. The alpha particle wake is highly assymetrical and affects the magnetic field in the lunar wake to a limited extent via diamagnetic currents. The introduction of alpha particle specie with typical solar wind parameters does not produce instabilities. A possible mirror mode instability was observed in the model of a two-specie lunar wake with high proton temperature anisotropy. The influence of the conducting lunar core in a two-specie wake with calm interplanetary magnetic field is negligible.

Keywords: solar wind, Moon, hybrid simulation, alpha particles

Supervisor: Dr. Ing. Pavel Trávníček
Ústav fyziky atmosféry AV ČR

Abstrakt

Vliv přítomnosti alfa částic ve slunečním větru v interakci s Měsícem byl zkoumán za využití 2.5dimenzionálního hybridního modelu. Zanedbání přítomnosti alfa částic nemá silný efekt na celkovou strukturu lunárního chvostu. Chvost tvořený alfa částicemi je vysoce asymetrický a v omezené míře ovlivňuje magnetické pole skrze diamagnetické proudy. V modelu lunárního chvostu za přítomnosti dvou spécií s vysokou protonovou teplotní anizotropií byla pozorována možná zrcadlová nestabilita. Vliv vodivého měsíčního jádra v lunárním cvhostu za přítomnosti dvou spécií s klidným meziplanetárním magnetickým polem je zanedbatelný.

Klíčová slova: sluneční vítr, Měsíc, hybridní simulace, alfa částice

Překlad názvu: Struktura lunárního chvostu bez zanedbání přítomnosti alfa částic ve slunečním větru

Contents

Figures

Tables

Chapter 1

Introduction

The solar wind is a plasma, a collection of fully ionized particles, blowing away from the Sun through the interplanetary space until it reaches a shockwave as it interacts with interstellar plasma [1]. On its way out from the solar system, the solar wind encounters planets, moons, asteroids, as well as human-made objects. The nature of the interaction of the solar wind with these objects depends on many factors, including the interplanetary magnetic field, particle density, bulk velocity, temperature and other plasma parameters, as well as the size, shape, and the atmospheric, surface, and subsurface constitution of these objects [1]. This thesis focuses on the interaction of the solar wind with the Moon. The interaction is modelled using a hybrid model, in which electrons in the plasma are treated as a massless fluid, and ions are simulated as mactroparticles. The primary aim of this thesis is to investigate the interaction via a hybrid model in which both hydrogen and helium ions are taken into account, because the hybrid models used to study the lunar wake typically omit the helium ions.

This chapter gives a brief overview of solar-wind interactions in Section 1.1 and the goals of this thesis in Section 1.2. Chapter 2 features a review of the solar wind, its properties (Section 2.1) and the waves (Section 2.2) and instabilities (Section 2.3) that are typical for the solar wind and may be encountered in the lunar wake; a review of literature on the composition of the Moon and its electromagnetic properties (Sections 2.5 and 2.6); a review of how the solar wind and Moon interact (Section 2.7) and a review of numerical modeling efforts (Section 2.8).

1.1 Solar-Wind and its Interaction with Planets and Moons

As the solar wind flows through the interplanetary space, it encounters planets, moons, comets, and dust particles. In order that the interaction of the solar wind with the Moon is understood in context, a brief overview of the basic types of interations is presented in the following section. The interactions share similarities that may help better understand the lunar wake formation and the lunar plasma environment – for example, the supersonic plasma flow

around magnetized asteroids is similar to the supersonic plasma flow around magnetized areas in the lunar crust – the so called *lunar crustal magnetic anomalies*.

In general, the nature of the interaciton between a planetary object and the surrounding plasma flow depends on the properties of both the body and the plasma. If the planet's magnetic field is sufficiently strong, it will counterbalance the pressure of the plasma flow and divert it, forming a so-called magnetosphere. A planet without a significant dynamo may still influence the plasma glow via remanent magnetization in the crust and electric currents induced in a conducting ionosphere, or a conducting layer, such as a metallic core, or a layer of water, as is the case with the icy moon Europa.

The bulk velocity of the solar wind exceeds the speed of the fast magnetosonic wave. However, it should be noted that interactions with subsonic plasma flow can be observed in the solar system as well – for example the Galielean moons that interact with Jupiter's magnetospheric plasma.

1.1.1 Magnetospheres

The *magnetosphere* is a region in space dominantly influenced by a planet's magnetic field. Figure 1.1 shows the typical magnetosphere that forms when a planet with a sufficiently strong dynamo is embedded in a supersonic plasma flow. Upstream the magnetosphere, a *bow shock* forms where the plasma is abruptly slowed down to subsonic velocity, diverted around the obstacle, and heated, as plasma instabilities dissipate the energy [1]. The bow shock is not static – its position depends on the momentum flux of the solar wind [1]. The area between the bow shock and the boundary of the magntosphere – a so-called *magnetopause* – is called the *magnetosheath*. The magnetopause largely acts as an impenetrable barrier between the solar wind and the magnetospheric plasma [1]. The interaction region extends for hundreds of planetary radii downstream the solar wind – this part is called the *magnetotail*.

The magnetospheric interaction depends mostly on the planet's magnetic dipole strength; and the density and bulk velocity of the solar wind. Table 1.1 shows these quantities for the magnetospheres of solar system planets – Mercury, Earth, Jupiter, Saturn, Uranus, and Neptune. The gas gaints have strong magnetic fields, beacuse high pressures inside sustain a phase of hydrogen (so-called *metallic hydrogen*) with high electrical conductivity. This fact, combined with the weaker IMF at large radial distances from the Sun, is the reason why the magnetospheres of gas giants are so large compared to that of Earth. The magnetic fields of Venus and Mars are too small to support a magnetosphere, although there is evidence suggesting that both Venus and Mars did have a dynamo earlier in history.

The planetary magnetic field can be described as a linear combination of moments in a multipole expansion. In case of the magnetospheric interaction, only the dipole term plays a significant role – at this distance, the magnetic

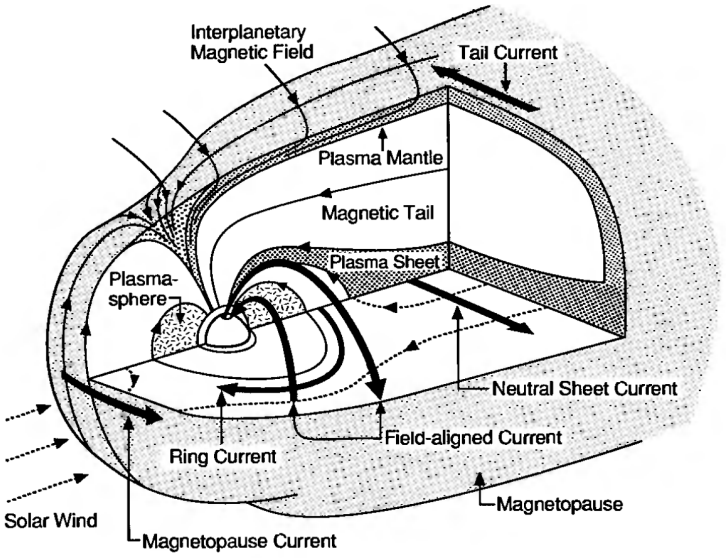

Figure 1.1: A schematic of the typical magnetosphere. Source: [1]

field is therefore

$$\mathbf{B}(\mathbf{r}) \approx \frac{3(\mathbf{M}\cdot\mathbf{r})\mathbf{r} - r^2\mathbf{M}}{r^5}, \tag{1.1}$$

where $\mathbf{M}$ is the dipole moment.

The size of the magnetosphere can be estimated as the distance of the pressure balance point where the pressure of the solar wind is balanced by the pressure of the planet's magnetic field. Neglecting thermal pressures of the solar wind and the magnetospheric plasma, the pressure of the solar wind is

$$p_{\mathrm{sw}} = \rho_{\mathrm{sw}} v_{\mathrm{sw}}^2, \tag{1.2}$$

where ρ_{sw} is the (mass) density of the solar wind and v_{sw} its bulk velocity; the pressure of the planetary magnetic field is

$$p_{\mathrm{mag}} = \frac{B^2}{2\mu_0}, \tag{1.3}$$

where $\mathbf{B}$ is the planetary magnetic field and μ_0 is the permittivity of free space. In the equatiorial plane, the dipole field strength is inversely proportional to the third power of radial distance r. Therefore, one can write

$$B(r) = B_0 \frac{R_{\mathrm{P}}^3}{r^3},$$

where R_P is the radius of the planet and B_0 is the magnitude of the magnetic field at the planet's surface. Thus, the pressure exerted by the planetary magnetic field on the solar wind flow depends on radial distance as

$$p_{\mathrm{mag}}(r) = \frac{B_0^2 R_{\mathrm{P}}^6}{2\mu_0 r^6}.$$

Planet	$\langle n_{\mathrm{SW}} \rangle / \mathrm{cm}^{-3}$	$\langle B_{\mathrm{IMF}} \rangle / \mathrm{nT}$	$\langle M \rangle / M_{\mathrm{E}}$
Mercury	53	41	5×10^{-4}
Earth	7	8	1
Jupiter	0.2	1	2×10^{4}
Saturn	0.07	0.6	600
Uranus	0.02	0.3	50
Neptune	0.006	0.2	25

Table 1.1: Select parameters of magnetospheres in the solar system

The estimate of the size of magnetosphere, also known as the *Chapman–Ferraro stagnation distance*, is therefore

$$R_{\mathrm{CF}} = \xi (B_0^2 / 2\mu_0 \rho_{\mathrm{sw}} v_{\mathrm{sw}}^2)^{1/6}, \tag{1.4}$$

where the dimensionless factor ξ corrects for the effects of magnetopausal current sheet. Empirically, $\xi \approx 1.4$ in Earth's case.

1.1.2 Induced Magnetospheres

Currents induced within a body or in its ionosphere by temporal changes in the direction and magnitude of the external magnetic field, may produce a so-called *induced magnetosphere*. The magnetic field produced by the induced electric currents are configured to prevent the external field from penetrating into the conductor. Inside the body, the induced electric current may flow in parts of the body or on the surface of conductors such as a molten metallic core or oceans (such as the one found under the surface of Jupiter's icy moon Europa). In the solar system, the induced magnetosphere is found at Venus, and at Titan, within Saturn's magnetosphere [2].

If the conductor is an ionosphere, the interaction is controlled not only by the external field, but also by the dynamic pressure of the incident plasma [1]. Similar to a magnetosphere, the induced magnetosphere is defined by the pressure balance of the incident plasma ($p_{\mathrm{ext}} = \sum_\alpha n_\alpha k_{\mathrm{B}} T_\alpha + \rho v^2 + B_{\mathrm{ext}}^2 / 2\mu_0$) and the ionosphere ($p_{\mathrm{i}} = \sum_\alpha n_\alpha k_{\mathrm{B}} T_\alpha + B_{\mathrm{ind}}^2 / 2\mu_0$). The concentration of ions in the ionosphere is enhanced by photoionization and therefore the ionospheric pressure will be the strongest above the dayside, which is facing the solar wind flow. However, unlike a classical magnetosphere, the boundaries of an induced magnetosphere are not as well defined. A definition proposed by *Luhmann et al.* is that an induced magnotosphere is everything between an outer boundary outside of which the obstacle has no effect on the external medium, and an inner boundary inside of which there is no effect of the external conditions [2].

The configuration of the magnetic field in fast plasma flows contains a magnetosheath and an induced magnetotail that is an extension of the magnetosheath into the wake. The magnetic field configuration and the plasma flow are displayed in a schematic in Figure 1.2. The magnetic field lines for a magnetic field perpendicular to the plasma flow will *drape* around

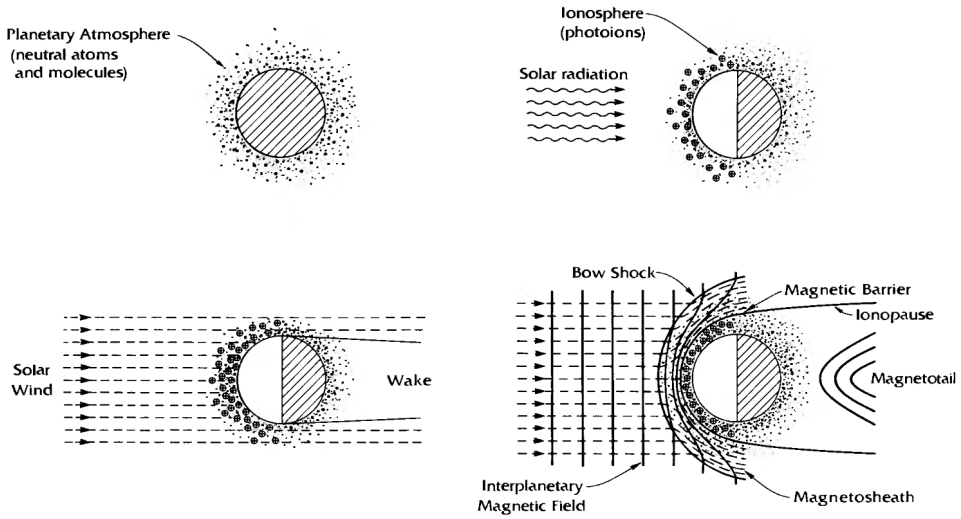

Figure 1.2: A schematic depicting the formation of an induced magnetosphere. Source: [1]

the obstacle. The existence of a bow shock upstream the body depends on the magnetosonic Mach number of the plasma flow, as well as ion pickup from the atmosphere of the obstalce, and the importance of finite-ion gyroradius effects. Mass loading by ion pickup slows the external plasma flow and therefore the bow shock need not form [2]. Ion pickup may also be the dominant process, in which case an induced magnetosphere will not form and the interaction looks different altogether – see the following section. The finite-ion gyroradius effects may prevent the formation of a magnetohydrodynamic shock if the magentosheath thickness is comprable to or less than the ion gyroradii [2]. The wake of the induced magnetosphere may tak the form of an induced magnetotail and/or an Alfven wing [2].

It was once thought that the Moon could produce an induced magentosphere in the solar wind. It has since been found out that the Moon does not have either a large enough conductivity, or a dense enough atmosphere (which would produced an ionosphere that would significantly influence the magnetic field) [2].

1.1.3 Magnetized Asteroids

Magnetized bodies with weak magnetization do not give rise to a magnetosphere when immersed in flowing plasma, but the interaction is still different from that with unmagnetized bodies. One case where this interaciton can be observed is when it comes to magetized asteroids interactig with the solar wind. The solar-wind interaction with magnetised asteroids has been analysed theoretically [3] and modelled both magnetohydrodynamically [4] and with the hybrid model [5], [6]. In the following paragraphs, I will discuss the hybrid model of this interaction.

When the solar wind interacts with a very weak magnetic dipole, a highly

anisotropic whistler wake emerges. It has a magnetic field signature but does not lead to a drop in density as whistler waves are non-compressional. As the magnetic dipole strength increases, additional fast and slow magnetosonic wakes form. They result in a rarefied (ion density drops to approximately a half) plasma tail with compression on its boundary. The angle of the wake wavefront depends on the Mach number of the solar wind. Upstream this compressional wave, there are additional perturbations of the magnetic field with a constant plasma density that are due to the whistler waves (which are non-compressional) [5].

For stronger magnetic dipoles, the fast magnetosonic wave dominates the interaction. The interaction region is more extensive and a shocklet structure appears upstream of the obstacle that is similar to the one appearing in hybrid models of solar wind interaction with unmagnetized planets with ionospheres. Plasma piles up on closed magnetic field lines of the dipole. The interaction is, however, different from a magnetospheric interaction due to the scales being comparable to proton inertial length. The fast magnetosonic shock upstream is due to this pile-up. Downstream, a region forms that is dominated by the dipole and is not accessible to the solar wind. This pressure gradient produces forces accelerating the plasma in a direction toward the center of the wake. Therefore, plasma velocity in the x-direction is enhanced in the central wake. In the case of the IMF antiparallel to the magnetic dipole, a belt forms that contains temporarily trapped ions. These ions are trapped on their Larmor trajectory as their gyroradii fit between the obstacle and the shock. For a perpendicular orientation of the IMF and the magnetic dipole, this belt does not form in the 3D hybrid simulations [5], [6].

In the case of an even stronger field, for which the distance of the pressure balance point from the obstacle is larger than typical plasma scales, a true magnetosphere forms. Simulations suggest that this is for the distance of the pressure balance point exceeding $\approx 20c/\omega_{\mathrm{p,i}}$. [5], [6]

1.1.4 Mass Loading

Mass loading is a phenomenon in which particles in the atmosphere of the interacting body (typically, a comet) are picked up by the plasma flow, which slows down as a result. In the simplest magnetohydrodynamic picture, the flowing plasma is contributed to by source terms – as particles are picked up, particles, mass, momentum, and energy are added to the flow [7]. In the cometary case, a cold gas consisting of heavy, almost-nonstreaming particles is added to the fast solar wind flow. Thus, only the mass source term is significant, hence, the term “mass loading”. The temperature change of the solar wind flow depends on the magnetosonic Mach number, the polytropic index, and the intensity of the mass loading. Mass loading of a supersonic flow leads to the heating of the flow (and its deceleration), while mass loading of a subsonic flow causes cooling (and acceleration) [7].

1.2 Thesis Goals

Due to its solar origin, the solar wind consists of mostly protons and electrons, with alpha particles being generally less than 10 % of the ions. It naturally follows that under certain circumstances, the omission of alpha particles from solar wind interaction models may be justfied. Indeed, when it comes to hybrid lunar wake models, oftentimes alpha particles are omittted. This thesis aims to investigate the efffect of alpha particle negligence in a lunar wake model and its justification via the means of a qualitative study. There are three effects which will be adressed:

1. the influence of the drift between protons and alpha particles in the solar wind on the structure of the lunar wake,
2. the influence of ion temperature anisotropy on the formation and propagation of instabilities in the lunar wake and its vicinity,
3. the influence of lunar core conductivity on the properties and structure of the lunar wake in the presence of two ion species.

These effects are studied via 2D simulations of the lunar wake, using an implementation of the CAM–CLL scheme for the hybrid model where electromagnetic field is approximated by a mesh, the protons and alpha particles are represented by macro-marticles moving in the simulation box, and electrons are approximated by a massless neutralizing fliud, also modeled as a mesh.

Chapter 2

Literature Review

2.1 Solar Wind Properties

The interplanetary space is filled with plasma of solar origin streaming outward from the Sun. This is due to coronal heating, as a result of which the Sun can not gravitationally contain its atmosphere, and so plasma streams out from the solar corona to the interplanetary space and farther, until it reaches a termination shock, where it becomes slower and denser as it interacts with interstellar plasma. This streaming plasma is called the *solar wind*. Much like the Sun, the solar wind consists mostly of ionized hydrogen (approx. 97 %) and helium (approx. 3 %), the vast majority of which is in the form of alpha particles; the typical helium-3 abundance is $(4.9 \pm 0.5) \times 10^{-4}$ relative to helium-4 [8]. The solar wind is a highly conducting fliud and as such, it carries a frozen-in magnetic field from the solar corona. This field is called the *interplanetary magnetic field* (IMF).

2.1.1 Characteristic Scales of the Solar Wind Plasma

Table 2.1 shows the typical values for the characteristic plasma scales in the solar wind at 1 au. It should be noted that these quantities are highly variable as are the solar wind properties – see Section 2.1.2. The importance of the values is mainly to illustrate which processes are relevant for interaction with the Moon, by comparing the characteristic spatial and temporal scales of the Moon, such as the lunar radius and the synodic month.

The collisional mean free path $\lambda_{\mathrm{mfp,p}}$, defined as the average distance a particle travels between two Coulomb collisions, is orders of magnitude larger than the typical timescale of any solar-wind interaction with a planet or a moon. For comparison, the size of Jupiter's magnetosphere (or, to be precise, the distance from the center of Jupiter to the magnetopause), the biggest magnetosphere in the solar system, is 30×10^5 km [1] – three orders of magnitude shorter than the collisional mean free path of solar-wind protons at 1 au. This means that for the purpose of its interactions with bodies in the solar system, the solar wind is a *collisionless plasma* – collisions play a negligible role.

Consider plasma consisting of electrons and mutliple ionic species $\alpha =$

Symbol	Parameter	Value
n_p, n_e	proton and electron number density	3 cm^{-3}
T_p, T_e	proton and electron temperature	10^5 K
B_IMF	interplanetary magnetic field	3 nT
$\lambda_\mathrm{mfp,p}$	proton collisional mean free path	3 au
d_p	proton inertial length	140 km
$r_\mathrm{g,p}$	proton gyroradius	160 km
d_e	electron inertial length (skin-depth)	3 km
$r_\mathrm{g,e}$	electron gyroradius	2 km
$\lambda_\mathrm{D,p}$, $\lambda_\mathrm{D,e}$	proton and electron Debye length	12 m
$\nu_\mathrm{c,p}^{-1}$	proton collision time	120 d
$2\pi \cdot \Omega_\mathrm{p}^{-1}$	proton gyration period	26 s
$2\pi \cdot \Omega_\mathrm{e}^{-1}$	electron gyration period	14 ms
$2\pi \cdot \omega_\mathrm{p,p}^{-1}$	proton plasma period	3 ms
$2\pi \cdot \omega_\mathrm{p,e}^{-1}$	electon plasma period	70 µs

Table 2.1: Typical plasma parameters (top), spatial scales (middle), and temporal sciales (bottom) in the solar wind at 1 au [9]

H, He, ..., each with a particle density n_α, where the particles belonging to that species have an electric charge q_α and a mass m_α. The *inertial length* of a species α is defined as

$$d_\alpha = \frac{c}{\omega_{\mathrm{p},\alpha}}, \tag{2.1}$$

where c is the speed of light in vacuum and $\omega_{\mathrm{p},\alpha}$ is the plasma frequency of the species α:

$$\omega_{\mathrm{p},\alpha}^2 = \frac{n_\alpha q_\alpha^2}{\epsilon_0 m_\alpha}.$$

For electrons, the inertial length is also known as *skin depth*. It is the characteristic length of the attenuation of the evansecent electromagnetic wave in plasma. In processes that occur on length scales greater than d_p, protons exhibit a so-called *magnetized behavior*, meaning that their trajectory is closely tied to the magnetic field lines [9].

The *gyroradius* (also known as *Larmor radius*) of a particle of species α,

$$r_{\mathrm{g},\alpha} = \frac{m_\alpha w_\perp}{|q_\alpha| B}, \tag{2.2}$$

where m_α is its mass, q_α its charge, and $w_\perp$ its thermal velocity perpendicular to the magnetic field $\mathbf{B}$, is relevant with respect to the so-called *finite gyroradius effects*. The difference in the scales of electron and ion motion is also the motivation to use plasma hybrid modeling. The lunar radius, $R_\mathrm{M} \approx 1740\,\mathrm{km}$ is somewhat comparable in scale to the typical solar-wind proton gyroradius, $r_\mathrm{g,p} \approx 160\,\mathrm{km}$, and thus it may be too much of a simplification to model solar wind protons as a fluid, whereas the electron gyroradius, $r_\mathrm{g,e} \approx 2\,\mathrm{km}$, is small enough with respect to the lunar radius for electron trajectories

to be neglected in the modeling. Therefore many models of the solar-wind interaction with the Moon have treated electrons as a fluid, while protons are treated as particles. See Section 2.8 for a review of hybrid models of the interaction, and chapter 3 for a more detailed description of hybrid modeling itself.

An important spatial scale with regards to electrostatic effects is the *Debye length*, defined as

$$\lambda_{\mathrm{D}\alpha} = \sqrt{\frac{k_{\mathrm{B}} T_\alpha}{4\pi n_\alpha q_\alpha^2}}, \tag{2.3}$$

where T_α is the temperature, n_α the number density, and q_α the electric charge of species α. The proton and electron Debye scales are similar throughout much of the heliosphere [9]. Taking into account the electron number density n_{e}, we see that the plasma parameter $\Lambda = n_e \lambda_{\mathrm{D}}^3 \gg 1$. Therefore, the solar wind, indeed, is a plasma.

2.1.2 Bulk Properties

Figure 2.1 shows the histograms of physical properties of the solar wind at 1 au measured from the start of 2010 until the end of 2021 by the hour. Listing top to bottom, left to right, the histograms are of the magnetic filed magnitude B, the magnetic field components B_x, B_y, B_z in geocentric solar ecliptic (GSE) coordinates[1], proton number density n, the alpha-to-proton number density ratio n_α/n_{p}, plasma speed v and plasma temperature T. The data used to plot these histograms is NASA/GSFC's hourly OMNI data set retreived through OMNIWeb [10].

Historically, solar wind has been classified into two categories based on the velocity of the plasma – slow solar wind and fast solar wind. The former is denser, slower, has a lower α/p ratio, and lower proton specific entropy than the latter. The measurements of solar wind properties are faced with the challenge of assesing the origin of the measured solar wind, for example recongizing coronal mass ejecta from normal solar wind. It has been suggested that the two-category classification of solar wind based on velocity is insufficient, and thus a classification based on solar wind plasma origin has been proposed [e.g. 11], [12]. The categories are coronal-hole plasma, streamer-belt plasma, and ejecta. Streamer-belt plasma can be subdivided into streamer-belt plasma and sector-reversal-region plasma. Coronal-hole plasma corresponds to fast solar wind, whereas streamer-belt plasma corresponds to slow solar wind [11] The type of plasma can be determined using its parameters such as Alfvén velocity v_A, proton specific entropy S_p, the ratio of abundance of oxygen ions $\mathrm{O}^{7+}/\mathrm{O}^{6+}$, and the ratio of expected and measured proton temperatures $T_{\mathrm{exp}}/T_{\mathrm{p}}$. There are several such categorization schemes [11], [12].

Table 2.2 shows the mean abundaces of helium, carbon, nitrogen, magnesium, silicon, sulfur, and iron, respectively, as ratios to oxygen abundance,

[1] the x axis is pointing toward the Sun and the z axis is perpedicular to the plane of the Earth's orbit around the Sun, facing north, y completes the right-handed system

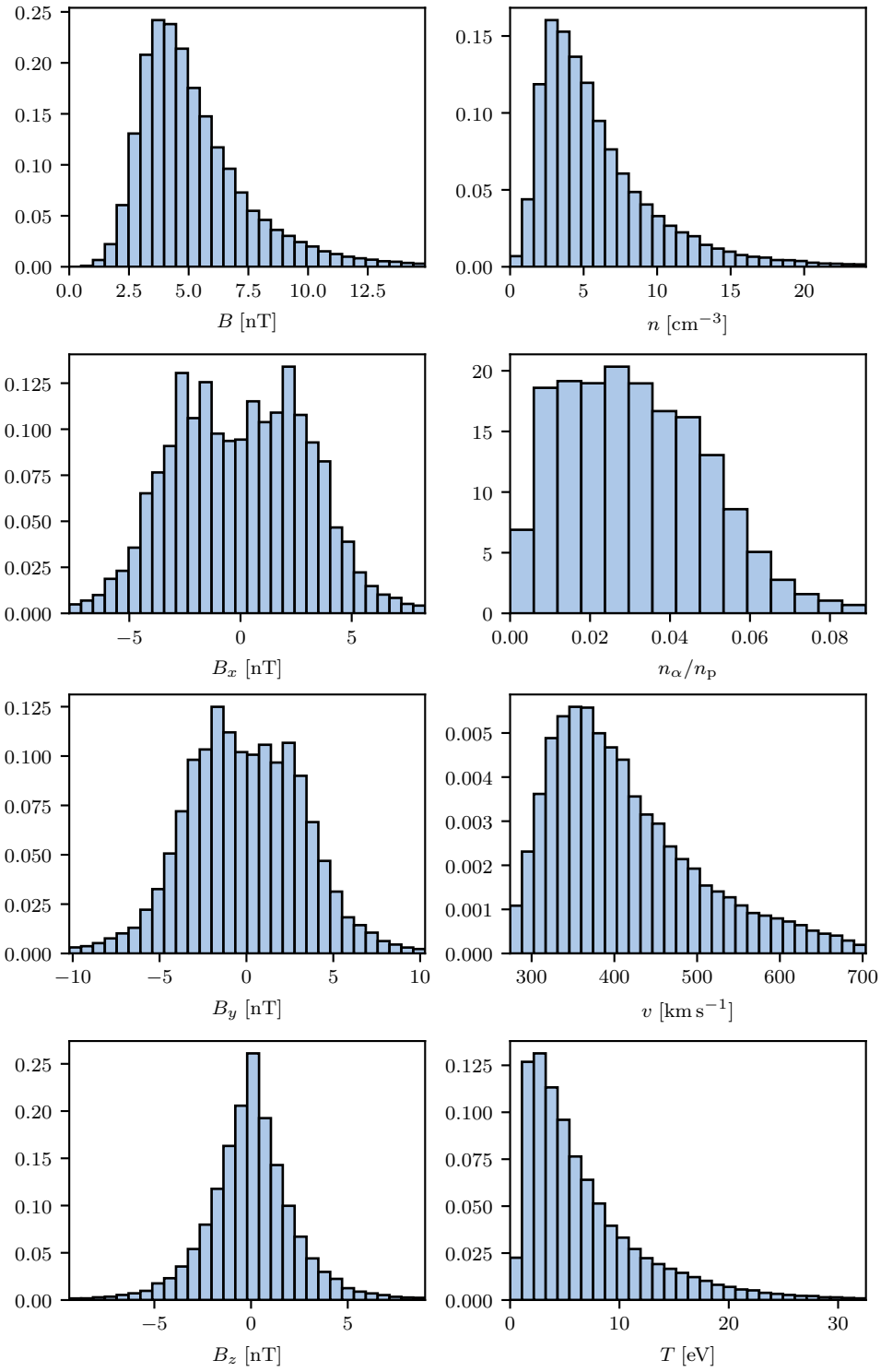

Figure 2.1: Histograms of solar wind magnetic-field magnitude B and its components B_x, B_y, B_z in the GSE coordinates, proton number density n, the alpha-to-proton number density ratio n_α/n_p, plasma speed v and temperature T

	IS	CH	CME	Bulk SW
He/O	77.0	84.0	93.3	83.2
C/O	0.672	0.702	0.625	0.672
N/O	0.139	0.154	0.138	0.145
Mg/O	0.131	0.118	0.200	0.141
Si/O	0.166	0.168	0.180	0.170
S/O	0.062	0.037	0.064	0.053
Fe/O	0.116	0.080	0.146	0.109
C^{6+}/C^{5+}	1.189	0.609	1.491	1.042
O^{7+}/O^{6+}	0.249	0.087	0.526	0.253
f_{FIP}	1.852	1.509	2.413	1.846

Table 2.2: Mean abundances and charge state ratios in different solar wind regimes from Genesis mission measurements [13].

and the charge state ratios of carbon ions C^{6+}/C^{5+} and oxygen ions O^{7+}/O^{6+} in the solar wind measured over a period of more than two years (2001 – 2004) in the Lagrange point L1. The data were gathered by the Genesis Ion Monitor onboard the Genesis spacecraft and the Solar-Wind Ion Composition Spectrometer on board the Advanced Composition Explorer. The data is categorized[2] by solar wind into: interstream plasma (or slow solar wind; IS), coronal hole plasma (or fast solar wind; CH), and coronal mass ejecta (CME) [13]. The error of the measurements is 20 % [13].

The ionic charge states reflect the electron temperature at the coronal source of the plasma at the *freeze-in point* where recombination time becomes greater than the characteristic expansion time-scale. Therefore, electron temperature at the freeze-in point, so-called *freeze-in temperature* can be indirectly measured by measuring the charge state ratios. [13]

2.1.3 Kinetic Properties

Assuming local thermodynamic equilibrium, the particles of the plasma would occupy the phase space $\{(\mathbf{x}, \mathbf{v})\}$ randomly with a Maxwell–Boltzmann distribution. A particle of the species α with a given number density $n_\alpha(\mathbf{x})$, bulk velocity $\mathbf{U}_\alpha(\mathbf{x})$), and temperature $T_\alpha(\mathbf{x})$ would have the following phase space distribution

$$f_\alpha^{(\mathrm{M-B})}(\mathbf{x}, \mathbf{v}) = \frac{n_\alpha(\mathbf{x})}{(2\pi)^{3/2} w_\alpha^3(\mathbf{x})} \exp\left(-\frac{(\mathbf{v} - \mathbf{U}_\alpha(\mathbf{x}))^2}{2w_\alpha(\mathbf{x})}\right), \tag{2.4}$$

where

$$w_\alpha(\mathbf{x}) = \sqrt{\frac{k_\mathrm{B} T_\alpha(\mathbf{x})}{m_\alpha}} \tag{2.5}$$

is the so-called *thermal velocity* of species α. The solar wind is, however, only a *weakly collisional* plasma since the mean free path is larger than the typical

[2] The SW regime was determined by a regime selection algoritm in real time from electron and ion spectrometer data gather in situ onboard the Genesis spacecraft. [13]

scales – see Section 2.1.1. This means that the collisions do relax the system back into thermodynamic equllibrium, and the local equilibrium distribution $f^{(\mathrm{M-B})}$, only very slowly. A generalized form of the Maxwell–Boltzmann distribution often used for plasma is the so-called *bi-Maxwellian* distribution, which introduces temperature anisotropy with respect to the magnetic field:

$$f_\alpha^{(\mathrm{bM})}(\mathbf{x},\mathbf{v}) = A^{(\mathrm{bM})}(\mathbf{x}) \exp\left(-\frac{v_\perp^2}{2w_{\perp,\alpha}^2(\mathbf{x})} - \frac{(v_\parallel - U_{\parallel,\alpha}(\mathbf{x}))^2}{2w_{\parallel,\alpha}(\mathbf{x})} \right), \tag{2.6}$$

where

$$A^{(\mathrm{bM})}(\mathbf{x}) = \frac{n_\alpha(\mathbf{x})}{(2\pi)^{3/2} w_{\parallel,\alpha}(\mathbf{x}) w_{\perp,\alpha}^2(\mathbf{x})}$$

and, analogously to the isotropic Maxwellian case, we define the paralell and perpendicular thermal velocities of species α as

$$w_{\parallel,\alpha}(\mathbf{x}) = \sqrt{\frac{k_\mathrm{B} T_{\parallel,\alpha}(\mathbf{x})}{m_\alpha}} \qquad \text{and} \qquad w_{\perp,\alpha}(\mathbf{x}) = \sqrt{\frac{k_\mathrm{B} T_{\perp,\alpha}(\mathbf{x})}{m_\alpha}}, \tag{2.7}$$

where $T_{\perp,\alpha}$ and $T_{\parallel,\alpha}$ are the temperatures perpendicular and parallel, respsectively, to the magnetic field lines.

Another generalization of the Maxwell–Boltzmann distribution is the κ-distribution:

$$f_\alpha^{(\kappa)}(\mathbf{x},\mathbf{v};\kappa) = A^{(\kappa)}(\mathbf{x}) \left[1 + \frac{1}{\kappa - \frac{3}{2}} \frac{(\mathbf{v} - \mathbf{U}_\alpha(\mathbf{x}))^2}{w_\alpha^2(\mathbf{x})} \right]^{-\kappa-1}, \tag{2.8}$$

where

$$A^{(\kappa)}(\mathbf{x}) = n_\alpha(\mathbf{x}) \left[\pi w_\alpha^2(\mathbf{x}) \left(\kappa - \frac{3}{2} \right) \right]^{-\frac{3}{2}} \frac{\Gamma(\kappa+1)}{\Gamma(\kappa - \frac{1}{2})},$$

$n_\alpha(\mathbf{x})$ and $U_{\parallel,\alpha}(\mathbf{x})$) are the number density and bulk velocity of species α, respectively, and $w_\alpha(\mathbf{x}) = \sqrt{k_\mathrm{B} T_{\parallel,\alpha}(\mathbf{x})/m_\alpha}$ is its thermal velocity [14]. The posisble values of the parameter kappa are $3/2 < \kappa < \infty$. For $\kappa \to \infty$, the kappa distribution is identical to Maxwell–Boltzmann distrbution, i.e. the system resides at thermal equilibrium. For $\kappa \to 3/2$, the system approaches the furthest state from equilibrium, called *anti-equlibrium* [14]. At anti-equilibrium, $\kappa \to 3/2$, the κ-disitribution turns into the power law, $f^{(\kappa)}(\mathbf{v}) \propto |\mathbf{v} - \mathbf{U}|^{-5}$ [14]. The κ-distribution may be generalized to the *bi-κ-distribution*, in a fashion similar to the bi-Maxwellian, to account for temperature anisotropies [9].

In-situ observations show that ion and electron distributions in the solar wind deviate from the Maxwell–Boltzman or bi-Maxwellian distributions. Firstly, protons show temperature anisotropy with respect to the magnetic field [9]. Solar wind protons consist of two populations: the *proton core* and the *proton beam*. Majority of solar wind protons belong to the core. The proton beam is streaming faster than the proton core parallel to the magnetic field lines with a relative speed greater than the proton alfvén velocity [15]. The differential flow speed of the proton beam depends on the Coulomb

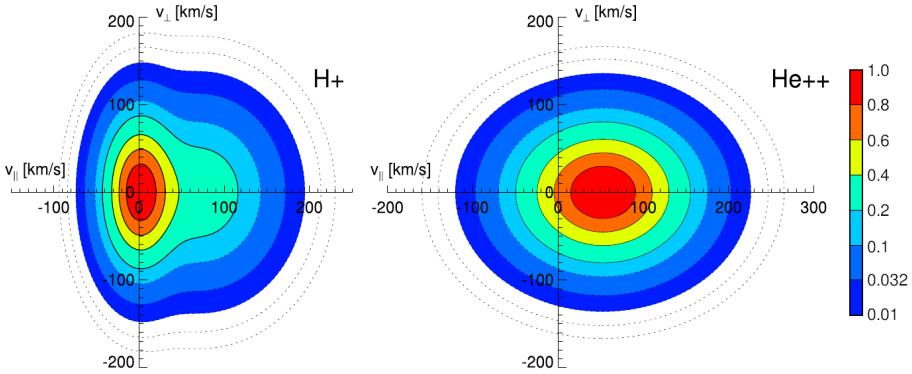

Figure 2.2: Ion velocity distribution functions in the solar wind. Source: **alterman2018** (edited).

collision rate, proton pressure anisotropy, and the alfvén velocity. For solar wind at 1 au, which is approximately collisionless, the drift velocity of the proton beam is $\Delta v_{\mathrm{pb}} = 1.06 \pm 0.15 v_{\mathrm{A}}$, where v_{A} is the local alfvénic velocity [15]. Proton temperature anisotropy is weakly dependent on the parallel beta of protons due to instabilities, which provide constraints on this relation – see Section 2.3. The instabilities define a stable area in $(T_\perp/T_\parallel, \beta_\parallel)$-space [16]. The 2D histogram of the distribution of solar wind protons in this space as measured by Wind/SWE is featured in Figure 2.3.

The alpha particles in the solar wind also show a differential flow with respect to the proton core. The α/p drift however, is slower than the drift of the proton beam [15]. In the solar wind at 1 au, the alpha particle drift is $\Delta v_\alpha = 0.62 \pm 0.13 v_{\mathrm{A}}$ [15]. In the perfectly collisionless limit, this value was extrapolated to

$$\Delta v_\alpha = 0.67 \pm 0.09 v_{\mathrm{A}}. \tag{2.9}$$

Another signature of the non-equilibrium of the solar wind is the so-called *anisothermal behavior*. Its a phenomenon where plasma species have different temperatures [9]. Alpha particles in the solar wind often have larger parallel temperature than protons. In-situ measurements showed $T_{\parallel,\alpha} \gtrapprox 4T_{\parallel,\mathrm{p}}$ [9], [18].

Solar wind electrons also consist of disctinct populations. There are three electron components in the solar wind: the *electron core*, the *electron halo*, and the *strahl*. The electron core is mostly bi-Maxwellian. It has however been suggested that a *self-similar distribution* might describe the core better [19]. The distribution function of the self-similar distribution is:

$$f^{(\mathrm{ss})}(\mathbf{x}, \mathbf{v}; s) = A^{(\mathrm{ss})}(\mathbf{x}) \exp\left[- \left(\frac{v_\parallel - U_\parallel(\mathbf{x})}{w_\parallel(\mathbf{x})} \right)^s - \left(\frac{v_\perp - U_\perp(\mathbf{x})}{w_\perp(\mathbf{x})} \right)^s \right], \tag{2.10}$$

where

$$A^{(\mathrm{ss})}(\mathbf{x}) = \left[2\Gamma\left(\frac{1+s}{s} \right) \right]^{-3} \frac{n(\mathbf{x})}{w_\perp^2(\mathbf{x}) w_\parallel(\mathbf{x})}.$$

Upon close inspection, one can notice that the self-similar distribution is, in fact, yet another generalization of the Maxwell–Boltzmann distribution. For

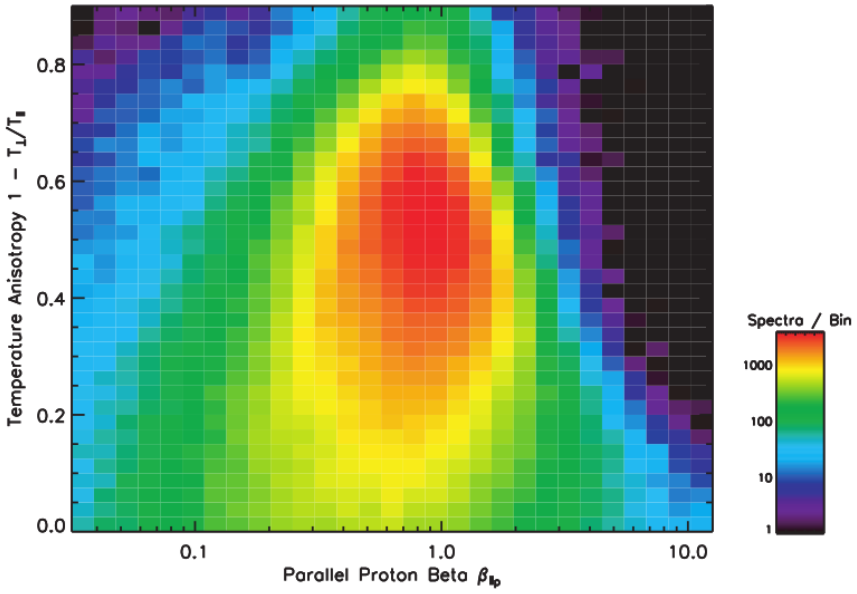

Figure 2.3: A histogram of solar wind protons as measured by Wind/SWE. The color shading of the bins is logarithmic. Source: [17].

$s = 2$, $f^{(\mathrm{ss})}$ is the bi-maxwellian distribution function. For interplanetary shocks, *Wilson et al.* have found the self-similar distribution with $2.0 \leq s \leq 2.05$ fit the electron core better than bi-maxwellian distribution [19].

The temperature of the electron halo and the electron strahl are higher than the temperature of the electron core. That is why the halo and strahl are collectively reffered to as *superthermal electrons* [9]. The electron halo population follows a κ-distribution with $\kappa = 5.43$ at 1 au. As the distance from the Sun increases, the κ parameter decreases as well, as collisions relax the electrons closer to equilibrium [20]. The electron strahl is a field-aligned beam of electrons that typically drifts anti-Sunward relative to the solar wind, although a Sunward or bi-directional electron strahl can occur if the magnetic field configuration changes on the solar wind's trajectory from the Sun [9]. The ratio of superthermal electrons remains largely constant with increasing distance from the Sun, i.e. $(n_\mathrm{s} + n_\mathrm{h})/n_\mathrm{e}$, where n_s is the strahl number density, n_h the halo number density, and n_e the electron number density. However, with increasing distance from the Sun, $n_\mathrm{s}/n_\mathrm{e}$ decreases, while $n_\mathrm{h}/n_\mathrm{s}$ increases.

2.2 Waves in the Solar Wind

The understading of the waves and instabilities in the solar wind is important for a number of reasons. Waves and instabilities in the solar wind significantly influence its dynamics and thermodynamics in many ways: the heating and expansion of the solar wind, the angular momentum of the solar wind, the

solar wind thermal anisotropy, the heating and flow of alpha particles in the solar wind, and the fluid-like behavior of the solar wind [21]. For this reason, waves and instabilities need to be taken into account when modeling solar wind. For example, the expansion of the weakly collisional solar wind plasma was predicted by Parker to lead to large temperature anisotropies which are unstable to the growth of low-frequency magnetohydrodynmic modes – resulting in the so-called *firehose* instability (see 2.3.1).

Any perturbation δA of physical quantity A can be decomposed into its Fourier components:

$$\delta A(\mathbf{x}, t) = \int \mathrm{d}\omega \, \mathrm{d}\mathbf{k} \, \hat{A}(\mathbf{k}, \omega) \exp(\mathrm{i}\,\mathbf{k} \cdot \mathbf{x} - \mathrm{i}\,\omega t), \tag{2.11}$$

where ω is the frequency and $\mathbf{k}$ the wave vector of the component $\hat{A}$. In general $\omega \in \mathbb{C}, \mathbf{k} \in \mathbb{R}^3$. The imaginary part of frequency ω is important with regards to the damping or growth of the waves. Therefore we define the *growth rate* (or *damping rate*) as

$$\gamma = \mathrm{Im}\,\omega \tag{2.12}$$

There are three singificant damping mechanisms for plasma waves in the solar wind: *quasilinear diffusion* from wave-particle interactions, *nonlinear phase mixing*, and *stochastic heating* [9]. Dissipation in the sense of entropy generation can not occur in a collisionless plasma, because it requires particle-particle collisions.

Stochastic heating is a non-resonant energy diffusion process. It arises from fluctations on the gyroradius scale in space and larger-than-gyration-period in time in a constant background magnetic field $\mathbf{B}_0$. The fluctuations distort the helical trajectory of the particles. If the amplitude of the perturbation is so large that orbits become stochastic in the plane perpendicular to $\mathbf{B}_0$, the particles experience random increases and decreases in their kinetic energy, which leads to diffusion in $v_\perp$-space and thus, perpendicular heating. This process is consistent with the observed temperatures and drifts of solar-wind protons and minor ions [9]. It is a candidate process to explain ion heating in the direction perpendicular to $\mathbf{B}_0$ in weakly collisional plasmas. In high-β_p plasmas, the orbits become stochastic due to spatial variations in the magnetic field and the gain energy from the solenoidal component of the electric field. In low-β_p regime, the process is due to fluctuations in the electrostatic potential [9].

2.2.1 Alfvén Waves

Alfvén waves are non-compressive low-frequency waves generated by the movement of ions in a magnetic field $\mathbf{B}_0$. Becuase the solar wind is highly conductive and only weakly collisional, large-scale Alfvén waves travel almost undamped. Alfvén waves obey the dispersion relation

$$\omega^2 = \frac{B_0^2}{\mu_0 \rho_\mathrm{i}} k_\parallel^2, \tag{2.13}$$

where $k_{\parallel}$ is the magnitude of the projection of the wave vector to the magnetic field $\mathbf{B}_0$, ρ_{i} is the mass density of ions, and μ_0 is the permeability of free space. The phase velocity of this wave is called the Alfvén velocity,

$$v_A = \frac{B_0}{\sqrt{\mu_0 \rho_{\mathrm{i}}}}. \tag{2.14}$$

The velocity and magnetic field fluctuations associated with an Alfvén wave are either correlated or anti-correlated [21]:

$$|\delta \mathbf{B}|/B_0 = |\delta \mathbf{v}|/v_{\mathrm{A}}, \tag{2.15}$$

where B_0 is the amplitude of the unperturbed magnetic field and v_{A} is the Alfvén velocity. This fact is used to detect Alfvén wavse in the solar wind.

Alfvén waves can be extended to smaller scales. There are two such extensions – the kinetic Alfvén waves nad the Alfvén/ion-cyclotron waves, which shall be discussed in the following sections.

2.2.2 Kintetic Alfvén Waves

Kinetic Alfvén waves (KAWs) are the short-wavelength extension of the Alfvén branch for $k_{\perp} \gg k_{\parallel}$. They play a significant role in large-scale turbulance in the solar wind turbulence cascade. For $k_{\perp}\rho_{\mathrm{p}} \gtrapprox 1$, proton finite gyroradius effects modify the properties of the wave. In that case, the dispersion relation is given by

$$\omega^2 = \frac{k_{\parallel}^2 k_{\perp}^2 v_{\mathrm{A}}^2 \rho_{\mathrm{p}}^2}{\beta_{\mathrm{p}} + \frac{2}{1+T_{\mathrm{e}}/T_{\mathrm{p}}}} \tag{2.16}$$

where $k_{\parallel}$ and $k_{\perp}$ are the magntiudes of the projection of the wave vector parallel and perpendicular, respectively, to the background magnetic field, β_{p} is the proton beta, ρ_{p} is the proton density, T_{e} is the electron temperature, and T_{p} is the proton temperature. KAWs are electromagnetic, elliptically right-hand polarized and have a frequency $< \Omega_{\mathrm{p}}$. Unlike large-scale Alfvén waves, KAWs are compressive – number density is perturbed by them [9].

2.2.3 Alfvén/Ion-Cyclotron Waves

Alfvén/ion-cyclotron (AIC) waves are the short-wavelength extension of the Alvén branch for $k_{\parallel} \gg k_{\perp}$. The anisotropic Alfvénic turbulent cascade on its own cannot generate AIC waves. AIC waves are responsible for the heating of ions in direction perpendicular to $\mathbf{B}_0$ via cyclotron resonance heating. In the cold-plasma limit, AIC waves converge to L-mode waves, with the dispersion relation

$$\frac{c^2 k^2}{\omega^2} = 1 - \frac{\omega_{\mathrm{p}}^2/\omega^2}{1 + \omega_{\mathrm{c}}/\omega}, \tag{2.17}$$

where ω_{c} is the ion cyclotron frequency, and ω_{p} is the plasma frequency [9].

2.2.4 Fast and Slow Modes

The slow mode is a major candidate to explain compressive fluctations in the solar wind [9]. The perturbations to velocity $\delta\mathbf{v}$ and magnetic field $\delta\mathbf{B}$ of the fast and slow modes are in the plane defined by $\mathbf{k}$, $\mathbf{B}_0$. [21]. In the MHD limit, the dispersion relation of the slow and fast modes is given by

$$\omega = C_- k \qquad \text{for the slow mode,} \tag{2.18a}$$

$$\omega = C_+ k \qquad \text{for the fast mode,} \tag{2.18b}$$

where

$$C_\pm^2 = v_\mathrm{A}^2 \left[\frac{1}{2}\left(1 + \frac{\kappa}{2}\beta_\mathrm{p}\right) \pm \frac{1}{2}\sqrt{\left(1 + \frac{\kappa}{2}\beta_\mathrm{p}\right)^2 - 2\kappa\beta_\mathrm{p}\cos^2\theta} \right], \tag{2.19}$$

where κ is the polytropic index and θ is the angle between $\mathbf{k}$ and $\mathbf{B}_0$. C_+ is the fast magnetosonic speed and C_- is the slow magnetosonic speed.

2.3 Instabilities in the Solar Wind

In this section, we shall consider common *linear instabilities* in the solar wind. Linear instabilities are characterized by an exponential growth of the amplitude of a Fourier component of quantity A as follows

$$A(\mathbf{k}, t) = A(\mathbf{k}) e^{\gamma t}, \tag{2.20}$$

where γ is the growth rate of the instability – see (2.12) for the definition. Instabilities play a significant role in the physics of the solar wind – they redistribute energy from sources of free energy, such as a non-equilibrium particle velocity distribution, or large-amplitude waves, to unstable wave modes. Therefore, non-equilibrium distributions, such as the bi-maxwellian distribution, are prone to instabilities. To put it simply, the larger the ratio of temperatures, called *temperature anisotropy*, the further from equilibrium the plasma is and the larger the growth rate of certain instabilities is. Because the mean free path in the solar wind is large compared to typical solar system distances, collisions do not move solar wind back to thermodynamic equilibrium and we generally see a lot of instabilitis in the solar wind.

The exponential growth of linear instabilities is limited by nonlinear behavior. The linear approximation breaks down when the amplitude becomes comparable to the background value of the field, or at the nonlinear time

$$t_\mathrm{nl} = \gamma^{-1} \ln\left(\frac{A_0}{A(\mathbf{k})}\right) \tag{2.21}$$

If the spatial scale of the instability is comparable to the bulk scales of plasma, the instability is called a *macroinstability*. Instabilities, where the characteristic size is on the scae of the particle inertial lengths or gyroradii, we are talking about *microinstabilities*.

2.3.1 Firehose Instability

Firehose instability increases the curvature of a magnetic flux tube and ultimately excites Alfven waves. It is driven by high parallel ion temperature. A magnetic flux tube is influenced by three forces: centrifugal force F_{C}, thermal pressure force $F_{p\perp}$ in the plane perpendicular to the flux tube, and magnetic stress force F_B of the flux tube, given by:

$$F_{\mathrm{C}} = \frac{m_i n_0 v_{\mathrm{th}\parallel}^2}{R}, \tag{2.22a}$$

$$F_{p\perp} = \frac{p_\perp}{R}, \tag{2.22b}$$

$$F_B = \frac{B^2}{\mu_0 R}. \tag{2.22c}$$

In equilibrium, the perpendicular thermal pressure of plasma $F_{p\perp}$ and the magnetic stress F_B counterbalance the centrifugal force F_{C}. The condition for the firehose instability is therefore

$$p_\parallel > p_\perp + B^2/\mu_0, \tag{2.23}$$

which can be written in terms of plasma betas as

$$\beta_\parallel > \beta_\perp + 2, \tag{2.24}$$

in the case of multiple species, this becomes

$$\sum_s \beta_{s\parallel} > \sum_s \beta_{s\perp} + 2. \tag{2.25}$$

Fluid Treatment

The dispersion relation of the firehose mode provided by linear analysis of the plasma as fluid is

$$\omega^2 = \frac{1}{2} k^2 v_A^2 \left[A_1 \pm \sqrt{A_2^2 + A_3^2} \right], \tag{2.26}$$

where

$$A_1 = \beta_{0\perp}(1 + \sin^2\theta) + \beta_{0\parallel}\cos^2\theta + 1, \tag{2.27a}$$

$$A_2 = \beta_{0\perp}(1 + \sin^2\theta) - 2\beta_{0\parallel}\cos^2\theta + 1, \tag{2.27b}$$

$$A_3 = \beta_{0\perp}\sin\theta\cos\theta. \tag{2.27c}$$

For parallel propagation ($\theta = 0°$), the growth rate is

$$\gamma_{\mathrm{fh}} = \frac{k_\parallel v_A}{2}\sqrt{\beta_{0\parallel} - \beta_{0\perp} - 2}. \tag{2.28}$$

For oblique propagation, there exists a limit angle $\theta_{\mathrm{fh,max}}$ defined by the equation

$$1 + \sin^2\theta_{\mathrm{fh,max}} = \left[1 - 3\frac{\beta_\parallel}{\beta_\perp^2}\left(2 + \beta_\perp - \beta_\parallel\right) \right]^{-1}. \tag{2.29}$$

Firehose mode cannot propagate for $\theta > \theta_{\mathrm{fh,max}}$[22].

Kinetic Treatment

When one does not neglect the kinetic effects of the ions, the linear dependence of the growth rate on the wave number vanishes. The second-order correction of γ_{fh}, which was provided by fluid approach, is

$$\gamma_{\mathrm{fh,c}} = \gamma_{\mathrm{fm}} \sqrt{1 - \frac{k_\parallel^2}{k_0^2}}, \tag{2.30}$$

where k_0 is a short-wavelength cut-off of $\gamma_{\mathrm{fh,c}}$, given by

$$\frac{k_0^2}{4} = \frac{\gamma_{\mathrm{fh}}^2}{k_\parallel^2} + \left(1 + \sum_s \frac{\omega_{\mathrm{p}s}^2}{\omega_{\mathrm{g}s}^2}\right)^2 \left[\sum_s \frac{\omega_{\mathrm{p}s}^2}{\omega_{\mathrm{g}s}^3} \left(\frac{\gamma_{\mathrm{fh}}^2}{k_\parallel^2} + \frac{2T_{s\perp} - 3T_{s\parallel}}{m_s}\right)\right]^{-2} \tag{2.31}$$

2.3.2 Mirror Instability

The mirror mode is a kinetic macroinstability. Contrary to the firehose instability, it evolves at an angle nearly perpendicular to waves. The dispersion relation (or rather its low-frequency limit) for the mirror mode is

$$\omega^2 = k_\parallel^2 v_A^2 \left[1 - \frac{1}{2} \sum_s \left(\beta_{s\parallel} - \beta_{s\perp}\right)\right], \tag{2.32a}$$

$$\mathrm{i}\sqrt{\frac{\pi}{2}} \frac{\beta_{\mathrm{i}\perp}^2}{\beta_{\mathrm{i}\parallel}} \frac{\omega}{k_\parallel v_{\mathrm{th,i}\parallel}} = 1 + \sum_s \left(\beta_{s\perp} - \frac{\beta_{s\perp}^2}{\beta_{s\parallel}}\right) + \frac{k_\parallel^2}{k_\perp^2} \left[1 + \frac{1}{2} \sum_s \left(\beta_{s\perp} - \beta_{s\parallel}\right)\right]. \tag{2.32b}$$

The condition for mirror instability is

$$\sum_s \frac{\beta_{s\perp}^2}{\beta_{s\parallel}} > 1 + \sum_s \beta_{s\perp}, \tag{2.33}$$

and the growth rate for the mirror mode is

$$\gamma_{\mathrm{mi}} = \sqrt{\frac{2}{\pi}} \frac{\beta_{i\parallel}}{\beta_{i\perp}} \left[\sum_s \beta_{s\perp} \left(\frac{\beta_{s\perp}}{\beta_{s\parallel}} - 1\right) - 1\right] k_\parallel v_{\mathrm{th,i}\parallel} \tag{2.34}$$

The mirror mode grows when the free energy of the pressure anisotropy is sufficiently large. However, the mirror mode is usually suppressed by the ion cyclotron instability, which consumes the free energy available in the anisotropy [22].

2.3.3 Ion Cyclotron Instability

The ion cyclotron instability occurs for L-mode waves with a frequency $\omega < \omega_{\mathrm{c}} = \omega_{\mathrm{gi}} A_{\mathrm{i}}/(A_{\mathrm{i}} + 1)$ when hot anisotropic ions interact with a cold isotropic background. The dispersion relation can be derived from the general

dispersion relation for an electromagnetic wave in a magnetized plasma [23, p. 283]. The dispersion relation is

$$1 - \frac{k_\parallel^2 c^2}{\omega^2} + \frac{\omega_{\mathrm{pe}}^2}{\omega_{\mathrm{ge}}^2} - \frac{\omega_{\mathrm{pe}}^2}{\omega_{\mathrm{ge}}\omega} + \frac{\omega_{\mathrm{pi}}^2}{\omega^2}\left[\frac{\omega}{k_\parallel v_{\mathrm{th,i}}} Z(\zeta_{\mathrm{i}}) + A_{\mathrm{i}}\left(1 + \zeta_{\mathrm{i}} Z(\zeta_{\mathrm{i}})\right)\right], \tag{2.35}$$

where

$$Z(\zeta) = \frac{1}{\sqrt{\pi}} \int_{-\infty}^{+\infty} \frac{\mathrm{d}x \exp(-x^2)}{x - \zeta}$$

is a plasma dispersion function for the Maxwell distribution, $\zeta_{\mathrm{i}} = \frac{\omega - \omega_{\mathrm{i}}}{k_\parallel v_{\mathrm{th,i}}}$. If the anisotropy is large (and therefore $T_\perp \gg T_\parallel \approx 0$), the dispersion relation simplifies to

$$k_\parallel^2 c^2 = \frac{\omega_{\mathrm{pi}}^2}{\omega_{\mathrm{gi}}^2} \frac{\omega^2}{\omega - \omega_{\mathrm{gi}}} - \frac{k_\parallel^2 c^2 \beta_{\mathrm{i}\perp}}{2} \frac{\omega_{\mathrm{gi}}^2}{(\omega - \omega_{\mathrm{gi}})^2)} \tag{2.36}$$

The unstable solution occurs for wavelengths much shorter than the ion inertial length and has a growth rate of

$$\gamma_{\mathrm{aic}} \approx \omega_{\mathrm{gi}} \sqrt{\frac{\beta_{\mathrm{i}\perp}}{2}}. \tag{2.37}$$

2.4 Formation and Evolution of the Moon

Geological history of the Moon provides insight into the composition of the Moon, which in turn is necessary to understand the coupling between the Moon and the flowing lunar wind e.g. in case of magnetic field induced in the lunar core. This section provides a concise review of humanity's understanding of the formation and evolution of the Moon in the context of lunar composition and solar wind interaction.

Historically, there have been three hypotheses of the lunar origin. The *capture* hypothesis, where the Moon formed independently form Earth and was gravitationally captured by the Earth; the *binary planet* hypothesis, the Earth and Moon have formed simultaneously from the same cloud and have always been gravitationally bound together; and the *fission* hypotesis, the material for Moon's creation was supplied from the Earth's mantle, after the core had formed. Today, it is thought that the Moon formed through a giant impact of a Mars-sized body on the early Earth about 4.5 billion years ago. Computer simulations suggest that the Moon has likely primarily formed from the material from the impacting planet. However, under certain conditions (fast spinning proto-Earth and the subsequent loss of angular momentum of the Earth-Moon system), the Moon could also have formed primarily form Earth's mantle [24]. The impact might have lead to the formation of a molten core and a magnetic field-supporting dynamo [25].

Returned samples of the lunar crust gave birth to the theory that a large portion of the Moon was initially molten and later stratified into the approximately spherical shells the Moon is composed of, as it crystallized.

This theorized event is called the *lunar magma ocean crytallization*. Another significant discovery was the magnetization of lunar crustal samples. The mechanism of the natural remanent magnetization of the lunar crust is still uncertain. One proposed mechanism is the so-called *thermoremanent magnetization* (TRM). It is due to the cooling of the crustal materials below the Curie temperature in the presence of an external magnetic field [25]. Another is *shock remanent magnetization*, where the rocks were magnetized by transient high pressures, possibly due to meteor impact [25]. For lunar crustal magnetization, see 2.6.3.

2.4.1 Ancient Lunar Dynamo

Let us now discuss the hypothetical ancient lunar dynamo. The Apollo-era samples suggested the existence of ancient magnetic fields with intesity ranging from 0.1 to 120 nT at the lunar surface. If the hypothetical lunar field had been approximately dipole, it would not have been able to produce this magnetic field variation between the returned samples and therefore it is likely that the proposed lunar magnetic field underwent large temporal variations [25]. Modern paleomagnetic studies now provide stronger evindence for the existence of a lunar core dynamo. For example, the oldest known unshocked lunar rock, troctolite 76535 was analyzed using magnetic measurements and thermochronological calculations. The data imply there was a long-lived magnetic field on the Moon some 4.2 billion years years ago, with magntiude of at least 1 µT at the surface . Other studies have provided additional evidence for an even later existence of the lunar dynamo, lasting at least until 3.56×10^9 years ago [26]. A recent study by *Mighani et al.* suggests that the lunar dynamo had lasted until sometime between 1.92 to 0.80 billion years ago [27].

2.4.2 Lunar Magma Ocean

Similar to many other other rocky bodies, it is thought that in the early stage of the formation of the Moon, a large part of the Moon was molten. This molten part s called the lunar magma ocean. The lunar magma ocean models were first developed to explain the high abundances of anorthosite in the lunar crust samples retrieved by the Apollo missions [28].

The widespread anorthosite distribution led to the hypothesis that the Moon was at least partially molten, and from this melt, anorthite plagioclase was buoyantly segregated to form an anorthositic crust [29]. Some models are even consistent with the Moon being fully molten and the lunar core having formed through metal-silicate partioning at the core-mantle boundary [28].

Modeling suggest that approximately 80 % of the lunar magma ocean solidified within the order of a thousand years [29]. This created anorthosite lid on the remaining magma ocean. In the absence of tidal heating, full solidification reqired in the order of tens of millions of years. When tidal heating from the Earth is taken into account, which would melt and recycle parts of the lunar crust, the solidification would take $\sim$ 220 million years [29].

2.4.3 Lunar Volcanism

The lunar maria are formed by volcanic basalts. The mare basalts cover approximately 17% of the lunar surface. Oceanus Procellarum, Mare Nubium, Mare Cognitum, and Mare Insularum were dated using crater size-frequency analysis [30]. The data show that volcanism was active over a long period of time, from $\sim$ 3.93 to 1.2 billion years ago. Most of the basalts erupted between 3.3 and 3.7 billion years ago [30].

2.5 Lunar Geoscience Methods

2.5.1 Electromagnetic sounding

Electromagnetic sounding is the measurement of the inductive response of conducting materials within the Moon. Assuming a body with a constant isotropic conductivity σ and using Farady's law of induction

$$-\partial_t \mathbf{B} = \boldsymbol{\nabla} \times \mathbf{E},$$

Ohm's law

$$\mathbf{j} = \sigma \mathbf{E},$$

Ampere's circuital law

$$\boldsymbol{\nabla} \times \mathbf{B} = \mu_0 \left(\mathbf{j} + \epsilon_0 \partial_t \mathbf{E} \right),$$

and assuming the displacement current $\epsilon_0 \partial_t \mathbf{E}$ is neglibible[3], i.e. $\omega \ll \sigma \mu_0 c^2$, one gets the diffusion equation for the magnetic field

$$\partial_t \mathbf{B} = \frac{1}{\mu_0 \sigma} \nabla^2 \mathbf{B}. \tag{2.38}$$

For the induction response of the Moon, which can be thought of as a series of concentric spherical shells, the solution can be found analytically – see [31].

This is, however, made significantly more complicated by the plasma environment of the solar wind – see section 2.7.3 for a detailed discussion. Therefore it is the best to conduct these measurements during the passing of the Moon through Earth's magnetospheric tail lobe. When the Moon enters the magnetic tail lobe from the (highly varying) IMF, the sudden change in the external magnetic field induces currents in the Moon. The measured disturbance in the ambient magnetic field is due to this inductive response of the Moon. The decay time of the core-induced field is in the order of days, and therefore, it appears as an internal dipole field when the Moon is passing through the tail lobe [32].

For the measurements, two magnetometers need to be used to separate the external and internal magnetic fields. A combination of a lunar surface

[3]For a characteristic timescale of one minute, this condition holds for any known object in the solar system [31].

magnetometer planted by the Apollo mission and a spacecraft-boarded magnetometer has been used. The ARTEMIS mission with the dual Themis satellites opossite to each other on the same orbit will allow for a more precise measurement [33]. The goal is to determine a so-called *transfer function* $h(\omega)$ defined as:

$$h(\omega)B_{\text{ext}}(\omega) = B_{\text{ext}}(\omega) + B_{\text{ind}}(\omega),$$

where B_{ext} is the external field and B_{ind} the induced field. The trasnfer function is used to calculate an *apparent conductivity*

$$\sigma_{\text{a}}(\omega) = \frac{4h^2(\omega)}{\mu_0 \omega R^2}, \tag{2.39}$$

where ω is the frequency of the wave component of the magnetic field, R is the lunar radius, and μ_0 is the permeability of free space [31], [34].

The finding of conductivity, for example, provide information about the temperature profile on the Moon as conductivity of the lunar rocks is a funciton of temperature. Further, the knowledge of the conductivity profile is vital for better modeling and analyses of the lunar interaction with the solar wind.

2.5.2 Seismology

During the Apollo lunar landing missions, a network of seismological experiements was set up on the Moon. The netowrk was only functional until 1977, when it was shut down due to a lack of funding. Nonetheless, more than 13 000 seimsic events were cataloged, which have been analyzed in decades to come [35]. There were active experiements, esigned to evaluate the subsurface structure in the vicinity of the experiment using controlled seismic sources. Passive seismometers detect natural seismic events. There are several types of moonquakes that the passive experiments detected. They are

1. deep moonquakes,
2. shallow moonquakes,
3. meteoroid impacts,
4. thermal moonquakes, and
5. a total of nine artificial impacts.

The majority of recorded events are due to deep moonquakes that originate at depths from 700 to 1200 km [35].

Simliarly to electromagnetic sounding, the seismic measurements are used to determine the transfer function for P-waves and S-waves and put constraints on the luanr composition [36].

2.5.3 Lunar Laser Ranging

Lunar Laser Ranging (LLR) is an indirect measurement of the location of a point on the lunar surface. It consists of measuring the time of flight of a laser pulse emitted from a station on the Earth and received after reflection off a retroreflector array on the lunar surface, providing the location of the Moon-based arrays with millimeter precision. LLR is used to infer the properties of Moon that infuence its orientation and movement: it can be used to measure Moon's moment of inertia and thus estimate parameters such as size, density, and ellipticity of the layers in Moon [37].

2.6 Lunar Composition

2.6.1 Core

The Earth has a large iron-rich core in its center. All of the terrestrial planets, as well as Jupiter's moons Ganymede, Europa, and Io are thought to have metallic cores. Therefore it is no surprise it has been assumed that the Moon has a metallic core as well. However, it has also been suggested that the Moon has a molten silicate core, instead [38]. The exact size, composition, and state of the core is not known to a high degree of certainty. The size and composition of core as well as other layers of the Moon is determined from the bulk properties of the Moon. Typically, a model's properties are compared to the measured masss, moment of inertia, Love numbers k_2, l_2, h_2, and the seismic and electromagnetic responses of the Moon. All of these parameters put a constraint on the size and shape of the lunar core, as well as the mantle and the crust.

The low mean lunar density implies that the lunar core is only small in size compared to that of terrestrial planets. Observation of the induced magnetic dipole moment in the passage through Earth's magnetotail indicated a possible highly conducting metallic core of 340 ± 90km [39]. The lunar mass and moment of inertia can be satisfied by either a solid iron core with $R \approx 330\,\text{km}$, or liquid eutectic Fe-FeS core with $R \approx 460\,\text{km}$ [32]. The core is thought to be predominately iron with light elements such as sulphur and carbon.

The estimate of the core radius could be skewed by a possible partially molten layer in the lower mantle. The molten mantle would have a higher conductivity than the solid mantle and thus the core would appear larger. The melt in the lower mantle would therefore mean that the core radius could be up to 40 km smaller than previously thought [32].

2.6.2 Mantle

The structure of the lunar mantle is uncertain. In addition to the tools used for inferring the properties of the lunar core (bulk moment of inertia, Love numbers, seismic and electromagnetic repsonse, etc.), the understanding

of the LMO crystallization process an important tool in the lunar mantle stratigraphy. The LMO has been modeled in experimental setups [40] as well as using numerical simulations [41]. The first mineral to crystallize from the cooling lunar magma ocean was Mg-rich olivine, followed by orthopyroxene. Therefore the lower mantle is expected to be composed of Mg-rich olivine, with the concentration of orthopyroxene increasing with altitude.

During the LMO crystallization process, the remaining magma became increasingly abundant in Ca and Fe. From this magma, Ca- and Fe-rich pyroxenes sank, while plagioclase crystals floated, forming a lid on the LMO and developing into the lunar crust [42]. In the late stages of LMO crystallization, the magma was increasing enriched by Fe, Ti, and other elements. It solidified into two types of rocks: the ilmenite-bearing cumulates, and cumulates enriched by thorium, potassium, rare earth elements, and phosporus, referd to by the acronym KREEP (named for the high abundance of potassium, rare earth elemnts, and phosphorus) [42].

The seismographic experiments revealed that the lunar mantle is a source of moonquakes. They can be categorized by the depth of their origin into shallow moonquakes and deep moonquakes. Little is known about shallow moonquakes because of their rarity. It has been speculated that they are due to the release of thermoelastic stresses in the upper mantle or lower crust [43]. Deep moonquakes, albeit being weaker than shallow moonquakes, are fairly common. Their sources, the so-called *nests*, are located at 700 to 1100 km below the lunar surface. More than 250 of these nests have been identified so far [43]. The deep moonquake activity is correlated with the tidal cycles and therefore it has been suggested that they are triggered by the tides.

Seismology, as explained in the section 2.5.2 is also useful to put constraints on the composition of the layers in the lunar mantle. The Apollo seismographic data indicate that in the upper mantle, the sesmic velocities are almost constant, whereas the middle mantle is more heterogeneous. There is some evidence for a seismic discontiunity in the middle mantle at approximately 460 km below the lunar surface. If it exists, it may indicate the depth of the ancient lunar magma ocean. It is also possible, however, that this discontinuity is only local to the Procellarum–KREEP Terrane. In depths below 1150 km, seismic waves have been found to be attenuated. Therefore, it has been proposed that approximately 150 km of the bottom mantle is partially molten [44]. This has been inferred from seismic measurements of deep moonquakes. This theory has been contested by, e.g., *Matsuyama et al.*, who used LLR to put constraints on the model of the interior structure of the Moon [45].

2.6.3 Crust

The lunar crust is hihgly non-uniform. This can be first noticed due to the differences in albedo between the lunar highlands and the lunar maria. Samples from the lunar crust as well as indirect measurements of its properties have shown a complex picture. First, gamma-ray spectrometry has revealed differences in thorium – in particular, high abundaces of thorium in the

Procellarum and Imbrium maria. It has also been discovered that the lunar crust may be thicker on the lunar farside than on the nearside. Unlike the Earth, the Moon's curst does not have plate tectonics.

The crust and the top-most mantle layers consist of discrete regions with fundamentally different properties and origin called *terranes*. The three major terranes are the Procellarum KREEP[4] terrane, the Feldspathic Highlands terrane, and the South Pole–Aitken basin [36].

The Feldspthic Highlands Terrane (FHT) covers approximately 60% of the lunar surface [36]. It is the oldest of the major terranes. The upper crust of the FHT is approximately 90% plagioclase. The Procellarum KREEP Terrane (PKT) is characterized by the high abundace of incompatible elements that formed the KREEP rocks. The fact that KREEP rocks are only abundant within this region of the lunar crust suggests that it is where the last crystallization of the LMO, by then highly abundant in incompatible elements, occured. The SPA is a large impact basin, and the largest known impact structure in the solar system [38].

The lunar crust has been studied using samples acquired by Apollo missions and measurements from satellites. Mare basalt and volcanic glass samples provide an opportunity to study the mantle because they are exposed on the lunar surface while having originated in the mantle. Seismometers planted by the Apollo mission provide (by definition[5]) information about crustal thickness.

Crustal Magnetic Anomalies

Initial magnetometer measurements featured inexplicable magnetic field enhancements outside the lunar wake. These enhancements were explained by the presence of so-called lunar crustal anomalies – permanently magnetized regions within the lunar crust. There are two major theories of their origin: thermoremanent magnetization (TRM) and shock remanent magnetization (SRM). Thermoremanent magnetization is the acquisition of crustal magnetization from an ancient lunar dynamo. Paleomagnetic studies suggest that the lunar crustal magnetization 4.2 billion years ago was likely due to a magnetic field generated by the lunar dynamo – see section **??**. On the other hand, shock remanent magnetization is a process where the lunar magnetic anomalies have originated due to meteor impacts onto the lunar surface. This theory is supported by a high abundance of crustal magnetism on the antipodes of lunar maria [46]. This rule is, however, not universal as there are no magnetic anomalies on the antipodes of SPA (South-pole Aitken basin), and there is an unexpected anomaly near the Descartes Crater. These exceptions may be due to later geologic activity, such as Mare Imbrium

[4] *KREEP* stands for potassium, rare earth elements, and phosphorus – elements abundant in KREEP rocks

[5] The interface between crust and mantle is defined by Mohorovicic discontinuity *(Moho)* – a jump increase in longitudinal seismic wave *(P-wave)* phase velocity to a value between $7.6\,\mathrm{km\,s^{-1}}$ and $8.6\,\mathrm{km\,s^{-1}}$ [38]. It is the shallowest discontinuity in Earth, but there is an even shallower discontinuity in the lunar crust at 20 km[38].

formation [47]. The meteor impact hypothesis is supported by simulations of vapor dynamics following a meteor impact. The vapors in the model were able to produce a strong magnetic field that could have magnetized the crustal rocks [47].

2.6.4 Atmosphere and Dust Environment

The Moon has a very thin atmosphere that has been stable for the last 3 billion years. This was not always the case, as it has been suggested that ancient volcanic activity 3.5 billion years ago formed an atmosphere that could have reached 1 kPa on the surface, which is approximately 50% more the current value on Mars [48]. The lunar atmosphere was first measured using cold cathode ionization gauges installed by the Apollo missions 14 and 15 [49], and a year later using a mass spectrometer installed by the Apollo 17 mission [50], [51]. Recently, it was studied in-situ by the Lunar Atmosphere and Dust Environment Explorer (LADEE) [52].

The lunar atmosphere is so thin that it is a so-called *surface boundary exosphere*, meaning that it is colissionless and the gas molecules largely move uninterrupted along their keplerian trajectory. The main constituents are hydrogen, helium, neon, and argon [50]. The concentration of helium is highly variable (5×10^3 to $3 \times 10^4\,\mathrm{cm}^{-3}$) [53]. All noticeable He abundance increases are correlated with solar particle events reported by the Space Weather Prediction Center, while all decreases are correlated with the passages of the Moon through Earth's magnetotail. This correlation implies that the solar wind is a significant contributor to the lunar atmospheric He. The data also show a constant background source flux due to the radioactive decay of Th-232 and U-238 in the Moon [53]. Neon is supplied by the solar wind as well. There is, however, no correlation of Ne abundance to the solar parcticle events or passages through the Earth's magnetotail. This is due to neon's large time to photoionization, which is longer compared than the typical timescale of solar particle events or magnetotail passages [53]. The LADEE measurements have revealed an enhanced abundace of Ar over western maria – its likely source is the decay of K-40 in KREEP rocks in the Procellarum KREEP Terrane.

Apart from the gas cloud, the Moon is enveloped by a dust cloud, which was studied by LADEE as well. The first sign of the existence of this dust cloud was the observation of a "horizon glow" above the lunar terminator by Apollo 17 astronauts while on orbit above the Moon [54].

The dust cloud is produced by the impacts of high-speed cometary dust particles (as opposed to dust particles of asteroidal origin which typically hit the Moon at lower speeds) [55]. In addition to that, the exposure of the lunar surface to UV radiation and solar wind flow may result in the electrostatic charging and subsequent mobilization of small dust particles, especially over the lunar terminator [55]. In addition to a permanent dust cloud, there is a highly fluctuating cloud composed of nanodust ($< 20\,\mathrm{nm}$) [56].

2.7 Solar-Wind Interaction with the Moon

As a first-order approximation, the Moon can be treated as a resistive obstacle with no magnetic field in the solar wind that absorbs all incident ions. This produces a cavity in the lunar wake that is slowly refilled by a magnetosonic wave. There are, however, phenomena that increase the complexity of the interaction:

1. The solar wind plasma interacts with small scale magnetic field in the form of magnetic anomalies.
2. The conducting lunar core has eddy currents induced in it by a changing external magnetic field.
3. Ions that impact on the Moon may sputter lunar regolith matter.
4. There are plasma instabilities in the lunar wake.

The shape of the lunar wake depends on the parameters of the solar wind and the interplanetary magnetic field (IMF). If the bulk velocity of the solar wind is larger than the thermal velocity, then the cavity will reach further in the wake. The bigger the thermal velocity relative to the bulk velocity, the faster the lunar cavity is filled, and therefore the cavity region is shorter [57]. If we account for IMF, the interaction becomes more complicated. If the magnetic field lines are parallel to the solar wind flow, they prevent the cavity from being filled [57]. The rarefaction region produces the characteristic signature of the interaction with an unmagnetized body – magnetic field enhancement in the central wake. This is due to the diamagnetic current $\mathbf{j} = (\mathbf{B} \times \boldsymbol{\nabla} p)/B^2$ caused by the pressure gradient on the boundary of the wake.

2.7.1 Lunar Surface Interaction

As the solar wind ions and electrons impact on the dayside of the Moon, they are either absorbed by or scattered from the lunar surface. In case the particles encounter lunar crustal anomalies, they may be reflected from them. These processes result in the absence of plasma in the near wake (and the subsequent formation of the void region), the charging of the lunar surace, and the formation of the exosphere.

It has historically been assumed (see e.g. [1]) that the almost all impacting solar wind ions are simply absorbed by the lunar surface. The data from sub-keV Atom Reflecting Analyzer (SARA) instrument onboard the Indian Chandrayaan-1 have shown that up to 20 % of solar wind protons may be scattered/reflected from the lunar surface in the form of energetic neutral atoms [58]. Interstellar boundary explorer misison had consistent results [59], [60].

As the lunar surface is exposed to the flowing solar wind and to solar wind photons, it is electrically charged. Assuming equillibrium, electric currents to

the surface balance out. Because the lunar crust has a low conductivity, the equillibirum need not hold globally and therefore, the lunar surface charge is not uniform [61].

There are four processes that drive these currents:

1. photoemission of electrons,
2. solar wind electrons impacting on the surface,
3. solar wind ions impacting on the surface,
4. surface ionization (that produces so-called secondary electrons). [62]

On the lunar dayside, the photoemission of electrons from the lunar regolith is the dominant process and therefore the lunar surface is charged positively [62]. On the nightside the electron thermal flux dominates and the surface is charged to a negative potential, as evidenced by Lunar Prospector data [63]. The strongest charging of the lunar surface was osberved at the lunar sunset terminator region [63].

2.7.2 Lunar Crustal Magnetic Fields

While the Moon does not have a global magnetic field that would shield it from the solar wind, there are magnetic anomaly regions on the lunar surface. They are constituted by magnetized rocks in the lunar crust. The major crustal anomalies (in order of significance) are the Gerasimovich anomaly, the South-pole Aitken basin (SPA), and Mare Marginis anomaly [64]. The crustal anomalies may be observed visually, as inside the magnetic anomalies, there are regions with relatively high albedo called *swirls*. Their different composition is likely due to being shielded from solar wind weathering [65]. However, the existence of lunar crustal anomalies was first inferred from the unexpected observation of magnetic field enhancements outside the lunar wake.

Many of the anomalies have magnetic fields sufficiently strong to produce a mini-magnetosphere [61], [66]. A shock wave has been observed above the Mare Imbrium antipode [67]. A mini-magnetosphere above the Gerasimovich anomaly has been modeled using a 3D hybrid code. The model suggests that there is a large reduction of proton flux on the lunar surface at areas over the anomaly and an enhanced flux in the surrounding areas as the protons are deflected [68].

There are three mechanisms by which solar wind ions interact with a magnetic anomaly:

1. deflection and impact without a change in velocity,
2. deceleration on the electric potential over the anomaly, followed by impact,
3. heating and reflection into space [69].

The reflected ions enter the lunar wake and constitute so-called *type-II-entry ions*. Type-II-entry ions are ions that were scattered from the lunar surface or deflected from the lunar crustal anomalies. This differentiates them from type-I entry ions that refill the lunar plasma cavity without having interacted with the Moon.

2.7.3 Induced Lunar Dipole

The magnetic field induced in the nearly spherical lunar core, therefore, decays with a characteristic time $T \sim \sigma\mu_0 L^2$, where σ is the conductivity and L the radius of the lunar core. For the lunar core, this time is longer than 10 days[32].

In case the Moon is submerged in plasma, the description becomes more complicated. Ohm's law as presented in the previous paragraph does not hold and can be replaced by generalized Ohm's law

$$\mathbf{E} + \mathbf{v} \times \mathbf{B} = \eta\mathbf{j} + \frac{1}{ne}\mathbf{j} \times \mathbf{B} - \frac{1}{ne}\boldsymbol{\nabla} \cdot \mathbf{P}_\mathrm{e} + \frac{m_\mathrm{e}}{ne^2}\frac{\partial \mathbf{j}}{\partial t}, \tag{2.40}$$

where $\mathbf{v}$ is the plasma bulk velocity, η is the resistivity, n is the plasma concentration, $\mathbf{P}_\mathrm{e}$ is the tensor of electron pressure [23]. Because the plasma in the solar wind–Moon interaction can be considered collisionless, the resistive term (1st term on RHS) is only relevant inside the Moon, where the evolution of the magnetic field is described by the diffusion equation (2.38). It should be noted though that this relation is a feature of a linearized one-fluid MHD model and as such, an approximation.

The environment of the solar wind is highly variable, and the temporal variations in the external magnetic field induce eddy currents in the highly conducting lunar core ($> 10^{-2}\,\mathrm{S\,m^{-1}}$ [31]). The induced dipole is confined in the Moon on the lunar dayside by the solar wind pressure [68], [70]. The induced magnetic field, however, contributes to the magnetic field in the lunar wake. Simulation results suggest that the influence is stronger than theoretically expected [70]. This may be due to the induced field at the solar terminator being compressed deeper into the lunar wake by the solar wind or due to currents induced in the solar wind.

2.7.4 Instabilities in the Lunar Wake

Both fluid and kinetic instabilities occur in the lunar wake. As the beams of ions refill the lunar wake, two-stream instability occurs [71]. At the boundary of the lunar cavity, there are regions where flute instability conditions are fulfilled [72]. The ARTEMIS probes have measured electrostatic waves excited by electron beam instability [73]. Electrons and ions in the wake are non-maxwellian, which could lead to kinetic instabilities. PIC simulations have suggested that in the center of the lunar wake, small disturbances in the electron velocity distribution lead to a non-linear growth of electron phase space holes. These phase space holes can disrupt ion beans [74]. The authors suggest that this instability has likely been observed as broadband

electrostatic noise during the wake passage of WIND [75]. A broadband electrostatic noise in the lunar wake has also been attributed to type-II entry ions in proton-governed regions (these occur when the IMF is parallel to the flow and therefore type-II-entry ions[6] are more prevalent in the near wake than type-I entry ions) [76]. The parallel cooling of ions refilling the wake may lead to the mirror mode instability or the ion cyclotron mode. These instabilities can also be triggered by the additional energy source provided by type-II-entry ions [77].

2.8 Lunar Wake Modeling

The simplest model of the plasma wake is a one-dimensional simulation of plasma expansion into the plasma cavity. The simulation box is in the solar wind rest frame, and thus the model covers the entire lunar wake - see [71] for a particle-in-cell implementation of this model[7]. This model was extended into two dimensions, where a circular plasma cavity is refilled from the sides – see [79]. Today, it is still too computationally expensive to implement a global[8] fully-kinetic 3D dynamic model with a decent resolution and particle sampling, and therefore a fluid approach needs to be used to some extent. The lunar wake has been modeled using a one-fluid plasma model – see [81]. Another approach is to use a hybrid model where electrons are treated as a massless fluid. Such model has been used in 2D (see for example [82]) and 3D case [68], [70], [83]–[86]. The simulation results have been compared to observations to show that the main features of the lunar wake are reproduced. The downside to hybrid models is that they are limited to ion phenomena, and thus, kinetic electron phenomena like phase space holes can not be investigated. It should be noted that the electron space phase holes disrupt ion beams, and therefore, their exclusion does affect ions in the model.

Electromagnetic Induction in the Lunar Core

Fatemi et al. have used a 3D hybrid model to study the interaction of solar wind and the Moon with a dipole induced in the lunar core [68]. In a qualitative study, three situations with magnetic dipoles of different strengths were numerically simulated. They showed that on the lunar dayside, there are no significant perturbations to the magnetic field. The authors have suggested the propagation of the magnetic field perturbations is suppressed by a current sheet. The lunar wake, however, was perturbed in their model compared to the control case, and furthermore, in their model, the perturbations extended outside the bounds of the Mach cone [68].

[6] The term type-II ions describes ions that enter the wake after having been reflected from the Moon, whereas type-I entry is due to the refilling of the lunar cavity [76].

[7] This article contained erroneous electric potentials. See [78] for correction of the original article.

[8] Local phenomena like surface charging have been modeled kinetically – see [80]

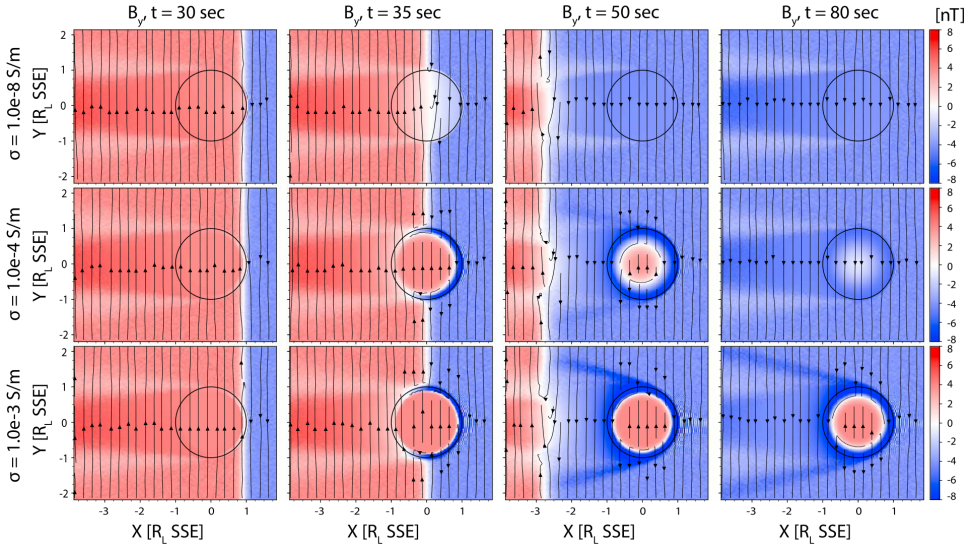

Figure 2.4: Graphs of the y-component of the magnetic field in hybrid simulations by *Fuqua Haviland et al.* for different lunar core conductivity values. The rows show different conductivities, the columns show different times. Source: [70]

Fuqua Haviland et al. have used a 3D hybrid model to study the effect of the conducting core on the interaction [70]. A discontinuity in IMF was introduced that, frozen in the solar wind, traveled with the solar wind flow. The magnetic field diffused into the lunar interior from the lunar dayside, while the core with high conductivity – and thus low magnetic diffusivity – retained the initial magnetic field. The induced magnetic field was enhanced in the lunar wake compared to the predictions given by a vacuum-response model (a model where plasma was omitted). The authors propose two mechanisms for this unexpected enhancement: plasma-induced magnetic fields and the compression of induced fields into the deep lunar wake that originate at the solar terminator region [70]. Figure 2.4 shows the evolution of the y-component of the magnetic field in their model as the discontinuity moves along the obstacle. Each row shows a different conductivity of the lunar core in the model. The columns correspond to times 20, 30, 35, 50, 80, and 220 s since the initial time, respectively. At $t = 30$ s, the discontinuity reaches the lunar dayside and at $t = 35$ s, the induced magnetic field starts to form as the discontinuity cannot quickly diffuse further into the conducting lunar core.

Current Systems in the Lunar Wake

The emergence of electric current systems in the lunar wake was studied by *Fatemi et al.* via the means of a 3D hybrid model[68]. The authors identified three current systems: around the void region ($\mathbf{J}_1$), around the rarefaction region ($\mathbf{J}_2$), and aroung the recompression region ($\mathbf{J}_3$). In case the IMF is anti-paralell to the solar wind flow, the electric currents are flowing

perpendicular to the IMF direction. The electric currents are circular and loop around the lunar wake. If the IMF is perpendicular to the solar wind flow, the current systems are aligned with the lunar wake and are connected. In the vicinity of the lunar poles, the current $\mathbf{J}_2$ connects to $\mathbf{J}_1$, and at the wake refilling distance, the current $\mathbf{J}_3$ connects to $\mathbf{J}_1$ and considerably enhances electric current density. In case the IMF direction is any arbitrary angle, the current systems are expected to be a superposition of the two (perpendicular and parallel) cases. All the three current systems are bound by the Mach cone. The current $\mathbf{J}_1$ on the void boundary is diamagnetic – due to the gradient of electron density. The current systems $\mathbf{J}_2$ and $\mathbf{J}_3$ around the rarefactin and recompression regions were not expected by the theoretical works [68]. These currents are a result of the confinement of the magnetosonic wave propagating perpendicular to the IMF.

Influence of Crustal Magnetism

The influence of the crustal magnetic fields has been studied in a 3D hybrid model by *Fatemi et al.* [77]. The velocity distribution of protons reflected from the crustal anomalies is not known and therefore various reflection and models have been employed as presented by *Holmstrom et al.* [87]. Interestingly, the choice of the reflection function does not have a significant qualitative effect on the lunar plasma environment. The reflected protons contribute to plasma compressions (additional to the wake disturbances with reflection neglected). Further, the interaction has been modeled above the Gerasimovich anomaly via a 3D hybrid code [68].

Chapter 3

The Model

Plasma is a very complicated system; only a handful of analytical solutions exist, and therefore plasma physics necessitates numerical solutions for non-trivial problems. Experimental physics is not a sufficient option either, especially for space plasmas, because probes only show a spatially and temporally localized picture. Numerical simulations in space physics are a useful complimentary tool to in-situ measurements. When compared to data from spacecraft, the numerical models help provide an explanation for the observed phenomena, as well as a global picture of the observed phenomena.

In this thesis, a two-dimensional hybrid model is used to study the interaction between the Moon and the solar wind with the presence of both hydrogen and helium ion species. The hybrid model is presented in Section 3.1. The numerical scheme used to solve the model is presented in Section 3.2.

In this chapter, the model and the numerical scheme used for its solution are presented, as well as boundary conditions and the treatment of the

Because in the solar-wind interactions with planetary objects, the solar wind is collisionless (and the model used in this thesis is collisionless as well), the main focus of this chapter will be to present the numerical treatments of collisionless plasma and specifically the hybrid model that was used in this thesis to model the solar-wind interaction with the Moon.

3.1 Particle-Ion–Fluid-Electron Hybrid Model

In general, the hybrid model involves the solving of the Vlasov or the Boltzmann equation for some species of plasma particles, while other are treated by an MHD equation. The electromagnetic field is determined from Maxwell equations with self-consistent source terms. The particle-ion–fluid-electron hybrid model (which, in this thesis, will simply refered to as "the hybrid model" for brevity) is a model of plasma which can be tought of as a middle ground between the particle and fluid models of plasma. In numerical treatment, the time-step needs to be sufficiently small, so that the gyration of the particles is not neglected. A fully particle model necessitates the using the scale of electrons, the smallest of the timescales, because their gyrofrequency is the largest of all the particle species. The particle-ion–fluid-electron model

treats all ion species as particles (or macro-particles) and electrons as a fluid. This is practical for numerical simulations, because it allows one to work at timescales typical for ions, which are larger. To simplify the model, electrons are often treated as a *massless fluid* (this simplification is justified by the fact that the mass densities $\rho_\mathrm{e} \ll \rho_\mathrm{i}$) that neutralizes the ion charge – i.e. quasineutrality is assumed. If the displacement current is also assumed to be negligible, one is left with the following set of differential equations for the position $\mathbf{x}_{\alpha,n}$ and $\mathbf{v}_{\alpha,n}$ of n-th particle of ionic specie α, magnetic field $\mathbf{B}$ and electric field $\mathbf{E}$:

$$\frac{\mathrm{d}\mathbf{v}_{\alpha,n}}{\mathrm{d}t} = \frac{q_\alpha}{m_\alpha}\left(\mathbf{E} + \mathbf{v}_{\alpha,n} \times \mathbf{B}\right), \tag{3.1}$$

$$\frac{\mathrm{d}\mathbf{x}_{\alpha,n}}{\mathrm{d}t} = \mathbf{v}_{\alpha,n}, \tag{3.2}$$

$$\frac{\partial \mathbf{B}}{\partial t} = -\boldsymbol{\nabla} \times \mathbf{E}, \tag{3.3}$$

where the electric field

$$\mathbf{E} = \frac{1}{\rho_{\mathrm{Q,i}}}\left(-\mathbf{j}_\mathrm{i} \times \mathbf{B} + \frac{1}{\mu_0}(\boldsymbol{\nabla} \times \mathbf{B}) \times \mathbf{B} - \boldsymbol{\nabla} p_\mathrm{e}\right) + \frac{\eta}{\mu_0}\boldsymbol{\nabla} \times \mathbf{B}, \tag{3.4}$$

where μ_0 is the vacuum magnetic permeability, η is the resistivity of the plasma, $p_{e,0}$ and $\rho_{\mathrm{Q}e,0}$ are the electron pressure and electric charge in the undisturbed plasma, and finally the ionic electric charge density and ionic electric current density

$$\rho_{\mathrm{Q,i}}(\mathbf{x}) = \sum_{\alpha=1}^{s}\sum_{n=1}^{N_\alpha} q_\alpha \delta(\mathbf{x} - \mathbf{x}_{\alpha,n}), \tag{3.5}$$

$$\mathbf{j}_\mathrm{i}(\mathbf{x}) = \sum_{\alpha=1}^{s}\sum_{n} q_\alpha \delta(\mathbf{x} - \mathbf{x}_{\alpha,n})\mathbf{v}_{\alpha,n}, \tag{3.6}$$

where s is the number of ionic species, N_α is the number of particles of the specie α and q_α their electric charge, δ is the Dirac delta function, and $\mathbf{x}_{\alpha,n}$, $\mathbf{v}_{\alpha,n}$ the position and velocity (respectively) of nth particle of specie α.

The equation to be closed using a state equation. Assuming adiabatically expanding, isotropic electron fluid, the pressure is

$$p_\mathrm{e} = p_{\mathrm{e},0}(n_\mathrm{e}/n_{\mathrm{e},0})^\kappa, \tag{3.7}$$

where κ is the poisson constant. Another option is to approximate the electrons as an ideal gas

$$p_\mathrm{e} = (n_\mathrm{e} k_\mathrm{B} T_\mathrm{e}$$

Derivation

This set of equations is derived from Maxwell's equations and the Boltzmann transport equation. Consider particles of species α with phase space distribution f_α and charge q_α in an external (for now) electromagnetic field $(\mathbf{E}, \mathbf{B})$.

They obey the Boltzmann transport equation

$$\frac{\mathrm{d}f_\alpha}{\mathrm{d}t} = \left(\frac{\partial f_\alpha}{\partial t}\right)_{\mathrm{coll}}, \tag{3.8}$$

where on the right hand side is the collision term, which, as discussed in Section 2.1.1, can be assumed zero for the purposes of this thesis. Expanding the total derivation and substituting $\boldsymbol{\nabla}_{\mathbf{v}} f_\alpha = \mathbf{F}/m_\alpha$ and $\mathbf{F} = q_\alpha(\mathbf{E} + \mathbf{v} \times \mathbf{B})$, we have the *Vlasov equation* for particles of species α:

$$\frac{\partial f_\alpha}{\partial t} + \mathbf{v} \cdot \frac{\partial f_\alpha}{\partial \mathbf{x}} + \frac{q_\alpha}{m_\alpha}(\mathbf{E} + \mathbf{v} \times \mathbf{B}) \cdot \frac{\partial f_\alpha}{\partial \mathbf{v}} = 0, \tag{3.9}$$

where $\mathbf{E}$ and $\mathbf{B}$ are the electric and magnetic field, q_α is the electric charge of a particles of species α, and m_α its mass.

Now, let us consider the electromagnetic field. It is governed by the Maxwell's equations, where the charged particles contribute to the source terms. Combining (3.9) for all the species in plasma (in our case, electrons, protons, and alpha particles) with Maxwell's equations gives us a system of PDE describing the plasma. The evolution of the magnetic field is by Ampere's circuital law, for which Darwin approximation (low-frequency limit) will be used (i. e. displacement current is assumed negligible). This gives us the equation

$$\boldsymbol{\nabla} \times \mathbf{B} = \mu_0 \mathbf{j}, \tag{3.10}$$

where μ_0 is the permeability of free space and

$$\mathbf{j}(\mathbf{x}, t) = \sum_\alpha \mathbf{j}_\alpha(\mathbf{x}, t) = \sum_\alpha q_\alpha \int \mathbf{v}_\alpha f_\alpha(\mathbf{x}, \mathbf{v}_\alpha, t) \mathrm{d}^3\mathbf{v}_\alpha. \tag{3.11}$$

The main advantage of the hybrid model is that it allows one to simulate on the timescale of ions (which is typically larger than the electron timescale). This is achieved by only treating the ions as particles and approximating the electrons as a fluid.

Multiplying the Vlasov equation (3.9) by $n_\alpha v_\alpha$ and integrating over the velocity space, we arrive at the first moment equation for the electron fluid

$$m_\mathrm{e}\frac{\partial}{\partial t}(n_\mathrm{e}\mathbf{u}_\mathrm{e}) + m_\mathrm{e}\boldsymbol{\nabla} \cdot (n_\mathrm{e}\mathbf{u}_\mathrm{e} \otimes \mathbf{u}_\mathrm{e}) + \boldsymbol{\nabla} \cdot \mathbf{P}_\mathrm{e} = rho_{\mathrm{Q,e}}\mathbf{E} + \mathbf{j}_\mathrm{e} \times \mathbf{B} \tag{3.12}$$

where n_e is the particle density, $\mathbf{u}_\mathrm{e}$ the bulk velocity, and $\mathbf{P}_\mathrm{e}$ the tensor pressure of the electron fluid. $\rho_{\mathrm{Q,e}}$ is the electron electric charge density, $\mathbf{j}_\mathrm{e}$ the electric current density due to electrons. Simplifying, we get the MHD equation for the momentum of the electron fluid,

$$m_\mathrm{e}n_\mathrm{e}\left(\frac{\partial}{\partial t} + \mathbf{u}_\mathrm{e} \cdot \boldsymbol{\nabla}\right)\mathbf{u}_\mathrm{e} = \rho_{\mathrm{Q,e}}\mathbf{E} + \mathbf{j}_\mathrm{e} \times \mathbf{B} - \boldsymbol{\nabla} \cdot \mathbf{P}_\mathrm{e} - \rho_\mathrm{e}\eta\,\mathbf{j}. \tag{3.13}$$

Next, we assume the electron pressure is isotropic, $\boldsymbol{\nabla} \cdot \mathbf{P}_\mathrm{e} \equiv \boldsymbol{\nabla} p_\mathrm{e}$, and that the electron fluid is massless, $m_\mathrm{e} = 0$. The assumption of masslessness means the left hand side of the equation (3.13) is zero. The electronic current density

and electric charge can be elminated with the ionic counterparts. Using quasineutrality $\rho_{\mathrm{Q,e}} \approx \rho_{\mathrm{Q,i}}$, the electric charge density in the equation (3.13) can be substituted by ion charge density. The density of the electron electric current $\mathbf{j}_{\mathrm{e}}$ is eliminated using $\mathbf{j} = \mathbf{j}_{\mathrm{i}} + \mathbf{j}_{\mathrm{e}}$ is used, where $\mathbf{j}$ is substituted from (3.10). Thus, we receive the equation (3.4).

If ions are treated as individual particles, we finally have the system (3.1), (3.2), (3.3), (3.4), (3.5), (3.6). For computational purposes, the Vlasov equation for ions needs to be sampled more coarsely, so that the system of equations is smaller. This is achieved by grouping particles into macro-particles that represent multiple orders of magnitude of particles.

3.2 Current Advance Method – Cyclic Leapfrog

The numeric scheme used in the code that is used to solve the hybrid model in this thesis is called the *Current Advance Method – Cyclic Leapfrog* [88], because it combines two time-advancement schemes: the current advance method for ions, and the cyclic leapfrog for the magnetic field. The electric and magnetic fields, as well as moments of the distribution of ions, are discretised on a staggered grid with the magnetic field and ion moments specified at cell vertices and the electric field specidifed at the centers of these cells.

The notation used in this sections is as follows: the time step is denoted by Δt, the grid spacing $\Delta x = \Delta y = h$. A quantity X at time step k will be denoted by a superscript: $X^k := X(t_0 + k\Delta t)$, while the spatial indices of a field ψ will be denoted by a subscript: $\psi_{ij} := \psi(x_0 + i\Delta x, y_0 + j\Delta y)$.

Particle Distribution Moment Evaluation

In order that the model is computationally viable, particles have to be treated with the cloud-in-cell approach, where particles are represented by a macro-particle – a cloud of particles with a distribution $\varphi(\mathbf{x} - \mathbf{x}_{\alpha,n})$, which is then averaged onto the mesh when calculating the moments of the velocity distribution of ions. The equations (3.5) and (3.6) therefore become

$$\rho_{\mathrm{Q,i}} = \sum_{\alpha} \sum_{n} q_\alpha \varphi(\mathbf{x} - \mathbf{x}_{\alpha,n}),$$
$$\mathbf{j}_{\mathrm{i}} = \sum_{\alpha} \sum_{n} q_\alpha \varphi(\mathbf{x} - \mathbf{x}_{\alpha,n}) \mathbf{v}_{\alpha,n},$$

where $\sum_n$ is now the summation over all the macroparticle belonging to ion specie α, as opposed to over all particles belonging to that ion specie. In the numarical simulation, the ionic electric charge density $\rho_{\mathrm{Q,i}}$ and the ionic electric current density $\mathbf{j}_{\mathrm{i}}$ are calculated at the nodes of the mesh the following

way

$$\rho_{ij} = \sum_{\alpha} \sum_{n} q_\alpha \tilde{\varphi}_{\alpha,n;ij}, \tag{3.14}$$

$$\mathbf{j}_{ij} = \sum_{\alpha} \sum_{n} q_\alpha \tilde{\varphi}_{\alpha,n;ij} \mathbf{v}_{\alpha,n}, \tag{3.15}$$

where $\tilde{\varphi}$ is the discretised equivalent of φ on the mesh: $\tilde{\varphi}_{\alpha,n;ij} = \varphi(\mathbf{x} - \mathbf{x}_{\alpha,n})$.

This approach, however, produces noise in the moments, which can ultimately lead to numerical instabilities [88]. Therefore, the calculated $\rho_{ij}, \mathbf{j}_{ij}$ need to be smoothed. One way to do this is using a weighted average of the surrouding nodes first in x direction and then in y direction. For field ψ, let us denote the field smoothed in direction x $\psi^{(x)}$, and analogously for y. At node (i, j), the smoothed field is

$$\psi_{ij}^{(x)} = \tfrac{1}{4}\psi_{i-1,j} + \tfrac{1}{2}\psi_{i,j} + \tfrac{1}{4}\psi_{i+1,j}, \tag{3.16a}$$

$$\psi_{ij}^{(xy)} = \tfrac{1}{4}\psi_{i-1,j}^{(x)} + \tfrac{1}{2}\psi_{i,j}^{(x)} + \tfrac{1}{4}\psi_{i+1,j}^{(x)}. \tag{3.16b}$$

Electromagnetic Field Evaluation

The electric field is calculated by adopting the formula (3.4) on the mesh. Because the electric field is on a staggered mesh with nodes at cell centers, cell-centered averaging of the other quantities needs to be employed. The electric field in terms of the cell-centered averages is

$$\mathbf{E} = -\frac{\langle \mathbf{J}_\mathrm{i} \rangle \times \langle \mathbf{B} \rangle}{\langle \rho_{Q,\mathrm{i}} \rangle} + \frac{\langle \boldsymbol{\nabla} \times \mathbf{B} \rangle \times \langle \mathbf{B} \rangle}{\mu_0 \langle \rho_{Q,\mathrm{i}} \rangle} - \frac{\langle \boldsymbol{\nabla} p_\mathrm{e} \rangle}{\langle \rho_{Q,\mathrm{i}} \rangle} + \frac{\eta}{\mu_0} \langle \boldsymbol{\nabla} \times \mathbf{B} \rangle, \tag{3.17}$$

where $\langle \psi \rangle$ denotes the cell-centered average of a field ψ, defined as

$$\langle \psi \rangle_{i+1/2,j+1/2} := \frac{1}{4} \left(\psi_{i,j} + \psi_{i,j+1} + \psi_{i+1,j} + \psi_{i,j+1} \right),$$

with the derivative approximated by central difference calculated at the center of the cell using the vertices of the cell as follows:

$$\left\langle \frac{\partial \psi}{\partial x} \right\rangle_{i+1/2,j+1/2} \approx \frac{1}{2\Delta x} \left(-\psi_{i,j} + \psi_{i,j+1} + \psi_{i+1,j} - \psi_{i,j+1} \right).$$

For the evaluation of the electric and magnetic fields elsewhere than the nodes – which is needed for the stepping of particles, for example – bilinear interpolation is used. The term $\frac{\eta}{\mu_0} \langle \boldsymbol{\nabla} \times \mathbf{B} \rangle$ provides numerical diffusivity [89], and therefore, a minimal value is set throughout the whole simulation box, to provide numerical stability. Another tool to increase stability is the setting of minimal value for $\rho_{Q,\mathrm{i}}$, so that $\mathbf{E}$ does not diverge.

In the CAM-CL method, the electric and magnetic fields are calculated at a smaller time-step in a method called *substepping* [88]. The particles are not moved and no new particle moments are evaluated – only the electric and magnetic field is stepped using a leapfrog scheme. This is useful to

suppress electromagnetic noise [88]. Let M be the number of substeps (for all simulations used in this thesis, $M = 10$) and $\Delta\tilde{t} = \Delta t/M$. For simplicity, let us denote $\mathbf{B}_m = \mathbf{B}^{k+m/M}, \forall m = 0, \ldots, M$, and likewise $\mathbf{E}_m$. The evolution of the magnetic and electric field is then

$$\mathbf{B}_1 = \mathbf{B}_0 - \Delta\tilde{t}\,\boldsymbol{\nabla} \times \mathbf{E}_0, \tag{3.18a}$$
$$\mathbf{B}_2 = \mathbf{B}_0 - 2\Delta\tilde{t}\,\boldsymbol{\nabla} \times \mathbf{E}_0, \tag{3.18b}$$
$$\mathbf{E}_m = E(\rho_{\mathrm{c}}^{k+1/2}, \mathbf{J}_{\mathrm{i}}^{k+1/2}, \mathbf{B}_m, T_{\mathrm{e}}),\ \forall m \tag{3.18c}$$
$$\mathbf{B}_{m+1} = \mathbf{B}_{m-1} - 2\Delta\tilde{t}\,\boldsymbol{\nabla} \times \mathbf{E}_m, \text{ for } m = 1, \ldots, M-1 \tag{3.18d}$$
$$\mathbf{B}_M = \mathbf{B}_{M-2} - 2\Delta\tilde{t}\,\boldsymbol{\nabla} \times \mathbf{E}_{M-1}, \tag{3.18e}$$
$$\tilde{\mathbf{B}}_M = \mathbf{B}_{M-1} - \Delta\tilde{t}\,\boldsymbol{\nabla} \times \mathbf{E}_M, \tag{3.18f}$$

and finally, the next time-step of $\mathbf{B}$ is calculated average of the full-stepped $\mathbf{B}_M$ and half-stepped $\tilde{\mathbf{B}}_M$:

$$\mathbf{B}^k = \tfrac{1}{2}(\mathbf{B}_M + \tilde{\mathbf{B}}_M). \tag{3.19}$$

Current Advance

The current advance ties together the time-stepping of the electric field and the macroparticles. To achieve a second-order accuracy of time integration, a scheme similar to a leapfrog scheme is used, called the *current advance method*. In a classical leap-frog scheme for charged particles, the difference equations of motion are

$$\mathbf{x}^{k+1/2} = \mathbf{x}^{k-1/2} + \mathbf{v}^k \Delta t \tag{3.20a}$$
$$\mathbf{v}^{k+1} = \mathbf{v}^k + \frac{q}{m}\left(\mathbf{E}^{k+1/2}(\mathbf{x}^{k+1/2}) + \mathbf{v}^{k+1/2} \times \mathbf{B}^{k+1/2}(\mathbf{x}^{k+1/2})\right). \tag{3.20b}$$

A problem with this set of equations is that it is implicit as $\mathbf{v}^{k+1/2}$, $\mathbf{E}^{k+1/2}$ are not known. This necessitates the pre-pushing of the velocity $\mathbf{v}$ and estimating the electric field $\mathbf{E}$ at time level $k + 1/2$– this is done using a mixed time-level electric field

$$\mathbf{E}* = \mathbf{E}(\rho_{Q,\mathrm{i}}^{k+1/2}, \mathbf{j}_{\mathrm{i}}^{k}, \mathbf{B}^{k+1/2}, p_{\mathrm{e}}).$$

The current advance method involves the pre-pushing of not all the particles, but only the total ionic electric current at each grid point as follows:

$$\mathbf{j}_{\mathrm{i}}^{k+1/2} = \mathbf{j}_{\mathrm{i}} * + \frac{\Delta t}{2}\left(\Lambda \mathbf{E} * + \boldsymbol{\Gamma} \times \mathbf{B}^{k+1/2}\right), \tag{3.21}$$

where

$$\mathbf{j}_{\mathrm{i}}^{*} = \sum_s \varphi^{k+1/2} q_s \mathbf{v}_s^k, \tag{3.22a}$$
$$\Lambda = \sum_s \varphi^{k+1/2} \frac{q_s^2}{m_s}, \tag{3.22b}$$
$$\boldsymbol{\Gamma} = \sum_s \varphi^{k+1/2} \frac{q_s^2}{m_s} \mathbf{v}_s^k, \tag{3.22c}$$

where $\sum_s$ is the sum over all macroparticles, and φ is the weighing function. The current $\mathbf{j}_{\mathrm{i}}^*$ is called the *free-streaming current* [88], because it was not yet accelerated.

Properties and Limitations

The current advance method allows the modeling of multiple ion species with ease. In current advance method, the ionic electric current does not need to be advanced per-particle and then collected if the free-streaming moments (3.22) are collected. This makes the calculations faster as only one iteration over particles is required instead of two.

The smoothing (3.16) of moments provides numerical stability, but it means that short-wavelength wave modes are suppressed by design.

3.3 Initial and Boundary Conditions

In the model there are two boundaries: a natural boundary given by the lunar surface, and an artificial boundary, which is necessitated by the finite simulation box. The simulation domain and its boundaries are shown in a schematic in Fig. 3.1. Both the lunar-surface boundary and the external boundary of the simulation box have to be implemented carefully so that the boundary conditions do not produce numerical instability on the one hand, and so that the real-life system is well-described.

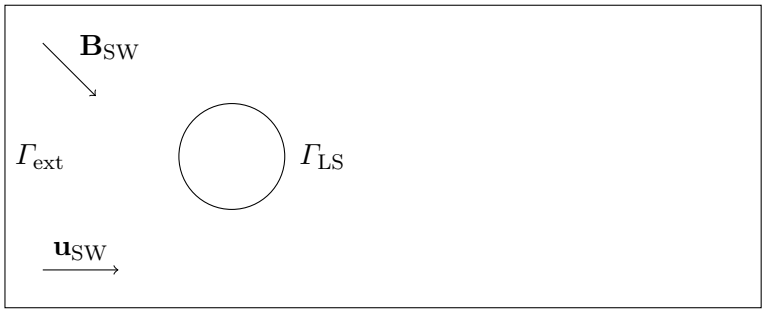

Figure 3.1: Schematic of the simulation domain (not to scale).

The simulation box is initialized to resemble the undisturbed solar wind with interplanetary magnetic field $\mathbf{B}_{\mathrm{SW}}$; ionic species $\alpha = \mathrm{p}, \mathrm{\alpha}, \ldots$ with the bulk velocity $\mathbf{u}_{\alpha,\mathrm{SW}}$, electric charge density $\rho_{\alpha,\mathrm{SW}}$, thermal anisotropy $A_{\alpha,\mathrm{SW}}$, and paralell beta $\beta_{\|\alpha,\mathrm{SW}}$. However, all simulation units are in the terms of dimensionless parameters. The magnetic field is initialized with a value

$$\mathbf{B}_0 = \mathbf{B}_{\mathrm{SW}}/B_{\mathrm{SW}}$$

in every node of the mesh, and the electric field is initialized with a value

$$\mathbf{E}_0 = -\mathbf{u}_0 \times \mathbf{B}_0 = -\frac{\mathbf{u}_{\mathrm{SW}} \times \mathbf{B}_{\mathrm{SW}}}{v_{\mathrm{A}} B_{\mathrm{SW}}}$$

in every node of its mesh, so that the electric field is self-consistent (see for example [90]). Macro-particles are generated with bi-Maxwellian distribution (see 2.6) (or Maxwellian in case the initial thermal anisotropy of the ionic specie that the macroparticle belongs to is equal to 1) with a uniform current density $\rho_{0,\alpha}$ and a specified number of macro-particles in each cell carrying that charge. For specific initialization values used in each simulation run used in this study, see Chapter 4.

The external boundary is treated with periodic boundary conditions. This works well with the initialization, as the plasma throughout the entire domain is initialized as undisturbed solar wind, and as solar wind flows outward past the moon, the macroparticles crossing the boundary appear upstream the Moon as the undisturbed solar wind. This approach is simple to implement. However, a disadvantage is that it does not allow the simulation to run infinitely, as the particles that interacted with the Moon once reappear upstream and produce simulation artifacts. On the other hand, the constant super-alfvénic inflow of the solar wind pushes any waves further downstream (see Results and Discussion).

Model of The Lunar Interior

Ideally, the behavior of the natural boundary Γ_{LS} in the model would reflect that of its real counterpart. With regards to the electromagnetic field that could mean computing Maxwell's equations, or perhaps the diffusion of magnetic field in the lunar interior. The interaction of particles with the boundary would be complicated to model, as the ions interact with crustal magnetic fields as well as the charged lunar surface. This leads to a small part of the ions being reflected back into the solar wind (and entering the wake as type-II entry ions), with the vast majority being absorbed by the lunar surface. The modeling of this interaction has only achieved locally above the Gerasimovich anomaly [91]. For a global model, the limited resolution does not allow a proper modeling, although a simple reflection model has been implemented [77].

The electric and magnetic fields in the lunar interior can be calculated in the CAM–CL scheme, because in the hybrid model, if the inverse ionic charge density $\rho_{Q,\mathrm{i}}$ is set to zero, the scheme (3.18) for the substepping of electromagnetic field becomes a leapfrog scheme of the diffusion equation (2.38) of the magnetic field. For the study of the influence of the conducting lunar interior, only σ needs to be changed from the "background value" (which is used for the stabilization of the scheme, because it increases diffusivity [89] – see also Section 3.2). This is the approach used in this thesis. In my previous work [92], several implementation methods have been tested against one another. In this thesis, I chose to use a hyperbolic tangent function as the transition between the conducting layer with a constant resistivity and the background (also with resistivity constant), because it provides smoothing of the transition while being computationally fast [92]. This was used only in simulation run 5 (see Chapter 4) to isolate the studied effect. In other runs, the background value is used throughout the entire simulation box.

The macro-particles that intersect the lunar surface must be either deflected or removed from the simulation. The model used in this thesis neglects the interaction of ions with the lunar surface and therefore all ions are assumed to be absorbed by the lunar surface. The macro-particles need to be treated carefully, though, because in the calculation of $\mathbf{E}$ in the hybrid model, some terms are divided by the ionic electric charge density $\rho_{Q,\mathrm{i}}$. The introduction of minimal ionic charge density prevents these terms from diverging and crashing the simulation. Still, the discontinuity in the ionic charge density is not desired, as it would create a discontinuity in the electric field. Therefore, the macro-particles need to be removed over a distance as to not create a discontinuity. In the model used in this thesis, this is achieved by marking particles that pass throught the lunar surface for removal. This can technically be done by assigning them to a separate ionic specie. The particles in this specie for removal are than randomly deleted at each timestep with a probability given by

$$p = \frac{v_r \Delta t}{R_{\mathrm{M}}},$$

where r is the distance of the macro-particle from the center of the lunar obstacle, v_r is the velocity in that direction, Δt the timestep and R_{BC} is the size of the boundary condition. This means that the path after which the macro-particles will be removed has an exponential distribution and does not depend on the velocity of the particle.

Chapter 4

Results and Discussion

A total of 6 two-dimensional lunar wake simulations are analysed in this qualitative study. The goal is to evaluate the influence of alpha particles on the lunar wake – see Chapter 1 – with the focus on three phenomena:

1. the alpha/proton drift,
2. the potential formation and evolution of instabilities due to temperature anisotropy,
3. and the inductive response of the conducting lunar core.

For this reason, the simulations whose results are presented below are of four kinds: (1) reference simulations, (2) simulations that isolate the alpha/proton drift, while keeping other parameters at standard values, (3) simulations that isolate ion anisotropy and parallel beta instead, and (4) simulations that investigate the influence of the lunar core. The structure of this chapter is informed by this categorization.

Units and Coordinate System

All simulation results presented come from 2.5-dimensional simulations, in which the symmetry $\frac{\partial}{\partial z} = 0$ applies. This means that the simulation mesh has only two dimensions, while the electric and magnetic fields have three dimensions, and the z coordinate of particles is neglected. The coordinate system used in these simulations is defined by the bulk velocity of the solar wind $\mathbf{u}_{\mathrm{SW}}$ and the interplanetary magnetic field in the solar wind $\mathbf{B}_{\mathrm{SW}}$. The x-coordinate is defined parallel to the solar wind flow $\mathbf{u}_{\mathrm{SW}}$. The y-coordinate is defined in such a way that the vector $\mathbf{B}_{\mathrm{SW}}$ lies in the plane (x, y), i. e. so that $B_{\mathrm{SW},z} = 0$.

The model relies on dimensionless quantities based off natural constants. Proton inertial length d_{p} (see equation (2.1)) is used as the unit of distance and inverse proton cyclotron frequency $\Omega_{\mathrm{p}}^{-1} \equiv \omega_{\mathrm{c,p}}^{-1}$ as the unit of time. This means that Alfvén velocity of protons, $v_{\mathrm{A,p}}$ is the unit of speed, because $d_{\mathrm{p}}\Omega_{\mathrm{p}} = v_{\mathrm{A,p}}$. Another typical length is the lunar radius R_{M}, which is used throughout this section instead of d_{p}. The magnetic field is expressed in terms of the value B_{SW}.

	run 0	run 1	run 2	run 3	run 4	run 5
N_x	2200	2200	2200	2200	2200	2200
N_y	900	900	900	900	900	900
N_p/cell	128	128	128	128	128	64
N_α/cell	64	64	64	64	64	32
$v_\mathrm{p}/v_\mathrm{A}$	5.0	5.0	5.0	5.0	5.0	5.0
$\Delta v_\alpha/v_\mathrm{A}$	–	0.67	0.67	0.67	0.67	0.67
ϕ_B	-45.0	-45.0	-45.0	-45.0	-45.0	-45.0
$\beta_{\parallel\mathrm{p}}$	1.0	1.0	1.0	1.0	0.1	1.0
$\beta_{\parallel\alpha}$	–	0.1	0.1	0.1	0.1	0.1
proton anisotropy	1.0	1.0	1.0	0.2	4.0	1.0
α anisotropy	–	1.0	0.2	1.0	1.0	1.0
background resistivity	0.01	0.01	0.01	0.01	0.01	0.01
lunar core resistivity	–	–	–	–	–	10^{-5}

Table 4.1: Select parameters of simulation runs

Simulation Parameters

The resolution of the simulation was chosen to be $\Delta t = 0.01\Omega_\mathrm{p}^{-1}$ in time and $h = \Delta x = \Delta y = 0.2d_\mathrm{p}$ in space. The size of the lunar obstacle is $R_\mathrm{M} = 13.0h$. An overview of parameters used to initialize each of the simulation runs is provided in Table 4.1. The simulations are set up in the same manner with the difference of the parameters that were isolated for investigation. In all the simulations, the magnetic field is initialized with

$$\mathbf{B}_\mathrm{SW} = (B_\mathrm{SW}/\sqrt{2}, -B_\mathrm{SW}/\sqrt{2}, 0).$$

All the simulation runs contain a proton hydrogen specie initialized with

$$\mathbf{v}_\mathrm{p} = (5v_\mathrm{A}, 0, 0).$$

The number of proton macroparticles spawned at each cell is denoted by N_p/cell. In all runs, the simulation box contained $\sim 10^8$ proton macroparticles. Simulation runs 1 - 5 also contain an alpha particle specie initialized with the value

$$\mathbf{v}_\alpha = (v_\mathrm{p} + \Delta v_\alpha/\sqrt{2}, -\Delta v_\alpha/\sqrt{2}, 0),$$

where Δv_α is the drift velocity of the alpha specie with respect to the bulk of the solar wind.

4.1 Reference Simulation

Here I present the results of a simulation that serves as the default and was used to compare with the simulations with the investigated effects. The parameters of this simulation are listed under run 0 in Table 4.1. It contained a proton species only, to serve as a reference. The computed quantities in

this simulation at time $t = 50\Omega_{\mathrm{p}}^{-1}$ are shown in Figures A.1 and A.2 in the appendix – on the left hand side, magnetic field $\mathbf{B}$, proton particle density n_{p}, proton bulk velocity density u_{p}, and proton temperature anisotropy $A_{\mathrm{p}} = T_{\perp \mathrm{p}}/T_{\parallel \mathrm{p}}$; on the right hand side, the electric field $\mathbf{E}$.

All the quantities are bound by a Mach cone with an apex angle of approximately 20°. This means that no wave modes are propagating away at a velocity $\gtrapprox 2v_{\mathrm{A}}$ (in direction normal to the wake structure). The depletion of the solar wind plasma by the lunar obstacle leads to a very low protonic charge density in the near lunar wake. It should be noted that in the model, the protonic charge density is artificially higher than what would be the case in a real scenario. This is due to the handling of incident particles upon the boundary representing the lunar wake, where they are marked for removal at a random time after passing through the boundary, instead of being immediately removed. The reasons for this handling are explained in Chapter 3.

This void, called the lunar cavity, is refilled by protons that are accelerated by an electronic pressure gradient [82]. This occurs on both flanks of the lunar wake, although there is some asymmetry in the system, provided by the external magnetic field orientation (as it is not anti/parallel to the solar wind flow). As the proton beams interact in the middle of the lunar wake, a two–stream instability occurs [79]. Additionally, as these protons are depleted from the flanks of the lunar wake, two rarefaction waves propagate outward from the center of the lunar wake.

The magnetic field is enhanced in the lunar wake. This is likely caused by a pressure gradient of the proton specie on the flanks of the lunar wake and the resulting diamagnetic current. In the model, the pressure gradient reflects on the electric field, and therefore the magnetic field as well through substepping.

4.2 Proton/Alpha Drift Influence

The solar wind is predominantly composed of protons and electrons. Approximately 5% of the solar wind ions are alpha particles. The alpha particle specie drifts in the direction of the magnetic field with an average drift velocity of $0.67v_{\mathrm{A}}$ relative to the solar wind. See Section 2.1 for a detailed review. To assess the influence of the alpha particle specie, results from simulation runs 0 and 1 (see Table 4.1) are compared in this Section. Simulation run 0 serves as a reference and did not include the alpha-particle ion specie.

A plot of all quantities in simulation run 1 at time $t = 50\Omega_{\mathrm{p}}^{-1}$ can be found in Figures A.3 and A.4 in the appendix – similarly to the purely proton case, on the left hand side, magnetic field $\mathbf{B}$, proton number density ρ_{p}, proton bulk velocity density u_{p}, and proton temperature anisotropy $A_{\mathrm{p}} = T_{\perp \mathrm{p}}/T_{\parallel \mathrm{p}}$; on the right hand side, the electric field $\mathbf{E}$, number density ρ_{He} carried by the alpha specie, alpha bulk velocity density u_{He}, and helium temperature anisotropy $A_{\mathrm{He}} = T_{\perp \alpha}/T_{\parallel \alpha}$.

Figure 4.1 features side-by-side graphs of charge density of protons in

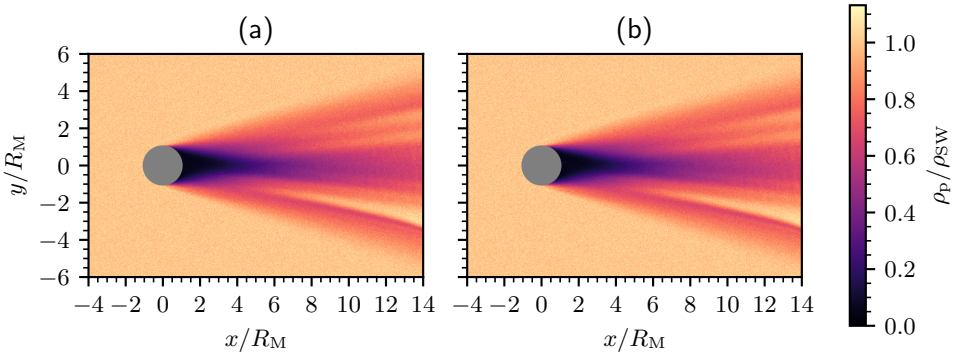

Figure 4.1: proton electric charge density (divided by solar wind mass density) in the lunar wake in the case of (a) purely proton solar wind (i.e. simulation run 0) and (b) solar wind containing a drifting alpha particle specie (simulation run 1)

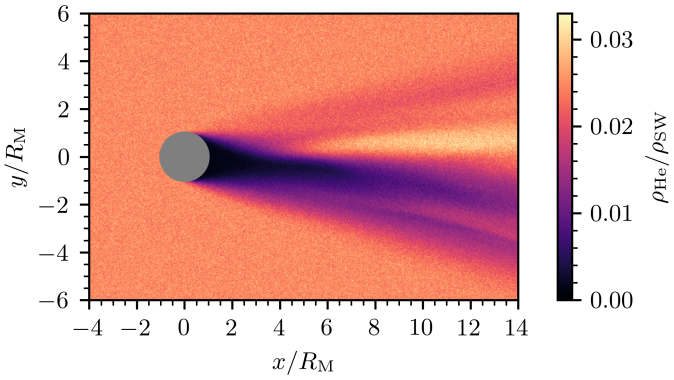

Figure 4.2: alpha-particle electric charge density (divided by solar wind mass density) in the lunar wake in simulation run 1

simulation runs 0 and 1, respsectively. The charge density of alpha particles in simulation run 1 is plotted in Figure 4.2. The plasma cavity in the wake of the alpha density is angled approximately 5° from the x-axis.This is corresponding to the bulk velocity of alpha particles in the unperturbed solar wind in simulation run 1, $\mathbf{v}_{\alpha,\mathrm{SW}}/v_\mathrm{A} = (5.47, -0.47, 0)$. However, it is not the case that the α-wake structure is a proton-wake rotated by 5°. The perturbations of the helium charge density are bound by the same Mach cone as the purely proton wake is in the control case. And the α-wake is highly asymmetrical.

There is a notable enhancement of ρ_α (with respect to the upstream value) on the $+y$ flank of the wake along the x axis extending far into the wake, separated from the unperturbed flow by an outward-propagating rarefaction wave – similar to the recompression region in the purely proton wake. There also seems to be a structure resembling the typical recompression region on the $-y$ flank, with a steeper gradient of alpha charge density, but lower amplitude of enhancement.

The perturbation of the magnetic field (i.e. the difference of the magnetic

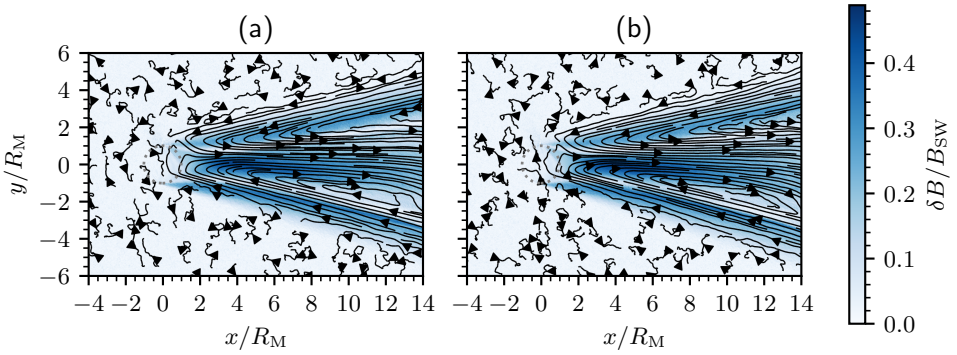

Figure 4.3: Figures (a) and (b) show the magnetic field perturbation in the lunar wake in the case of (a) a purely proton solar wind (i.e. simulation run 0) and (b) solar wind containing a drifting alpha particle specie (i.e. simulation run 1), respectively. The field lines are plotted in the xy plane and therefore do not show the contribution of B_z; it is however inclued in the magnitude B of the magnetic field, plotted in shades of blue.

field minus the upstream value) is plotted in Figure 4.3. Subfigure (a) shows the control case – a purely proton solar wind, subfigure (b) shows solar wind in simulation run 1 with alpha particles added. The differences in the general structure are only subtle. They are better highlighted in Figure 4.4, that shows the graphs of the magnetic field on a line defined by a constant x so that lower-magnitude disturbances may be identified more easily. The left and right columns show magnetic field for $x = 4R_M$ and $x = 10R_M$, respectively. The rows in each column show the magnitude of the magnetic field and the B_x, B_y and B_z components, respectively. The magnetic field from the reference simulation is graphed in blue and the magnetic field from simulation 1 is shown in orange. For all three directional components of the magnetic field as well as the magnitude of the magnetic field, the wake magnetic-field signature is slightly shifted ($\lessapprox 0.1R_M$) toward negative y – appearing to be "pulled" by the alpha specie. Further, the z-component of the magnetic field is more significantly perturbed by the alpha specie. Most notably, the peaks at $y \approx 0.6R_M$ for $x = 4R_M$ and at $y \approx 1.3R_M$ for $x = 10R_M$ are supressed.

This behavior can be attributed to the enhancement of the magnetic field in the plasma cavity typical for the purely proton lunar wake – see reference simulation results in Section 4.1. In a purely proton lunar wake, the magnetic field in the central wake is enhanced by a diamagnetic current resulting from the pressure gradient of protons on the flanks of the wake. The depletion of alpha particles from the lunar wake causes an alpha pressure gradient, and therefore, additional diamagnetic currents. These currents may be responsible for the shifting of the magnetic field signature toward $-y$, consistent with the direction of the drift of the alpha specie relative to the proton specie.

Figure 4.5 shows the graphs of proton charge density and bulk velocity on a line defined by a constant x. Similarly to the aforementioned graph, the left and right columns show the quantities for $x = 4R_M$ and $x = 10R_M$, respectively. The rows in each column show the proton charge density and

the u_x, u_y and u_z components. The overall $\approx 5\%$ decrease in proton charge density is due to a different setup of the simulations, where in the reference simulations, all the ions are protons, while in simulation run 1, 5% of protons are replaced by alpha particles. While in x and y direction, there are no large-scale changes to the protonic bulk velocity, there are changes to $u_{z,\mathrm{H}}$ farther downstream in the $+y$ flank of the wake. It is unclear what the mechanism for this supression of peak is.

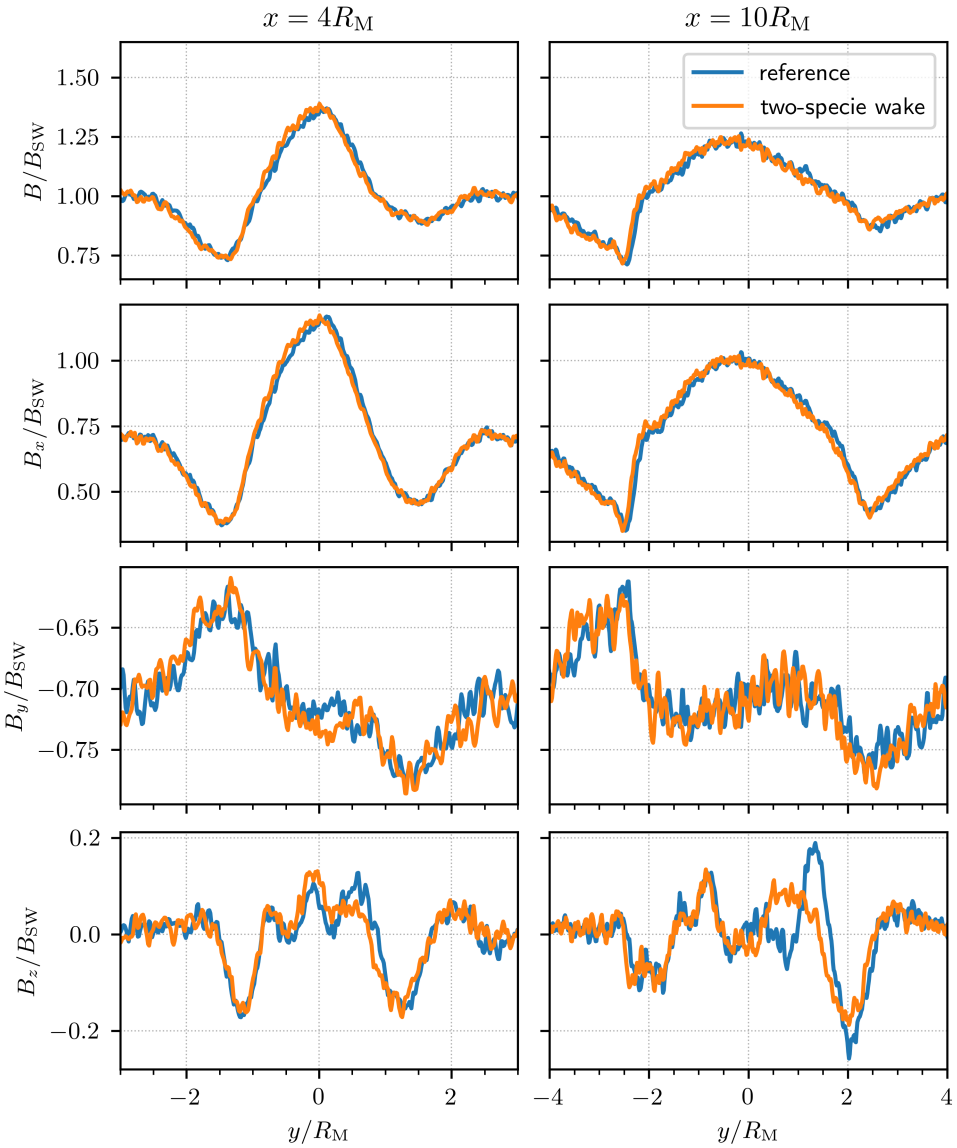

Figure 4.4: The cross sections of magnetic field amplitude and directional components. Simulation run 0 is in blue and simulation run 1 is in orange.

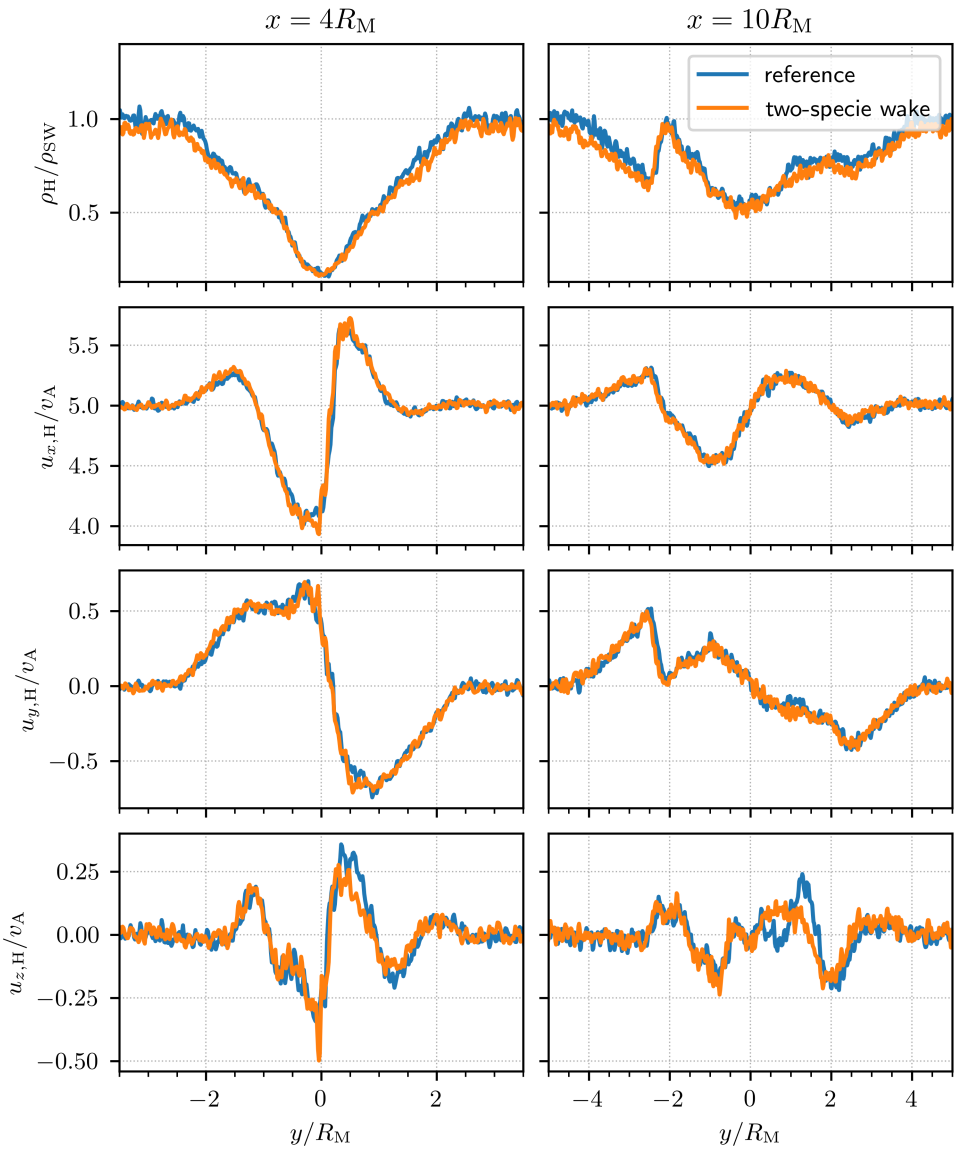

Figure 4.5: The cross sections of proton density and directional components of proton bulk velocity. Simulation run 0 is in blue and simulation run 1 is in orange.

4.3 Temperature Anisotropy

The lunar wake plasma is highly anisotropic in the central wake both in the control case – see Figure A.1 – and in the simulation with both the protons and alpha particles – see the bottom graphs in Figures A.3 and A.4. The high tempereature anistropy has the potential to launch plasma instabilities in the lunar wake [22], and in the solar wind, the alpha particle drift and high alpha temeperature anisotropy produce an ion cyclotron instability [93]. For a review of instabilities, see sections 2.2 and 2.7.4.

Because high anistropy and parallel beta of particles in plasma play a role in the formation of instabilities typical for the solar wind (see Section 2.3), various values of tempetature anisotropy and parallel betae of both solar wind protons and alpha particles in the upstream solar wind were used in the simulations (see Table 4.1) so that the potential formation is more thoroughly investigated. The pairs of values of temperature anisotropy and parallel beta were chosen according to the histogram in Figure 2.3 which shows abundances in the solar wind as measured by SWE/Wind.

Figures A.3, A.4, A.5, A.6,A.7, A.8,A.9,A.10 featuring graphs of runs 1 through 4, the runs that are relevant for this particular problem, are located in the appendix. This chapter features select comparisons in quantities between the simulation runs. Figure 4.6 shows the graphs of the magnetic field (field lines superimposed onto a map of the magnitude of the magnetic field) in simulation runs 1 and 4. In runs 1 and 2, the maximum magnetic field, found in the center of the near lunar wake in the plasma cavity, is greater than that of runs 3 and 4. There are generally no differences in the global structure of the lunar wake magnetic field. However, there are notable differences in the z-component of the magnetic field – see Figure 4.7. In simulation run 3 far down the wake ($8R_M < x < 14R_M$), B_z exhibits a different structure in the center of the wake.

Both proton density and velocity show stronger dependence on the upstream temperature anisotropy. Figure 4.8 presents a comparison of proton charge density between runs 1 and 4. The proton density in the run with enhanced upstream proton anisotropy shows a wave-like structure in the rarefaction cone region, as well as a more pronounced plasma cavity in the far wake ($x > 8R_{\mathrm{M}}$). The components of bulk velocity are shown in Figures 4.9, 4.10, and 4.11.

Compared to run 1, which serves as a control, in run 3, all components of the proton bulk velocity $\mathbf{u}_{\mathrm{H}}$ show a different structure in the entire wake. This may be cased by a smaller average proton gyroradius of the particles due to the smaller upstream temeprature anisotropy. Likewise, run 4 shows a different structure throughout the entire wake, which may be simply due to the greater gyroradii. There is, however, also a notabe wave-like structure originating from the wake propagating outward through the recomression region. These waves may be the signature of an instability forming in the central lunar wake.

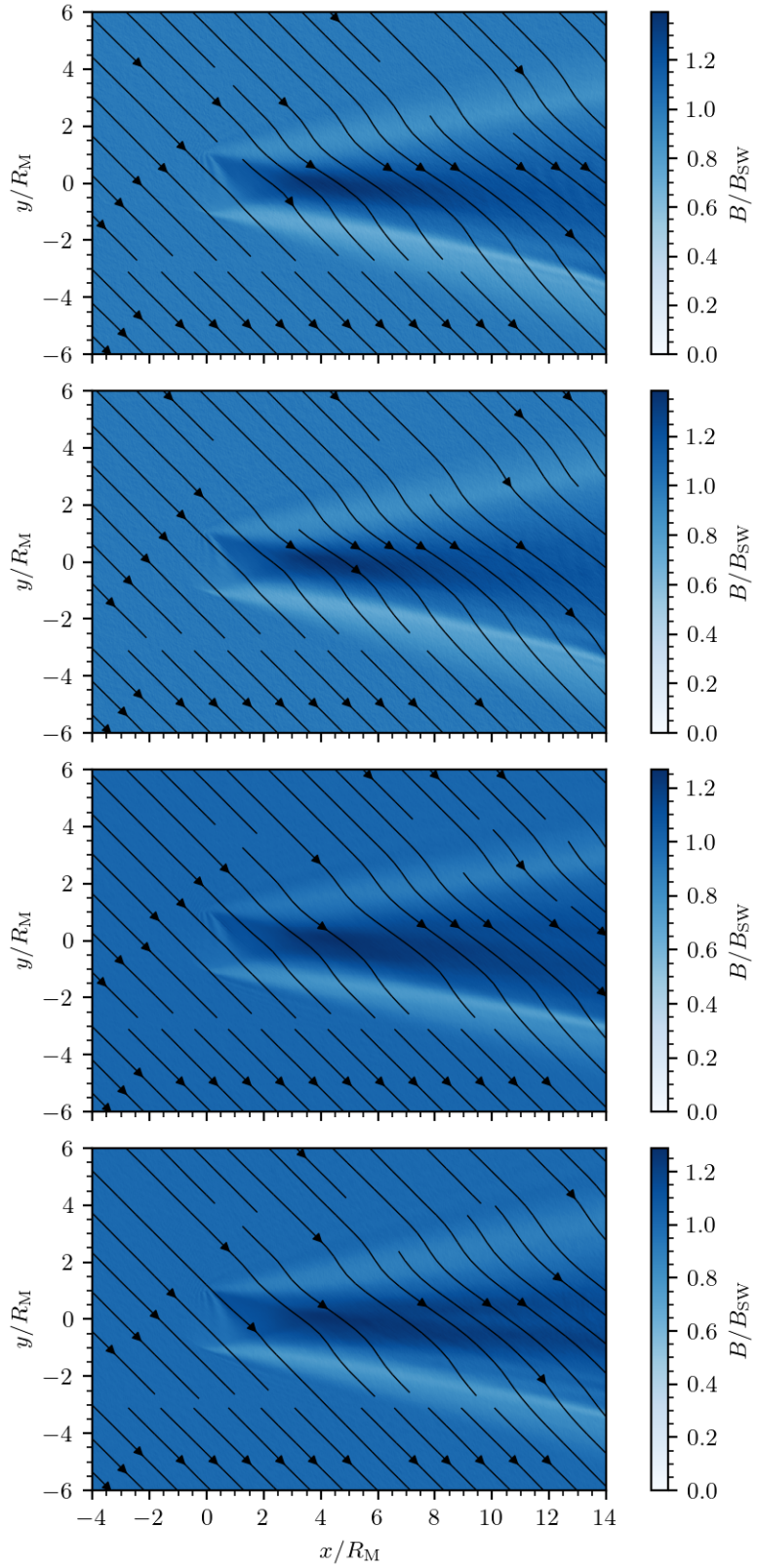

Figure 4.6: The comparison of magnetic field in between simulation runs 1 – 4.

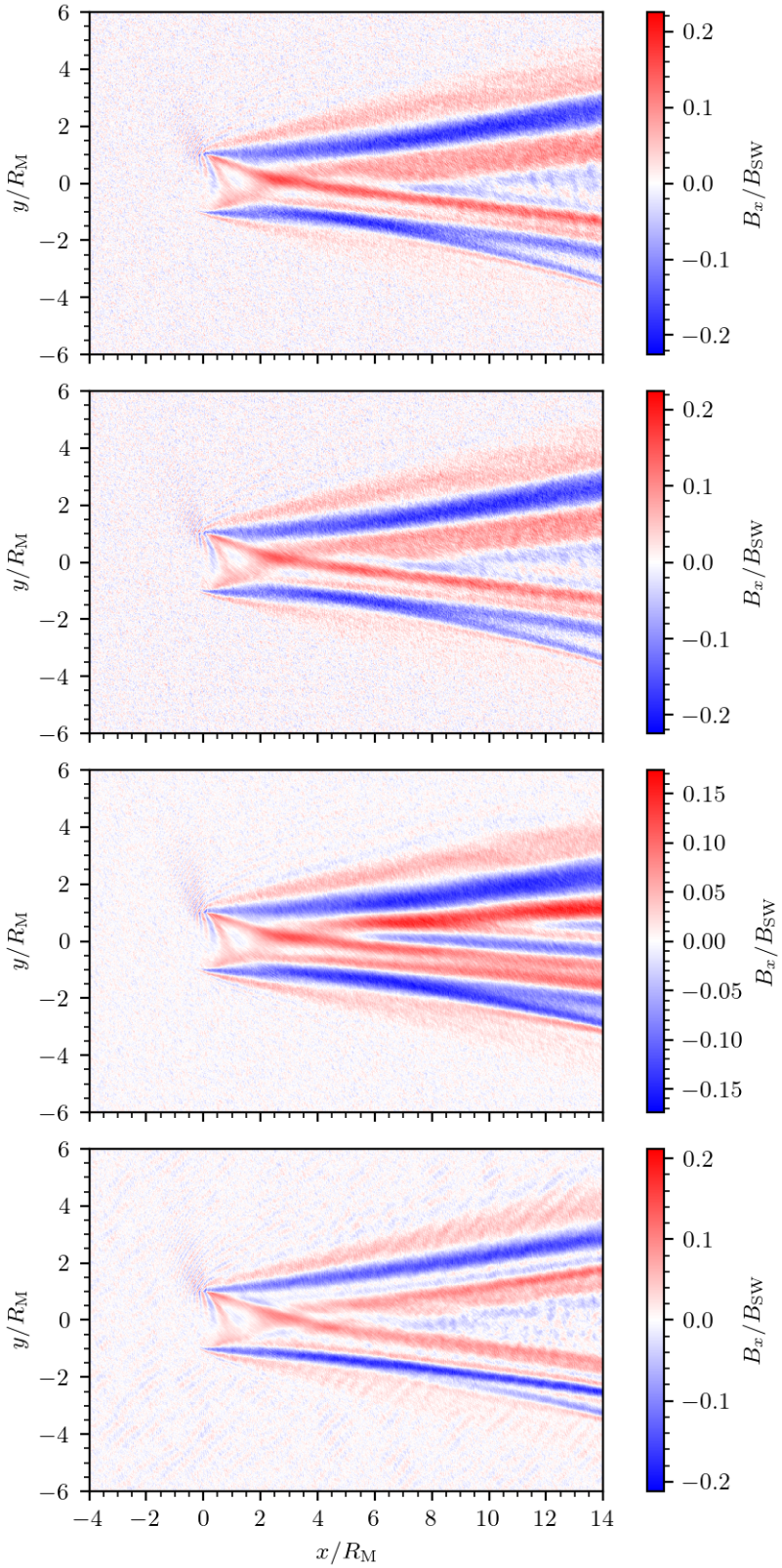

Figure 4.7: The comparison of B_z in between simulation runs 1 – 4.

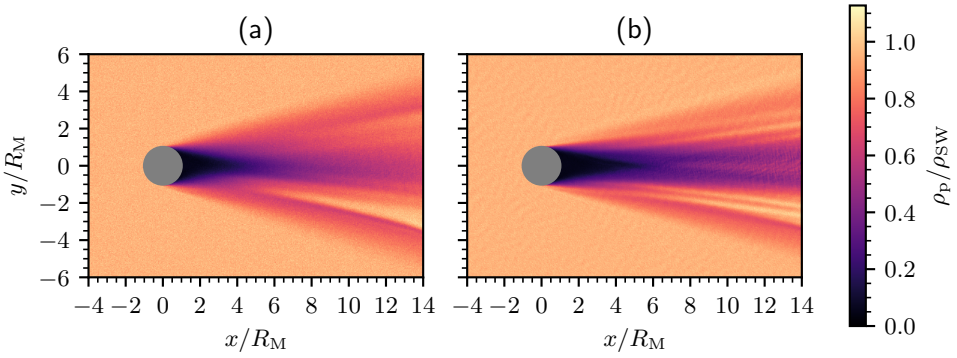

Figure 4.8: The comparison of proton charge density between simulation runs 1 and 4.

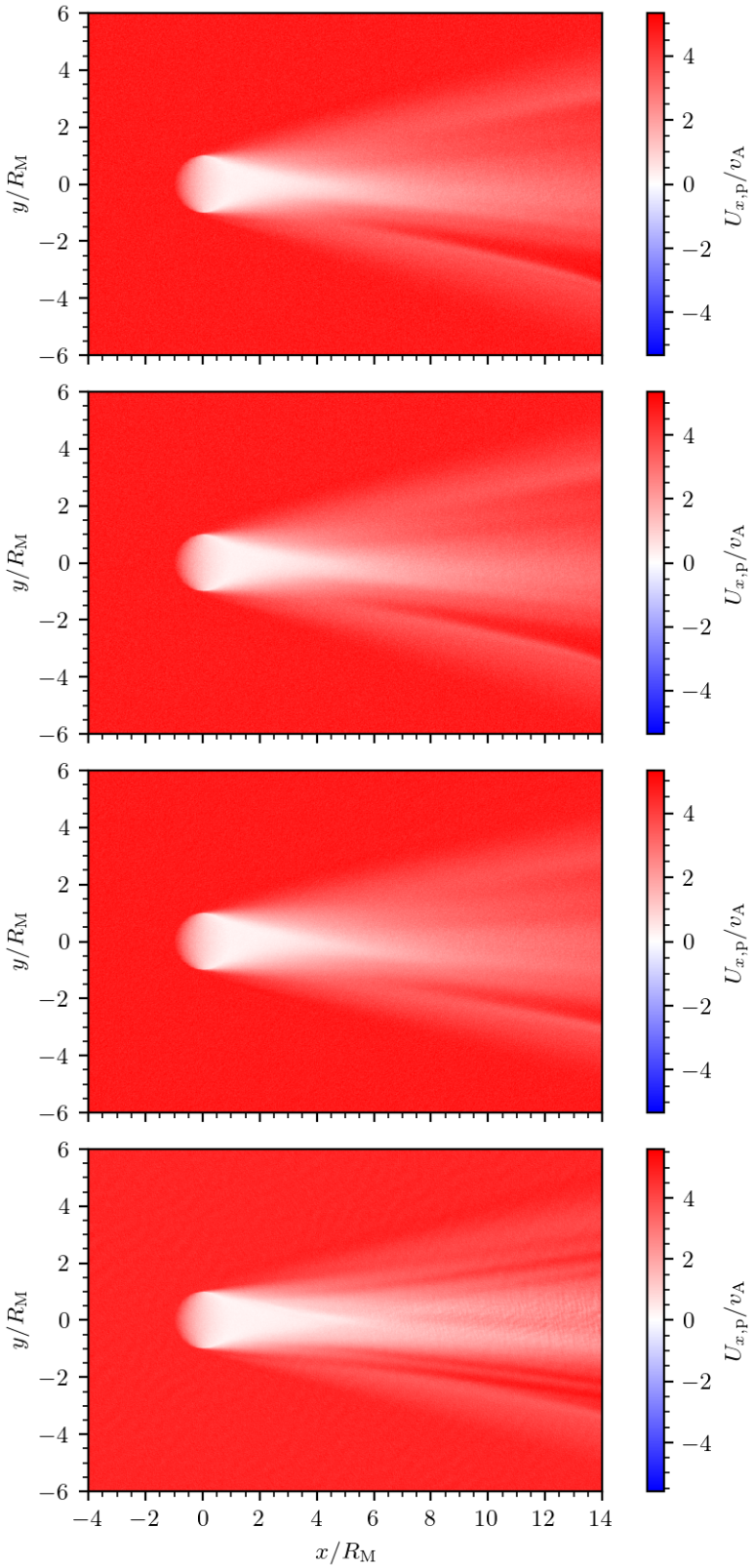

Figure 4.9: The comparison of the x-component of proton bulk velocity between simulation runs 1 – 4.

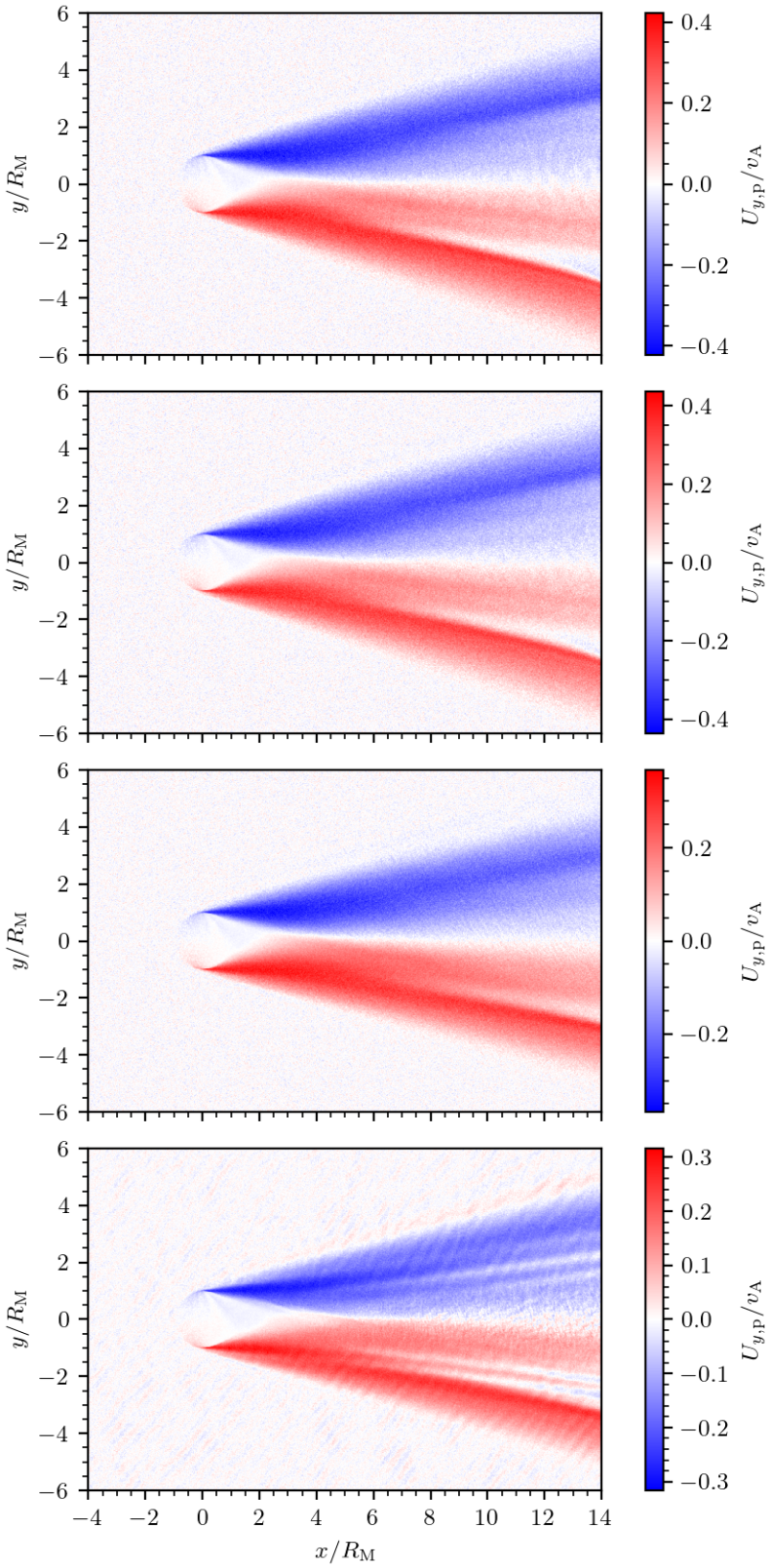

Figure 4.10: The comparison of the y-component of proton bulk velocity between simulation runs 1 – 4.

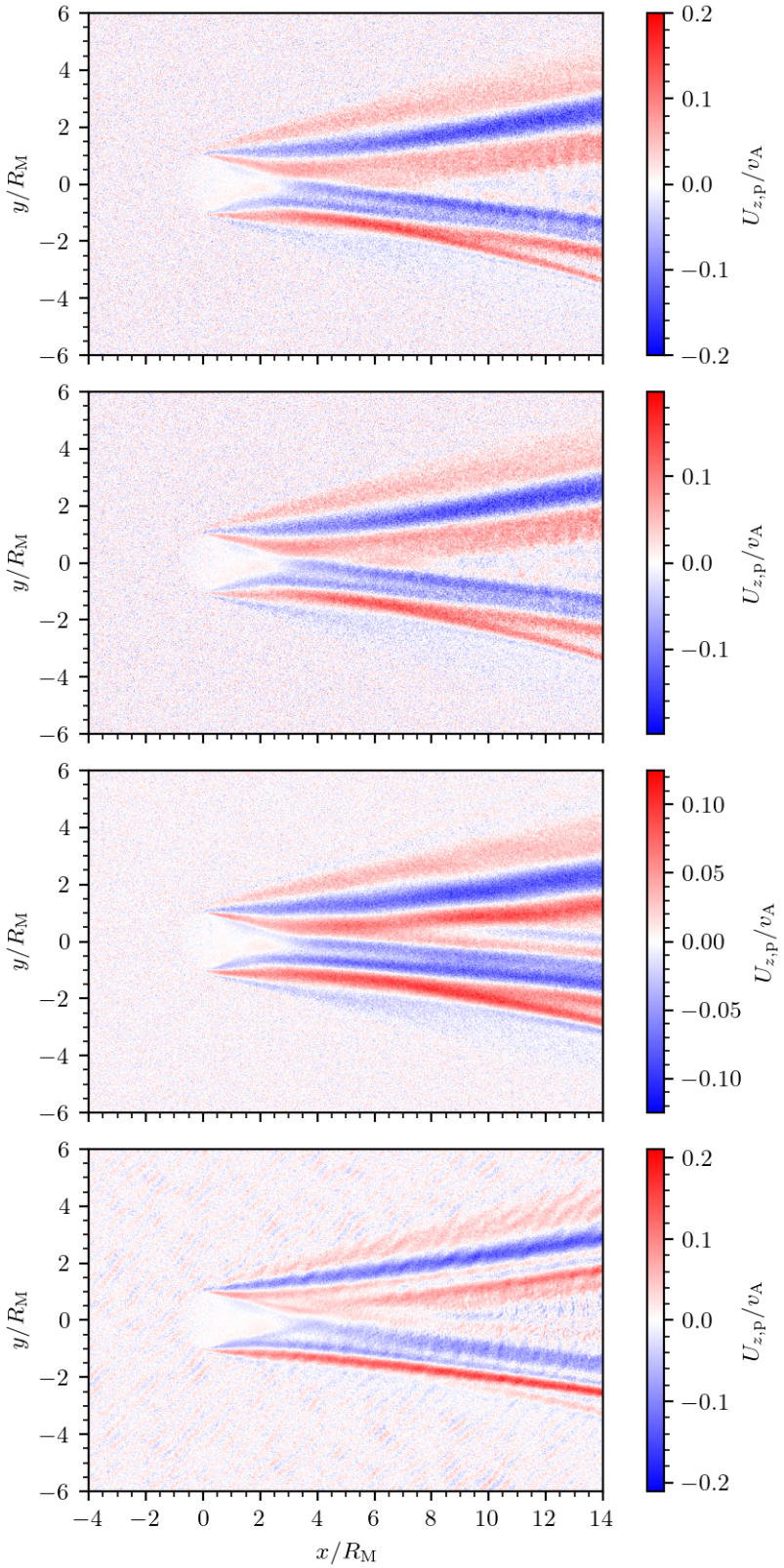

Figure 4.11: The comparison of the z-component of proton bulk velocity between simulation runs 1 – 4.

4.4 Instability Analysis

As discussed in Sections 2.3 and 2.7.4, the lunar wake is rich in instabilities. The ions refilling the void in the Moon's wake produce a two-stream instability, and, in the case of low $\beta_{\parallel}$, mirror and ion-cyclotron instabilities as well.

It is not straightforward to identify instabilities in the simulation results because of two reasons. One may use mathematical analysis to find whether there are unstable wave modes in the plasma – see Section 2.3. A problem with this approach is that the formulae for stability conditions and growth factors are derived under very strict conditions, which are not satisfied in the lunar wake. See for example the derivation in [23]. The lunar wake is not a uniform plasma near local thermodynamic equilibrium, as the refilling of the lunar wake is a non-equilibrium trasport process (and, in general, the solar wind is basically missing a major relaxation process – collisions). Therefore, the formulae presented in Section 2.3 may only serve as guidelines, but no certain conclusions may be made using them. A different approach might be to use visual clues in the graphs to make inferences about the existence and evolution of instabilities in the lunar wake. The unique geometry of the lunar wake makes this task unreliable as well.

Let us first consider the latter approach. In run 4, where the anisotropy and parallel beta are enahnced with respect to the normal conditions of the solar wind, the magnetic field (Figure 4.6) as well as the density of the hydrogen specie (Figure 4.8) feature a somewhat wave-like structure originating from the lunar wake outward, unlike in the other runs. In order to investigate possible unstable wave-modes, fast Fourier transform is used with the normalization

$$A_{kl} = \frac{1}{\sqrt{MN}} \sum_{m,n} a_{mn} \exp\left\{-2\pi \mathrm{i} \left(\frac{mk}{M} + \frac{nl}{N}\right)\right\}, \tag{4.1}$$

where a_{kl} is a node of a mesh representing the investigated quantity, M, N the dimensions of the mesh, and A_{kl} is a new mesh of complex quantity. This can be used to find the phase and amplitude of wave modes (see Section 2.3 for theoretical introduction). Figure 4.12 shows the amplitude of Fourier images of the components of magnetic fields. Subfigures (a,b,c) are the Fourier images of B_x, B_y, and B_z respectively in simulation run 1, which serves as a control in this case. The subject of investigation is the magnetic field in simulation run 4, whose x, y, and z components are shown in subgifures (d,e,f), respectively. The graphs on the right hand side, especially the graph of B_z from run 4, show a more pronounced wave structure. However, this merely indicates that complex wave phenomena occur.

Let us use the inequality for mirror mode instability (2.33) to define function

$$\Psi = 1 - \beta_{\perp}^2/\beta_{\parallel} - \beta_{\perp}. \tag{4.2}$$

For $\Psi \leq 0$, the plasma is stable, otherwise, the inequality (2.33) is satisfied and the plasma is mirror-unstable. The value of this function at each point

in the simulation run 4 at $t = 50\Omega_{\mathrm{p}}^{-1}$ is plotted in the top graph in Figure 4.13. The bottom graph is zoomed in and limited to the region

$$R \equiv 2.3R_{\mathrm{M}} < x < 9.2R_{\mathrm{M}}, \text{ and } -1.2R_{\mathrm{M}} < y < -0.6R_{\mathrm{M}}, \tag{4.3}$$

with $\Psi > 0$ colored uniformly in red. There is a relatively high abundance of points where Ψ is positive in this particular region in simulation run number 4. This marks the region as a candidate mirror instability, although, the derivation assumes an idealized situation and therefore, the region shall be treated as potentially unstable. Wherever *unstable region* is mentioned in this Section, it refers to area defined by (4.3).

In *Advanced Space Plasma Physics* [22], Treumann and Baumjohann plot 2D histograms of the quantities $\sum_s \beta_{s\perp}$ and $\sum_s \frac{\beta_{s\perp}^2}{\beta_{s\parallel}}$ to investigate the presence of mirror mode and perpendicular firehose mode in the solar wind. Figures 4.14,4.15,4.16,4.17 show the distribution in this histogram of cells in the results of simulations 1,2,3, and 4, respectively. For simulation run 4, there are areas in the near lunar wake ($2R_{\mathrm{M}} < x < 8R_{\mathrm{M}}$) and in the far lunar wake ($8R_{\mathrm{M}} < x < 14R_{\mathrm{M}}$), where the instability condition (shown in dotted line) is satisfied. Upstream of the lunar wake, the condition is not satisfied. This suggests that the conditions in the lunar wake are responsible for the wave phenomenon observed in the simulation results.

An approach that may provide more insight, used by e.g. *Hellinger et al.* [16] to find the potential for instabilities in the solar wind, is to estimate the growth rates of potential instabilities and plot them over histograms of parallel beta and proton anisotropy. These are plotted in figures 4.18. The curve $\gamma_{\max} \approx 10^{-3}$ shows the set of parameters for which the growth rate of mirror mode is 10^{-3}. Mesh points with $A, \beta_{\parallel}$ in the region to the right of that curve would have a growth rate larger than 10^{-3} and be mirror-unstable. This graph therefore serves as evidence to the contrary of having encoutered mirror mode instability in simulation run 4.

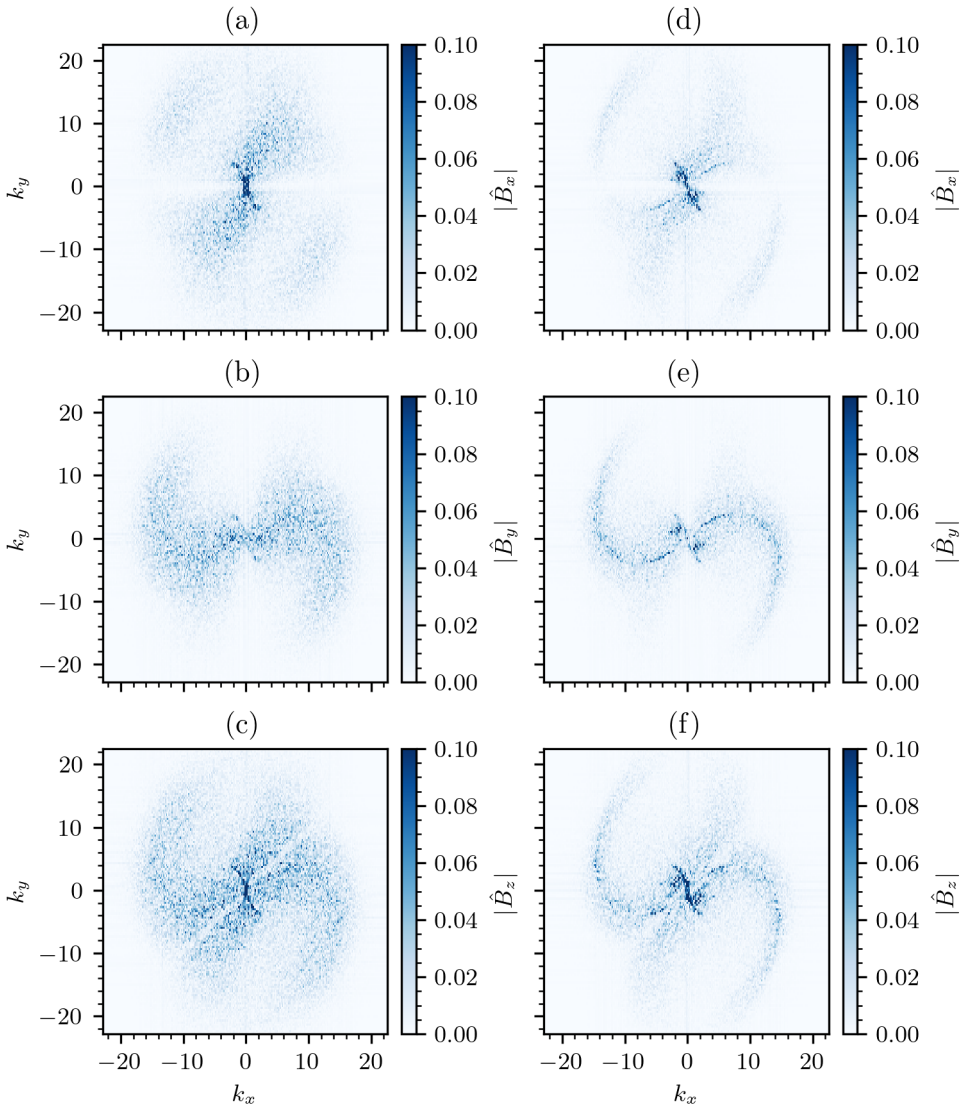

Figure 4.12: The amplitudes of fourier images of the components of magnetic fields. The left column shows the values in simulation run 1, while the right column shows the values in simulation run 4, where periodic structures occur more significantly.

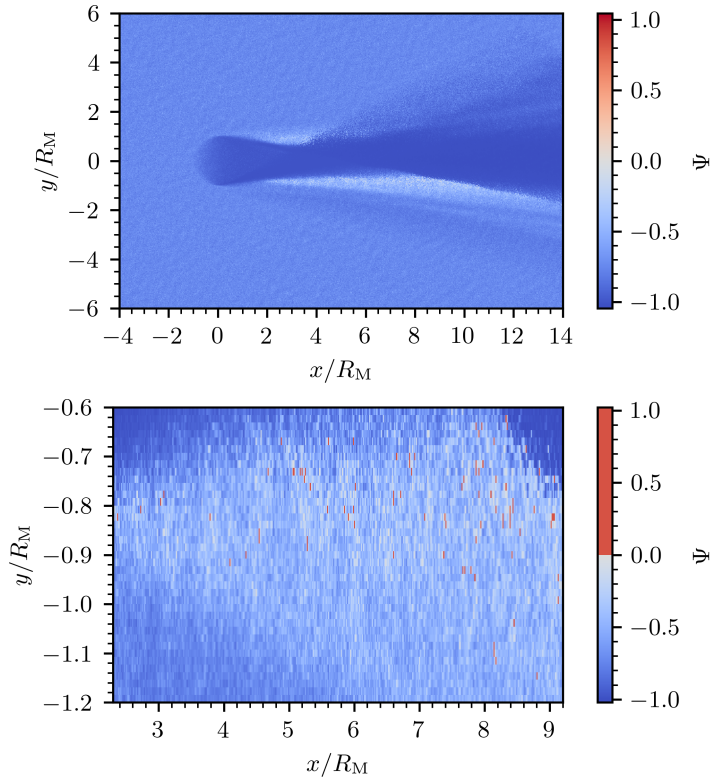

Figure 4.13: Graph of the function $\Psi = 1 - \beta_\perp^2/\beta_\parallel - \beta_\perp$ in simulation run 4. For $\Psi > 0$, the plasma is mirror-unstable.

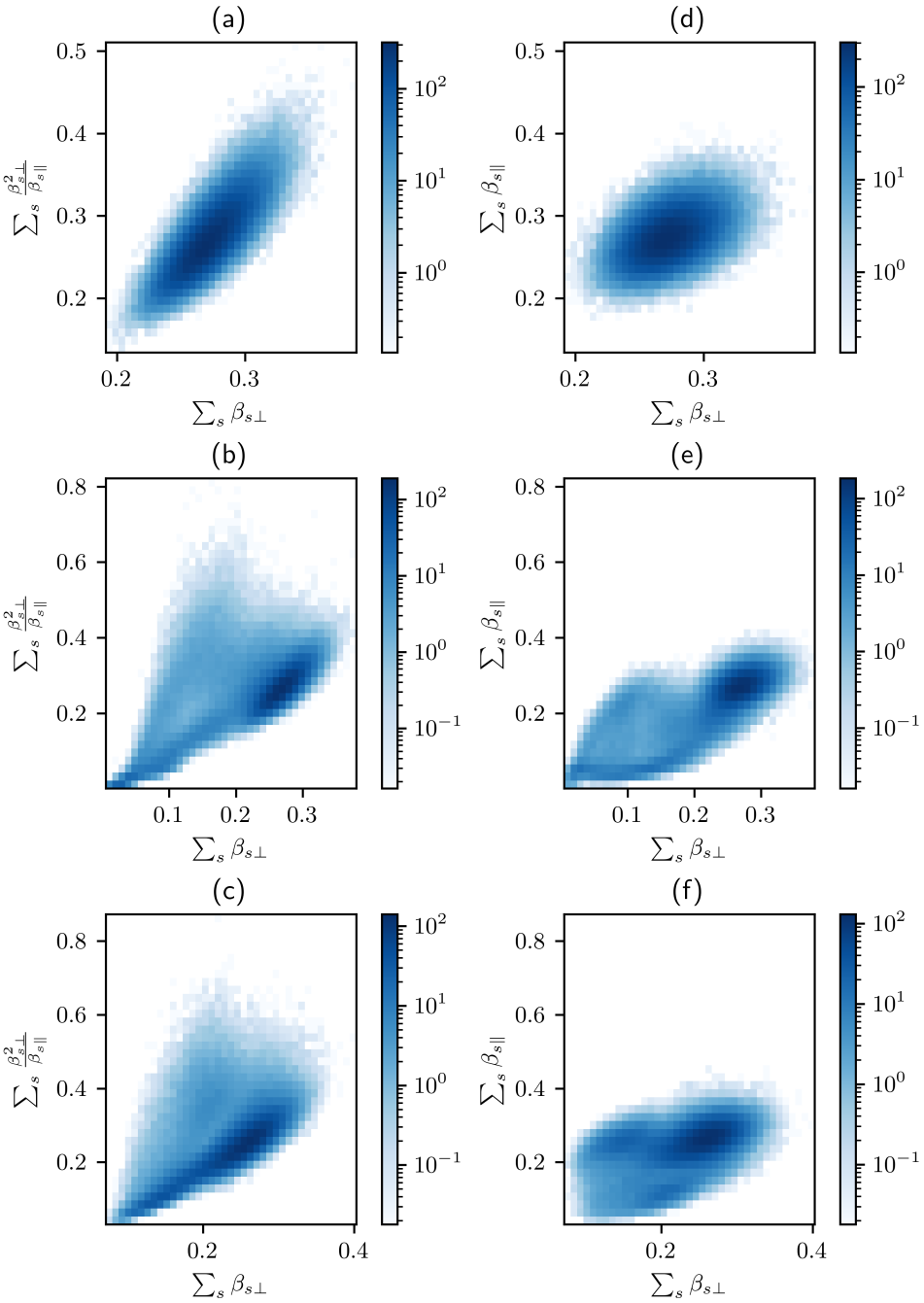

Figure 4.14: Histograms show the distribution of parameters relevant for the perpendicular mirror mode (a, b, c) and firehose mode (d, e, f) in simulation run 1. The rows correspond to upstream conditions (a, d), near lunar wake $2R_M < x < 8R_M$ (b, e), and far lunar wake $8R_M < x < 14R_M$ (c, f).

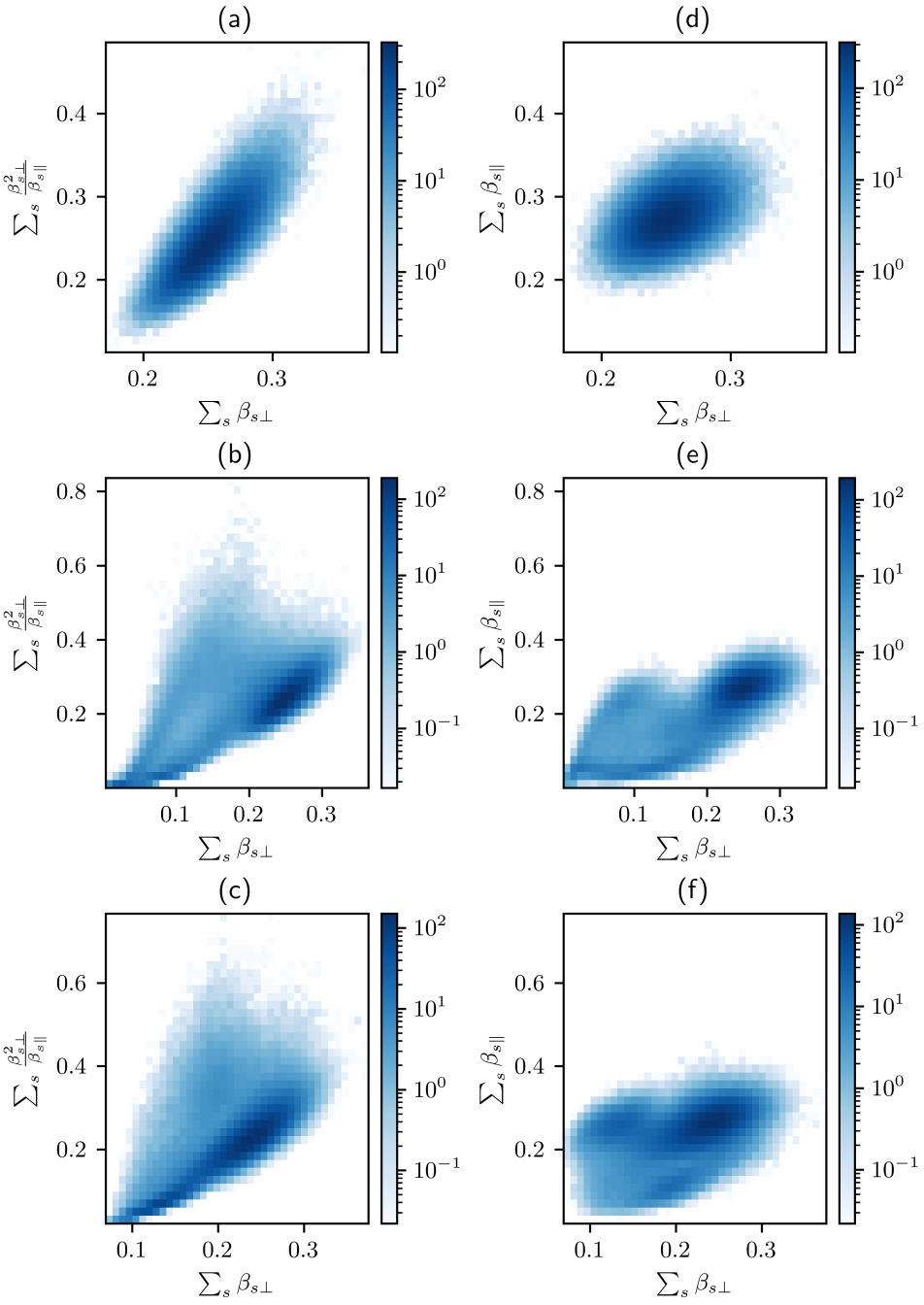

Figure 4.15: Histograms show the distribution of parameters relevant for the perpendicular mirror mode (a, b, c) and firehose mode (d, e, f) in simulation run 2. The rows correspond to upstream conditions (a, d), near lunar wake $2R_M < x < 8R_M$ (b, e), and far lunar wake $8R_M < x < 14R_M$ (c, f).

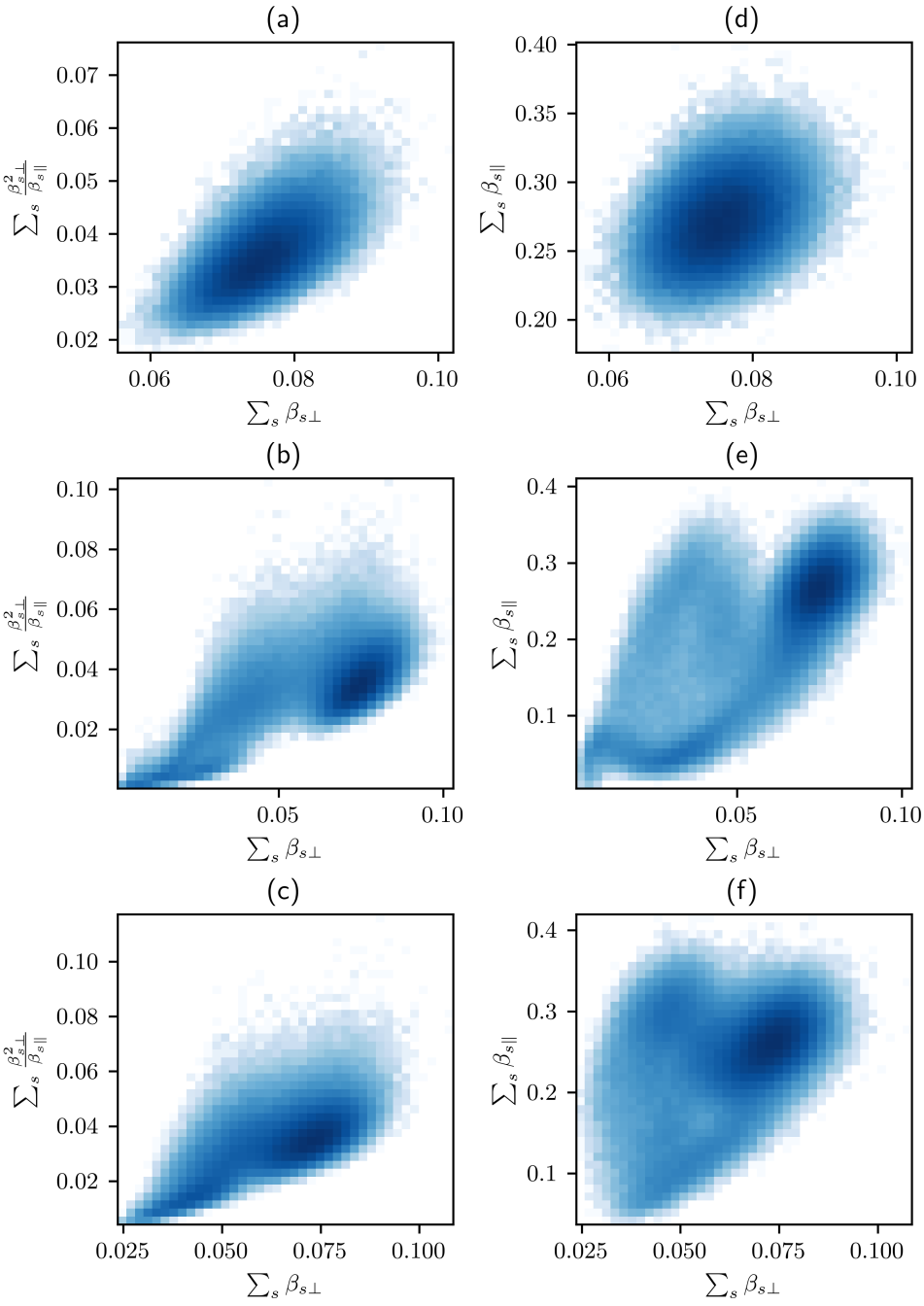

Figure 4.16: Histograms show the distribution of parameters relevant for the perpendicular mirror mode (a, b, c) and firehose mode (d, e, f) in simulation run 3. The rows correspond to upstream conditions (a, d), near lunar wake $2R_M < x < 8R_M$ (b, e), and far lunar wake $8R_M < x < 14R_M$ (c, f).

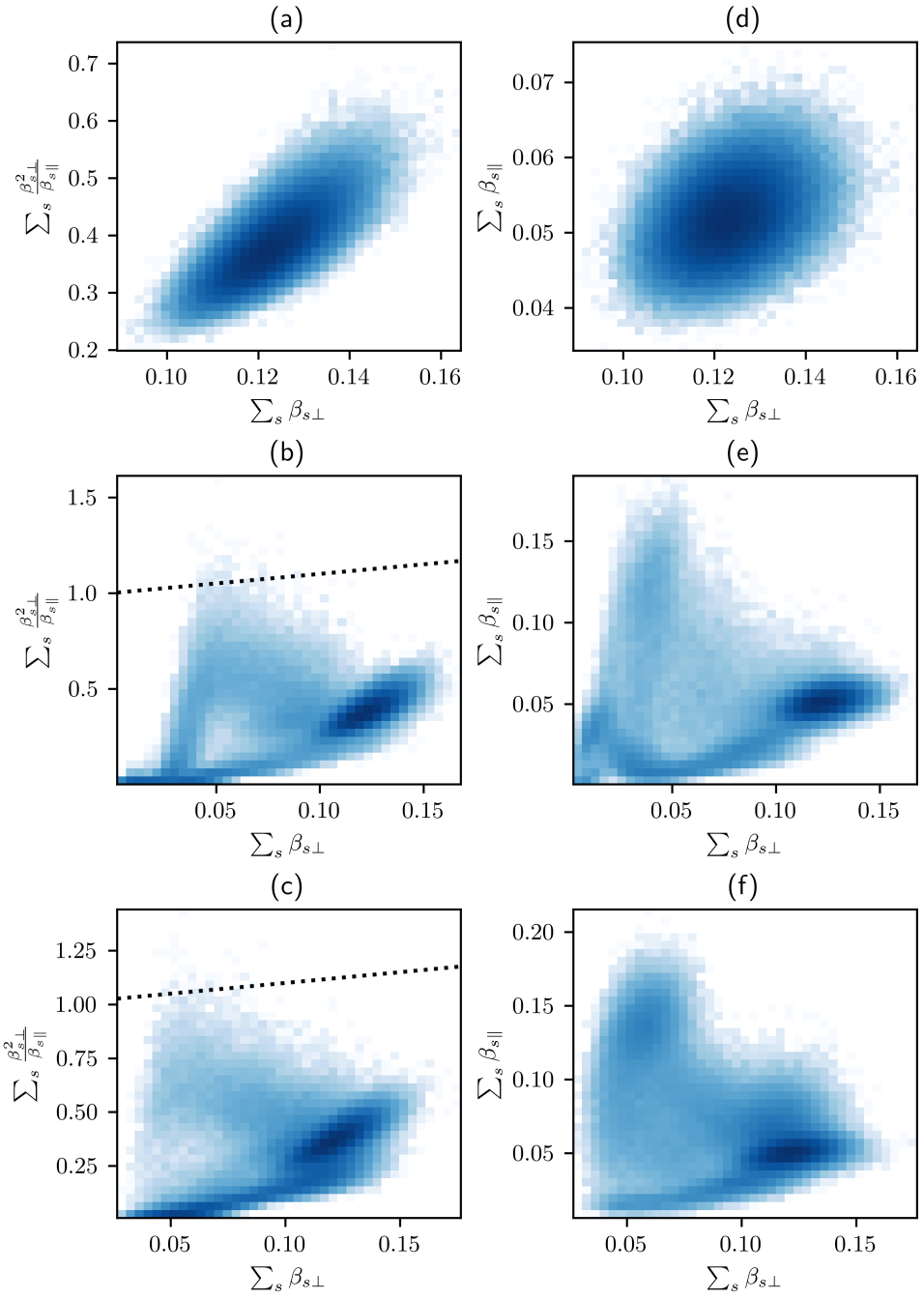

Figure 4.17: Histograms show the distribution of parameters relevant for the perpendicular mirror mode (a, b, c) and firehose mode (d, e, f) in simulation run 4. The rows correspond to upstream conditions (a, d), near lunar wake $2R_M < x < 8R_M$ (b, e), and far lunar wake $8R_M < x < 14R_M$ (c, f).

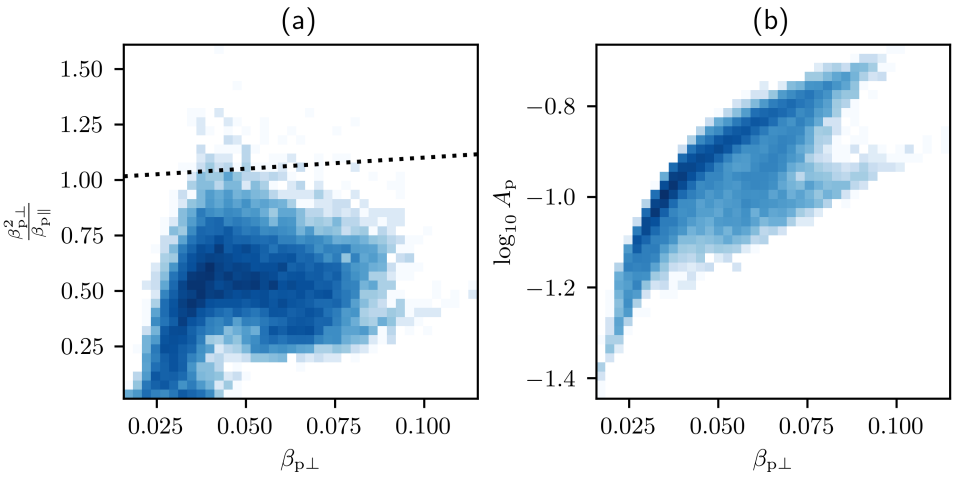

Figure 4.18: Histograms show the distribution of parameters relevant for the perpendicular mirror mode (a) and firehose mode (b) in simulation run 4 in the unstable region.

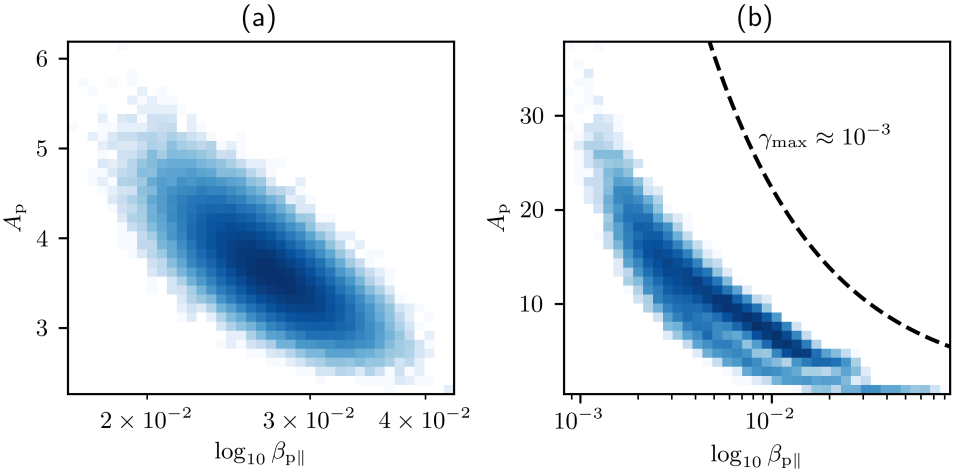

Figure 4.19: Histograms show the distribution of proton parallel beta and proton anisotropy in the upstream (a) and in the unstable region (b) in simulation 4.

4.5 Inductive Response

The influence of a conducting core on a two-specie wake was studied using run 5, where a conducting layer is added to the model with $\eta = 10^{-5}\mu_0 v_A^2/\Omega_p$, which is equivalent to $\sigma \sim 1 \times 10^5\,\mathrm{S\,m^{-1}}$ and a thickness of $0.3R_M$ that is smoothly transitioned into a background resistivity used throughout the simulation box. In this qualitative study, simulation run 1 will serve as a control.

The quantitites $\mathbf{B}$, ρ_H, u_H, A_H, $\mathbf{E}$, ρ_{He}, u_{He}, A_{He} at simulation time $t = 50\Omega_p^{-1}$ are shown in Figures A.11 and A.12 in the appendix.

The structure of the purely proton wake does not exhibit any differences in simulation run 5 as opposed to simulation run 1. However, there is a difference in the structure of the alpha wake, which is refilled at a slower rate as the alpha cavity extends further into the wake in run 5 compared to run 1. The typically high anisotropy in the region surroudning the low anisotropy center of the wake is not as pronounced in simulation run 1. The mechanism for these differences is unclear. An inductive response of the conducting lunar core would produce a strong magnetic signature. The comparison of the perturbation of the magnetic field by the lunar obstacle in the lunar wake of a non-conducting vs conducting Moon is featured in Figure 4.20. There are no significant changes to the magnetic structure of the wake. In order to show any possible subtle differences, cross-sections of the magnetic field with a constant x, similar to those in Section 4.2, are plotted in Figure 4.21. Any differences between the magnetic field signatures are in the order of digital noise.

A possible source of a simulation artifact caused by the boundary conditions applied on the lunar surface and the lunar interior could be the diferent electric field in the lunar core accelerating particles at a different rate, because particles intersecting the lunar surface are not removed instantly, but only marked for removal from the simulation in order to conserve numerical stability (see Section 3.2). However, the presence of this artifact would likely also have a similarly strong impact on the proton part of the wake.

Ideally, a steep change in the magnetic field would be initialized upstream of the lunar obstacle, as done by [70]. Due to numerical dispersivity of the scheme used, a shock wave in the magnetic field led to a numerical instability. For this reason, only a weak inductive response was to be expected from the Moon in this simulation setup.

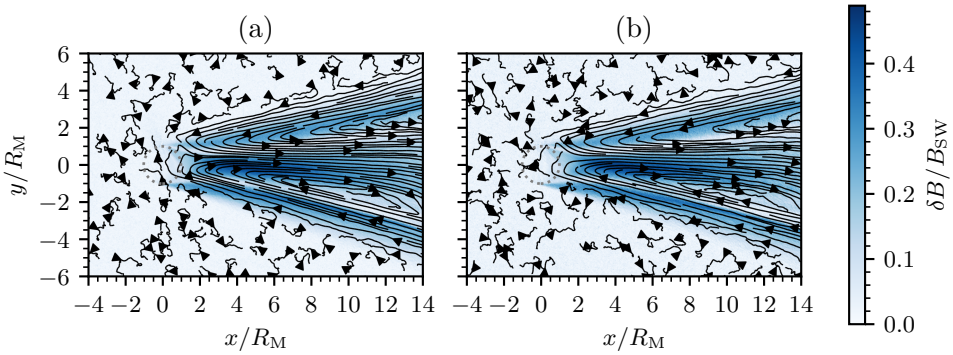

Figure 4.20: Figures (a) and (b) show the magnetic field perturbation in the lunar wake in the case of (a) Moon with background resistivity and (b) Moon with a conducting core (i.e. simulation run 5), respectively. The field lines are plotted in the xy plane and therefore do not show the contribution of B_z; it is however inclued in the magnitude B of the magnetic field, plotted in shades of blue.

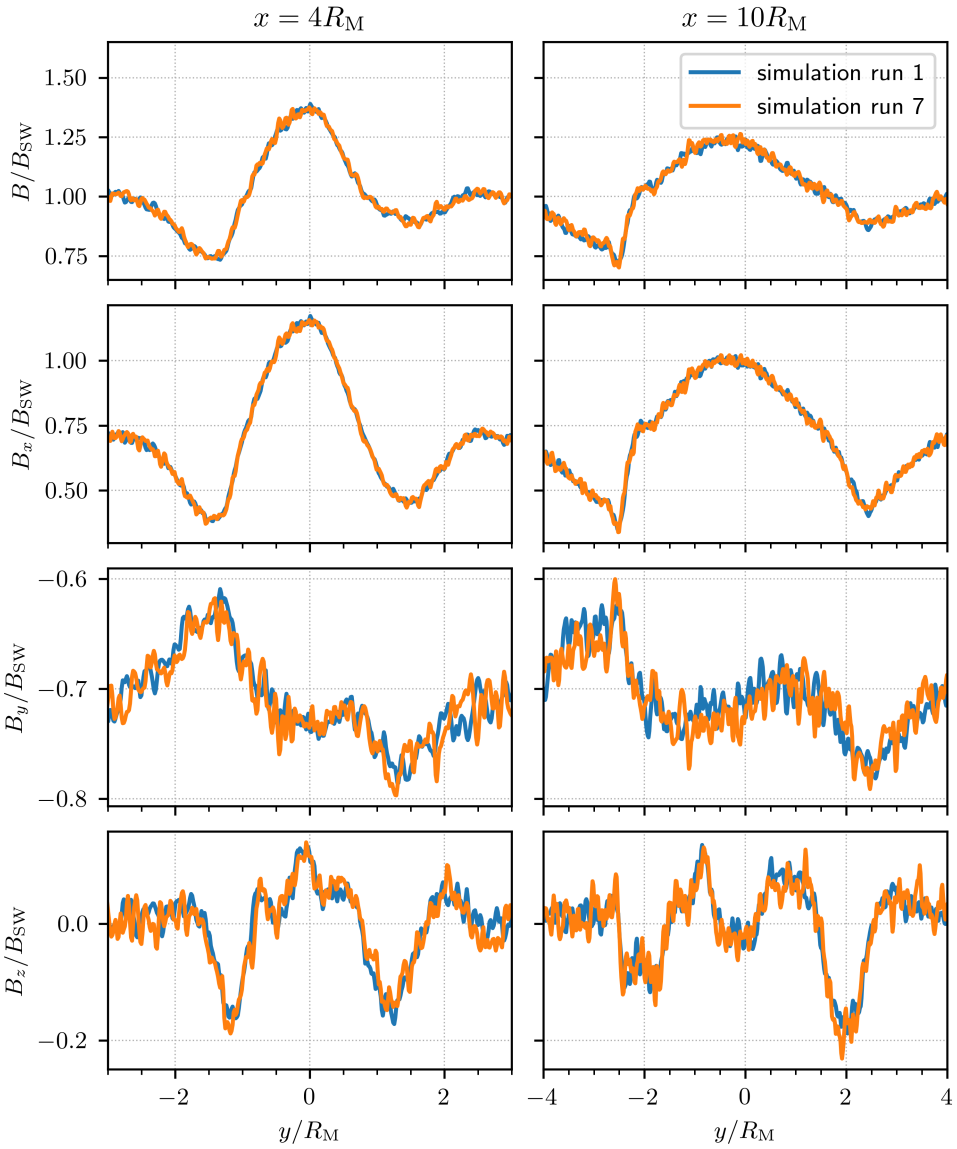

Figure 4.21: he cross sections of magnetic field amplitude and directional components. Simulation run 1 (non-conducting Moon) is in blue and simulation run 5 (conducting Moon) is in orange.

4.6 Justification of Helium Negligence in Lunar Wake Models

The helium ion specie is usually omitted in lunar wake models, with the justification that the concentration of helium in the solar wind is typically below 5 %[1], and because of the low charge/mass ratio, their interaction with the electromagnetic field is even weaker.

The usefulness of this negligence is generally supported by the comparison of simulation runs 1 and 0. The general structure of the lunar wake remains the same without the presence of alpha particles in the model – see Figures 4.3 and 4.1, with differences noticeable in the sections in Figures 4.4 and 4.5. The presence of alpha particles does not appear to play a major role in the model with a conducting lunar core, either. This may, however, be due to the fact that the external magnetic field is not changing, as discussed in my bachelor's thesis. To truly investigate the justification of the negligence of alpha particles in the lunar wake, ideally, a model with periodically changing upstream boundary condition for the magnetic field should be used. Due to the dispersive properties of the scheme used in this study with regard to a shock wave in magnetic field, this was not achieved in this thesis as the simulations terminated due to numerical instability.

It does, therefore, seem that the negligence of alpha particles in lunar wake models is justified under some circumstances – e.g. studies of global properties of the lunar wake. In some cases, it may not be advisable, as there are several open questions as to the influence of alpha particles which are beyond the scope of this thesis. For example, it has been suggested that type-II protons that enter the lunar wake after reflecting from the lunar surface fields may contribute to the formation of instabilities (see Section 2.7 for further details). An analogous mechanism may apply to alpha particles that reflect from the lunar surface. Also, any phenomenon that might me sensitive to the slight $-y$-ward shift of magnetic field signatures due to the $-y$-ward drifting alpha particle specie – see Section 4.2 – would be modeled incorrectly.

[1] For typical concetrations of ion species in the solar wind, see Section 2.1

Chapter 5

Conclusion

The interaction of the solar wind with the Moon has traditionally been modeled using a hybrid model with alpha particles omitted from the modeling. The ions of the solar wind are constituted by 5 % of alpha particles, however, moving with respect to the bulk of ions with an average velocity of $0.67v_{\mathrm{A}}$. The question then arises whether the effects of alpha particles in the lunar wake interaction are negligible. This thesis therefore focused on the modeling of the lunar wake without the negligence of alpha particles. A CAM–CL scheme was used to solve a 2.5 dimensional multi-ion-specie hybrid model (protons and alpha particles as macro-particles, electrons as a massless fluid) of the interaction on a 2200×900 mesh with $\Delta x = \Delta y = 0.2d_{\mathrm{p}}$ and $\Delta t = 0.01\Omega_{\mathrm{p}}^{-1}$ in a total of 6 simulation runs.

The negligence of alpha particles does not seem to have a strong effect on the general structure of the lunar wake. The perturbations of the magnetic field as well as the ionic number densities, bulk velocities, and temperature anisotropies, are enveloped by a Mach cone with an apex angle of $\approx 20°$, approximately the same angle as in the control case (a purely proton lunar wake simulation). The number density profile of the alpha specie is highly asymmetrical, contrary to that of the proton specie. The plasma cavity in the alpha specie has an angle of approximately $\approx 5°$ toward $-y$ direction, which is corresponding to the bulk velocity of alpha particles in the unperturbed solar wind. The recompression region as well as the rarefactional wave are present on both flanks of the asymmetrical alpha wake, however, the recompression region on the $+y$ flank is strongly enhanced.

All directional components of the magnetic field are slightly shifted by $\lessapprox 0.1R_{\mathrm{L}}$ toward $-y$. This is likely due to diamagnetic currents caused by a gradient in alpha-particle pressure. Further, B_z peaks in the $+y$ section of the far wake are suppresed by the alpha particle specie. The addition of alpha particles to the model also has an influence, albeit less significant, on the protonic bulk velocity in the z-direction, $u_{z,\mathrm{p}}$, but not on $u_{x,\mathrm{p}}, u_{y,\mathrm{p}}$.

These observations of the hybrid model with alpha particles not neglected therefore suggest that alpha particles should probably not be omitted from models of the lunar wake. However, because the most significant influence to the protonic specie bulk velocity as well as the magnetic field is in the z-direction, which was not modeled fully, the negligence of alpha particles

needs to be compared in a 3-dimensional model to support or rule out this assertion.

The addition of alpha particles alone to the model did not produce any instabilities apart from the two-stream instability typical for the lunar wake that is produced by the ion beams refilling the lunar plasma void. For this reason, simulation runs 2, 3, and 4, initialized at different points in the $(A, \beta_{\parallel})$ space of both particle species, were used. These configurations were chosen with respect to conditions common in the solar wind.

Increased anisotropy of the alpha specie did not cause a significant perturbance to the structure of the wake. However, for highly anisotropic solar wind protons, what seems to be a mirror instability was produced in the simulation. The observed effect was a wave-like disturbance in proton charge density emanating outward from the central wake on both flanks of the proton wake. The indicator that the observations are caused by the mirror instability is the fulfilling of mirror mode instability condition (2.33) for regions on the $-y$ flank of the wake, where the wave-like structure is more pronounced. However, the instability condition (2.33) is derived under assumptions which do not hold in the lunar wake. Therefore, strong conclusions cannot be made about the origin and nature of this possible instability.

The influence of a conducting lunar lunar core on a solar wind with the presence of alpha particles was studied in a simulation in which a conducting layer was added with $\eta = 10^{-5}\mu_0 v_{\mathrm{A}}^2/\Omega_{\mathrm{p}}, R = 0.3R_{\mathrm{M}}$. The proton specie was not influenced differently from a simulation without the conducting core model. The alpha wake cavity is prolonged, without any indication of an effect of the proton specie. It is possible that this is a simulation artifact produced by the handling of lunar boundary conditions. The reason for this conclusion is that the proton density seems not to be influenced, neither are there any significant perturbances to the magnetic field, typical for an induction response. It is expected that if there was an induction response in the model, it would not be very strong under the conditions used in the simulation set up. A better set up was not achieved however, due to numerical instability issues.

Bibliography

[1] M. G. Kivelson and C. T. Russell, Eds., *Introduction to space physics*, Cambridge ; New York: Cambridge University Press, 1995, 568 pp., ISBN: 978-0-521-45104-8 978-0-521-45714-9.

[2] J. G. Luhmann, S. A. Ledvina, and C. T. Russell, "Induced magnetospheres", *Advances in Space Research*, Comparative Magnetospheres, vol. 33, no. 11, pp. 1905–1912, Jan. 1, 2004, ISSN: 0273-1177. DOI: 10.1016/j.asr.2003.03.031.

[3] E. W. Greenstadt, "Conditions for magnetic interaction of asteroids with the solar wind", *Icarus*, vol. 14, no. 3, pp. 374–381, Jun. 1, 1971, ISSN: 0019-1035. DOI: 10.1016/0019-1035(71)90008-X.

[4] Z. Wang and M. G. Kivelson, "Asteroid interaction with solar wind", *Journal of Geophysical Research: Space Physics*, vol. 101, pp. 24 479–24 493, A11 1996, ISSN: 2156-2202. DOI: 10.1029/96JA02019.

[5] N. Omidi, X. Blanco-Cano, C. T. Russell, H. Karimabadi, and M. Acuna, "Hybrid simulations of solar wind interaction with magnetized asteroids: General characteristics", *Journal of Geophysical Research: Space Physics*, vol. 107, SSH 12–1–SSH 12–10, A12 2002, ISSN: 2156-2202. DOI: 10.1029/2002JA009441.

[6] S. Simon, T. Bagdonat, U. Motschmann, and K.-H. Glassmeier, "Plasma environment of magnetized asteroids: A 3-d hybrid simulation study", *Annales Geophysicae*, vol. 24, no. 1, pp. 407–414, Mar. 7, 2006, ISSN: 1432-0576. DOI: 10.5194/angeo-24-407-2006.

[7] K. Szegö, K.-H. Glassmeier, R. Bingham, *et al.*, "Physics of mass loaded plasmas", *Space Science Reviews*, vol. 94, no. 3, pp. 429–671, Dec. 1, 2000, ISSN: 1572-9672. DOI: 10.1023/A:1026568530975.

[8] J. Geiss and H. Reeves, "Cosmic and solar system abundances of deuterium and helium-3", *åp*, vol. 18, p. 126, Apr. 1972.

[9] D. Verscharen, K. G. Klein, and B. A. Maruca, "The multi-scale nature of the solar wind", *Living Reviews in Solar Physics*, vol. 16, no. 1, p. 5, Dec. 9, 2019, ISSN: 1614-4961. DOI: 10.1007/s41116-019-0021-0.

[10] N. E. Papitashvili and J. H. King, *OMNI hourly data set*, 2020. DOI: 10.48322/1SHR-HT18.

[11] F. Xu and J. E. Borovsky, "A new four-plasma categorization scheme for the solar wind", *Journal of Geophysical Research: Space Physics*, vol. 120, no. 1, pp. 70–100, 2015, ISSN: 2169-9402. DOI: 10.1002/2014JA020412.

[12] E. Camporeale, A. Carè, and J. E. Borovsky, "Classification of solar wind with machine learning", *Journal of Geophysical Research: Space Physics*, vol. 122, no. 11, pp. 10, 910–10, 920, 2017, ISSN: 2169-9402. DOI: 10.1002/2017JA024383.

[13] D. B. Reisenfeld, R. C. Wiens, B. L. Barraclough, *et al.*, "Solar wind conditions and composition during the genesis mission as measured by in situ spacecraft", *Space Science Reviews*, vol. 175, no. 1, pp. 125–164, Jun. 2013, ISSN: 0038-6308, 1572-9672. DOI: 10.1007/s11214-013-9960-2.

[14] G. Livadiotis and D. J. McComas, "Understanding kappa distributions: A toolbox for space science and astrophysics", *Space Science Reviews*, vol. 175, no. 1, pp. 183–214, Jun. 1, 2013, ISSN: 1572-9672. DOI: 10.1007/s11214-013-9982-9.

[15] B. L. Alterman, J. C. Kasper, M. L. Stevens, and A. Koval, "A comparison of alpha particle and proton beam differential flows in collisionally young solar wind", *The Astrophysical Journal*, vol. 864, no. 2, p. 112, Sep. 2018, ISSN: 0004-637X. DOI: 10.3847/1538-4357/aad23f.

[16] P. Hellinger, P. Trávníček, J. C. Kasper, and A. J. Lazarus, "Solar wind proton temperature anisotropy: Linear theory and WIND/SWE observations", *Geophysical Research Letters*, vol. 33, no. 9, 2006, ISSN: 1944-8007. DOI: 10.1029/2006GL025925.

[17] J. C. Kasper, A. J. Lazarus, and S. P. Gary, "Wind/SWE observations of firehose constraint on solar wind proton temperature anisotropy", *Geophysical Research Letters*, vol. 29, no. 17, pp. 20–1–20–4, 2002, ISSN: 1944-8007. DOI: 10.1029/2002GL015128.

[18] J. C. Kasper, M. L. Stevens, A. J. Lazarus, J. T. Steinberg, and K. W. Ogilvie, "Solar wind helium abundance as a function of speed and heliographic latitude: Variation through a solar cycle", *The Astrophysical Journal*, vol. 660, no. 1, p. 901, May 1, 2007, ISSN: 0004-637X. DOI: 10.1086/510842.

[19] L. B. W. III, L.-J. Chen, S. Wang, *et al.*, "Electron energy partition across interplanetary shocks. i. methodology and data product", *The Astrophysical Journal Supplement Series*, vol. 243, no. 1, p. 8, Jul. 2019, ISSN: 0067-0049. DOI: 10.3847/1538-4365/ab22bd.

[20] V. Pierrard, M. Lazar, S. Poedts, Š. Štverák, M. Maksimovic, and P. M. Trávníček, "The electron temperature and anisotropy in the solar wind. comparison of the core and halo populations", *Solar Physics*, vol. 291, no. 7, pp. 2165–2179, Aug. 1, 2016, ISSN: 1573-093X. DOI: 10.1007/s11207-016-0961-7.

[21] J. V. Hollweg, "Waves and instabilities in the solar wind", *Reviews of Geophysics*, vol. 13, no. 1, pp. 263–289, 1975, ISSN: 1944-9208. DOI: 10.1029/RG013i001p00263.

[22] R. A. Treumann and W. Baumjohann, *Advanced space plasma physics*, Reprinted. London: Imperial College Press, 2001, 381 pp., ISBN: 978-1-86094-026-2.

[23] W. Baumjohann and R. A. Treumann, *Basic space plasma physics*, Reprinted. London: Imperial College Press, 2006, 329 pp., ISBN: 978-1-86094-079-8.

[24] M. Cuk and S. T. Stewart, "Making the moon from a fast-spinning earth: A giant impact followed by resonant despinning", *Science*, vol. 338, no. 6110, pp. 1047–1052, Nov. 23, 2012, ISSN: 0036-8075, 1095-9203. DOI: 10.1126/science.1225542.

[25] B. P. Weiss and S. M. Tikoo, "The lunar dynamo", *Science*, vol. 346, no. 6214, p. 1 246 753, Dec. 5, 2014. DOI: 10.1126/science.1246753.

[26] C. Suavet, B. P. Weiss, W. S. Cassata, *et al.*, "Persistence and origin of the lunar core dynamo", *Proceedings of the National Academy of Sciences*, vol. 110, no. 21, pp. 8453–8458, May 21, 2013. DOI: 10.1073/pnas.1300341110.

[27] S. Mighani, H. Wang, D. L. Shuster, C. S. Borlina, C. I. O. Nichols, and B. P. Weiss, "The end of the lunar dynamo", *Science Advances*, vol. 6, no. 1, eaax0883, Jan. 3, 2020, ISSN: 2375-2548. DOI: 10.1126/sciadv.aax0883.

[28] L. Schaefer and L. T. Elkins-Tanton, "Magma oceans as a critical stage in the tectonic development of rocky planets", *Philosophical Transactions of the Royal Society A: Mathematical, Physical and Engineering Sciences*, vol. 376, no. 2132, p. 20 180 109, Nov. 13, 2018. DOI: 10.1098/rsta.2018.0109.

[29] L. T. Elkins-Tanton, S. Burgess, and Q.-Z. Yin, "The lunar magma ocean: Reconciling the solidification process with lunar petrology and geochronology", *Earth and Planetary Science Letters*, vol. 304, no. 3, pp. 326–336, Apr. 2011, ISSN: 0012821X. DOI: 10.1016/j.epsl.2011.02.004.

[30] H. Hiesinger, J. W. Head III, U. Wolf, R. Jaumann, and G. Neukum, "Ages and stratigraphy of mare basalts in oceanus procellarum, mare nubium, mare cognitum, and mare insularum", *Journal of Geophysical Research: Planets*, vol. 108, E7 2003, ISSN: 2156-2202. DOI: 10.1029/2002JE001985.

[31] J. Saur, F. M. Neubauer, and K.-H. Glassmeier, "Induced magnetic fields in solar system bodies", *Space Science Reviews*, vol. 152, no. 1, pp. 391–421, Dec. 2009. DOI: 10.1007/s11214-009-9581-y.

[32] H. Shimizu, M. Matsushima, F. Takahashi, H. Shibuya, and H. Tsunakawa, "Constraint on the lunar core size from electromagnetic sounding based on magnetic field observations by an orbiting satellite", *Icarus*, vol. 222, no. 1, pp. 32–43, Jan. 1, 2013, ISSN: 0019-1035. DOI: 10.1016/j.icarus.2012.10.029.

[33] D. G. Sibeck, V. Angelopoulos, D. A. Brain, *et al.*, "ARTEMIS science objectives", *Space Science Reviews*, vol. 165, no. 1, pp. 59–91, Dec. 1, 2011, ISSN: 1572-9672. DOI: 10.1007/s11214-011-9777-9.

[34] A. Khan, J. A. D. Connolly, N. Olsen, and K. Mosegaard, "Constraining the composition and thermal state of the moon from an inversion of electromagnetic lunar day-side transfer functions", *Earth and Planetary Science Letters*, vol. 248, no. 3, pp. 579–598, Aug. 30, 2006, ISSN: 0012-821X. DOI: 10.1016/j.epsl.2006.04.008.

[35] C. Nunn, R. F. Garcia, Y. Nakamura, *et al.*, "Lunar seismology: A data and instrumentation review", *Space Science Reviews*, vol. 216, no. 5, p. 89, Jul. 3, 2020, ISSN: 1572-9672. DOI: 10.1007/s11214-020-00709-3.

[36] R. Jaumann, H. Hiesinger, M. Anand, *et al.*, "Geology, geochemistry, and geophysics of the moon: Status of current understanding", *Planetary and Space Science*, Scientific Preparations For Lunar Exploration, vol. 74, no. 1, pp. 15–41, Dec. 1, 2012, ISSN: 0032-0633. DOI: 10.1016/j.pss.2012.08.019.

[37] V. Viswanathan, N. Rambaux, A. Fienga, J. Laskar, and M. Gastineau, "Observational constraint on the radius and oblateness of the lunar core-mantle boundary", *Geophysical Research Letters*, vol. 46, no. 13, pp. 7295–7303, 2019, ISSN: 1944-8007. DOI: 10.1029/2019GL082677.

[38] M. A. Wieczorek, B. L. Jolliff, A. Khan, *et al.*, "The constitution and structure of the lunar interior", *Reviews in Mineralogy and Geochemistry*, vol. 60, no. 1, pp. 221–364, Jan. 1, 2006, ISSN: 1529-6466. DOI: 10.2138/rmg.2006.60.3.

[39] L. L. Hood, D. L. Mitchell, R. P. Lin, M. H. Acuna, and A. B. Binder, "Initial measurements of the lunar induced magnetic dipole moment using lunar prospector magnetometer data", *Geophysical Research Letters*, vol. 26, no. 15, pp. 2327–2330, 1999, ISSN: 1944-8007. DOI: 10.1029/1999GL900487.

[40] Y. Lin, E. J. Tronche, E. S. Steenstra, and W. van Westrenen, "Evidence for an early wet moon from experimental crystallization of the lunar magma ocean", *Nature Geoscience*, vol. 10, no. 1, pp. 14–18, Jan. 2017, ISSN: 1752-0908. DOI: 10.1038/ngeo2845.

[41] J. F. Rapp and D. S. Draper, "Fractional crystallization of the lunar magma ocean: Updating the dominant paradigm", *Meteoritics & Planetary Science*, vol. 53, no. 7, pp. 1432–1455, 2018, ISSN: 1945-5100. DOI: 10.1111/maps.13086.

[42] B. L. Jolliff, J. J. Gillis, L. A. Haskin, R. L. Korotev, and M. A. Wieczorek, "Major lunar crustal terranes: Surface expressions and crust-mantle origins", *Journal of Geophysical Research: Planets*, vol. 105, pp. 4197–4216, E2 2000, ISSN: 2156-2202. DOI: 10.1029/1999JE001103.

[43] C. Frohlich and Y. Nakamura, "The physical mechanisms of deep moonquakes and intermediate-depth earthquakes: How similar and how different?", *Physics of the Earth and Planetary Interiors*, vol. 173, no. 3, pp. 365–374, Apr. 1, 2009, ISSN: 0031-9201. DOI: 10.1016/j.pepi.2009.02.004.

[44] R. C. Weber, P.-Y. Lin, E. J. Garnero, Q. Williams, and P. Lognonné, "Seismic detection of the lunar core", *Science*, vol. 331, no. 6015, pp. 309–312, Jan. 21, 2011. DOI: 10.1126/science.1199375.

[45] I. Matsuyama, F. Nimmo, J. T. Keane, *et al.*, "GRAIL, LLR, and LOLA constraints on the interior structure of the moon", *Geophysical Research Letters*, vol. 43, no. 16, pp. 8365–8375, 2016, ISSN: 1944-8007. DOI: 10.1002/2016GL069952.

[46] L. L. Hood, N. C. Richmond, and P. D. Spudis, "Origin of strong lunar magnetic anomalies: Further mapping and examinations of LROC imagery in regions antipodal to young large impact basins", *Journal of Geophysical Research: Planets*, vol. 118, no. 6, pp. 1265–1284, 2013, ISSN: 2169-9100. DOI: 10.1002/jgre.20078.

[47] L. L. Hood and N. A. Artemieva, "Antipodal effects of lunar basin-forming impacts: Initial 3d simulations and comparisons with observations", *Icarus*, Saturn's Icy Satellites from Cassini, vol. 193, no. 2, pp. 485–502, Feb. 1, 2008, ISSN: 0019-1035. DOI: 10.1016/j.icarus.2007.08.023.

[48] D. H. Needham and D. A. Kring, "Lunar volcanism produced a transient atmosphere around the ancient moon", *Earth and Planetary Science Letters*, vol. 478, pp. 175–178, Nov. 15, 2017, ISSN: 0012-821X. DOI: 10.1016/j.epsl.2017.09.002.

[49] F. S. Johnson, J. M. Carroll, and D. E. Evans, "Lunar atmosphere measurements", in *Lunar and Planetary Science Conference Proceedings*, vol. 3, Jan. 1, 1972, p. 2231.

[50] J. H. Hoffman, R. R. Hodges Jr., F. S. Johnson, and D. E. Evans, "Lunar atmospheric composition results from apollo 17", in *Lunar and Planetary Science Conference Proceedings*, vol. 4, Jan. 1, 1973, p. 2865.

[51] R. R. Hodges Jr., "Helium and hydrogen in the lunar atmosphere", *Journal of Geophysical Research (1896-1977)*, vol. 78, no. 34, pp. 8055–8064, 1973, ISSN: 2156-2202. DOI: 10.1029/JA078i034p08055.

[52] R. C. Elphic, G. T. Delory, B. P. Hine, *et al.*, "The lunar atmosphere and dust environment explorer mission", *The Lunar Atmosphere and Dust Environment Explorer Mission (LADEE)*, R. C. Elphic and C. T. Russell, Eds., pp. 3–25, 2015. DOI: 10.1007/978-3-319-18717-4_2.

[53] M. Benna, P. R. Mahaffy, J. S. Halekas, R. C. Elphic, and G. T. Delory, "Variability of helium, neon, and argon in the lunar exosphere as observed by the LADEE NMS instrument", *Geophysical Research Letters*, vol. 42, no. 10, pp. 3723–3729, 2015, ISSN: 1944-8007. DOI: 10.1002/2015GL064120.

[54] H. A. Zook and J. E. McCoy, "Large scale lunar horizon glow and a high altitude lunar dust exosphere", *Geophysical Research Letters*, vol. 18, no. 11, pp. 2117–2120, 1991, ISSN: 1944-8007. DOI: 10.1029/91GL02235.

[55] M. Horányi, J. R. Szalay, S. Kempf, *et al.*, "A permanent, asymmetric dust cloud around the moon", *Nature*, vol. 522, no. 7556, pp. 324–326, Jun. 2015, ISSN: 1476-4687. DOI: 10.1038/nature14479.

[56] D. H. Wooden, A. M. Cook, A. Colaprete, D. A. Glenar, T. J. Stubbs, and M. Shirley, "Evidence for a dynamic nanodust cloud enveloping the moon", *Nature Geoscience*, vol. 9, no. 9, pp. 665–668, Sep. 2016, ISSN: 1752-0908. DOI: 10.1038/ngeo2779.

[57] J. G. Luhmann, "Plasma interactions with unmagnetized bodies", in *Introduction to space physics*, M. G. Kivelson and C. T. Russell, Eds., Cambridge University Press, 1995, pp. 203–226. DOI: 10.1017/9781139878296.009.

[58] M. Wieser, S. Barabash, Y. Futaana, *et al.*, "Extremely high reflection of solar wind protons as neutral hydrogen atoms from regolith in space", *Planetary and Space Science*, vol. 57, no. 14, pp. 2132–2134, Dec. 1, 2009, ISSN: 0032-0633. DOI: 10.1016/j.pss.2009.09.012.

[59] D. J. McComas, F. Allegrini, P. Bochsler, *et al.*, "Lunar backscatter and neutralization of the solar wind: First observations of neutral atoms from the moon", *Geophysical Research Letters*, vol. 36, no. 12, 2009, ISSN: 1944-8007. DOI: 10.1029/2009GL038794.

[60] H. O. Funsten, F. Allegrini, P. A. Bochsler, *et al.*, "Reflection of solar wind hydrogen from the lunar surface", *Journal of Geophysical Research: Planets*, vol. 118, no. 2, pp. 292–305, 2013, ISSN: 2169-9100. DOI: 10.1002/jgre.20055.

[61] J. S. Halekas, Y. Saito, G. T. Delory, and W. M. Farrell, "New views of the lunar plasma environment", *Planetary and Space Science*, Lunar Dust, Atmosphere and Plasma: The Next Steps, vol. 59, no. 14, pp. 1681–1694, Nov. 1, 2011, ISSN: 0032-0633. DOI: 10.1016/j.pss.2010.08.011.

[62] T. J. Stubbs, J. S. Halekas, W. M. Farrell, and R. R. Vondrak, "LUNAR SURFACE CHARGING: A GLOBAL PERSPECTIVE USING LUNAR PROSPECTOR DATA", p. 5,

[63] J. S. Halekas, D. L. Mitchell, R. P. Lin, L. L. Hood, M. H. Acuña, and A. B. Binder, "Evidence for negative charging of the lunar surface in shadow", *Geophysical Research Letters*, vol. 29, no. 10, pp. 77–1–77–4, 2002, ISSN: 1944-8007. DOI: 10.1029/2001GL014428.

[64] A. R. Poppe, J. S. Halekas, C. Lue, and S. Fatemi, "ARTEMIS observations of the solar wind proton scattering function from lunar crustal magnetic anomalies", *Journal of Geophysical Research: Planets*, vol. 122, no. 4, pp. 771–783, 2017, ISSN: 2169-9100. DOI: 10.1002/2017JE005313.

[65] D. T. Blewett, E. I. Coman, B. R. Hawke, J. J. Gillis-Davis, M. E. Purucker, and C. G. Hughes, "Lunar swirls: Examining crustal magnetic anomalies and space weathering trends", *Journal of Geophysical Research: Planets*, vol. 116, E2 2011, ISSN: 2156-2202. DOI: 10.1029/2010JE003656.

[66] M. Wieser, S. Barabash, Y. Futaana, *et al.*, "First observation of a mini-magnetosphere above a lunar magnetic anomaly using energetic neutral atoms", *Geophysical Research Letters*, vol. 37, no. 5, 2010, ISSN: 1944-8007. DOI: 10.1029/2009GL041721.

[67] R. P. Lin, D. L. Mitchell, D. W. Curtis, *et al.*, "Lunar surface magnetic fields and their interaction with the solar wind: Results from lunar prospector", *Science*, vol. 281, no. 5382, pp. 1480–1484, Sep. 4, 1998, ISSN: 0036-8075, 1095-9203. DOI: 10.1126/science.281.5382.1480.

[68] S. Fatemi, H. A. Fuqua, A. R. Poppe, *et al.*, "On the confinement of lunar induced magnetic fields", *Geophysical Research Letters*, vol. 42, no. 17, pp. 6931–6938, 2015, ISSN: 1944-8007. DOI: 10.1002/2015GL065576.

[69] Y. Futaana, S. Barabash, M. Wieser, *et al.*, "Remote energetic neutral atom imaging of electric potential over a lunar magnetic anomaly", *Geophysical Research Letters*, vol. 40, no. 2, pp. 262–266, 2013, ISSN: 1944-8007. DOI: 10.1002/grl.50135.

[70] H. Fuqua Haviland, A. R. Poppe, S. Fatemi, G. T. Delory, and I. d. Pater, "Time-dependent hybrid plasma simulations of lunar electromagnetic induction in the solar wind", *Geophysical Research Letters*, vol. 46, no. 8, pp. 4151–4160, 2019, ISSN: 1944-8007. DOI: 10.1029/2018GL080523.

[71] P. C. Birch and S. C. Chapman, "Particle-in-cell simulations of the lunar wake with high phase space resolution", *Geophysical Research Letters*, vol. 28, no. 2, pp. 219–222, 2001, ISSN: 1944-8007. DOI: 10.1029/2000GL011958.

[72] N. Borisov and U. Mall, "Plasma distribution and electric fields behind the moon", *Physics Letters A*, vol. 265, no. 5, pp. 369–376, Feb. 7, 2000, ISSN: 0375-9601. DOI: 10.1016/S0375-9601(99)00852-X.

[73] J. B. Tao, R. E. Ergun, D. L. Newman, *et al.*, "Kinetic instabilities in the lunar wake: ARTEMIS observations", *Journal of Geophysical Research: Space Physics*, vol. 117, A3 2012, ISSN: 2156-2202. DOI: 10.1029/2011JA017364.

[74] C. B. Haakonsen, I. H. Hutchinson, and C. Zhou, "Kinetic electron and ion instability of the lunar wake simulated at physical mass ratio", *Physics of Plasmas*, vol. 22, no. 3, p. 032 311, Mar. 1, 2015, ISSN: 1070-664X. DOI: 10.1063/1.4915525.

[75] W. M. Farrell, M. L. Kaiser, and J. T. Steinberg, "Electrostatic instability in the central lunar wake: A process for replenishing the plasma void?", *Geophysical Research Letters*, vol. 24, no. 9, pp. 1135–1138, 1997, ISSN: 1944-8007. DOI: 10.1029/97GL00878.

[76] M. N. Nishino, M. Fujimoto, Y. Saito, *et al.*, "Effect of the solar wind proton entry into the deepest lunar wake", *Geophysical Research Letters*, vol. 37, no. 12, 2010, ISSN: 1944-8007. DOI: 10.1029/2010GL043948.

[77] S. Fatemi, M. Holmström, Y. Futaana, *et al.*, "Effects of protons reflected by lunar crustal magnetic fields on the global lunar plasma environment", *Journal of Geophysical Research: Space Physics*, vol. 119, no. 8, pp. 6095–6105, 2014, ISSN: 2169-9402. DOI: 10.1002/2014JA019900.

[78] P. C. Birch and S. C. Chapman, "Correction to "particle-in-cell simulations of the lunar wake with high phase space resolution"", *Geophysical Research Letters*, vol. 28, no. 13, pp. 2669–2669, Jul. 1, 2001, ISSN: 0094-8276. DOI: 10.1029/2001GL012961.

[79] P. C. Birch and S. C. Chapman, "Two dimensional particle-in-cell simulations of the lunar wake", *Physics of Plasmas*, vol. 9, no. 5, pp. 1785–1789, May 1, 2002, ISSN: 1070-664X. DOI: 10.1063/1.1467655.

[80] D. Lund, J. Zhao, A. Lamb, and D. Han, "Fully kinetic PIFE-PIC simulations of plasma charging at lunar craters", in *AIAA Scitech 2020 Forum*, American Institute of Aeronautics and Astronautics. DOI: 10.2514/6.2020-1549.

[81] L. Xie, L. Li, Y. Zhang, and D. L. De Zeeuw, "Three-dimensional MHD simulation of the lunar wake", *Science China Earth Sciences*, vol. 56, no. 2, pp. 330–338, Feb. 1, 2013, ISSN: 1869-1897. DOI: 10.1007/s11430-012-4383-6.

[82] P. Trávníček, P. Hellinger, D. Schriver, and S. D. Bale, "Structure of the lunar wake: Two-dimensional global hybrid simulations", *Geophysical Research Letters*, vol. 32, no. 6, 2005, ISSN: 1944-8007. DOI: 10.1029/2004GL022243.

[83] P. Trávníček, P. Hellinger, and D. Schriver, "Structure of mercury's magnetosphere for different pressure of the solar wind: Three dimensional hybrid simulations", *Geophysical Research Letters*, vol. 34, no. 5, 2007, ISSN: 1944-8007. DOI: 10.1029/2006GL028518.

[84] M. Holmstrom and B. Eliasson, "Modeling the lunar plasma wake", *arXiv:1301.0198 [physics]*, Jan. 2, 2013. arXiv: 1301.0198.

[85] S. Fatemi, M. Holmström, Y. Futaana, S. Barabash, and C. Lue, "The lunar wake current systems", *Geophysical Research Letters*, vol. 40, no. 1, pp. 17–21, 2013, ISSN: 1944-8007. DOI: 10.1029/2012GL054635.

[86] Y. Vernisse, H. Kriegel, S. Wiehle, U. Motschmann, and K. H. Glassmeier, "Stellar winds and planetary bodies simulations: Lunar type interaction in super-alfvénic and sub-alfvénic flows", *Planetary and Space Science*, vol. 84, pp. 37–47, Aug. 1, 2013, ISSN: 0032-0633. DOI: 10.1016/j.pss.2013.04.004.

[87] M. Holmström, M. Wieser, S. Barabash, Y. Futaana, and A. Bhardwaj, "Dynamics of solar wind protons reflected by the moon", *Journal of Geophysical Research: Space Physics*, vol. 115, A6 2010, ISSN: 2156-2202. DOI: 10.1029/2009JA014843.

[88] A. P. Matthews, "Current advance method and cyclic leapfrog for 2d multispecies hybrid plasma simulations", *Journal of Computational Physics*, vol. 112, no. 1, pp. 102–116, May 1, 1994, ISSN: 0021-9991. DOI: 10.1006/jcph.1994.1084.

[89] M. Holmstrom, "Handling vacuum regions in a hybrid plasma solver", *arXiv:1301.0272 [physics]*, Jan. 2, 2013. arXiv: 1301.0272.

[90] A. S. Lipatov, *The hybrid multiscale simulation technology: an introduction with application to astrophysical and laboratory plasmas* (Scientific computation). Berlin ; New York: Springer, 2002, 403 pp., ISBN: 978-3-540-41734-7.

[91] S. Fatemi, C. Lue, M. Holmström, *et al.*, "Solar wind plasma interaction with gerasimovich lunar magnetic anomaly", *Journal of Geophysical Research: Space Physics*, vol. 120, no. 6, pp. 4719–4735, 2015, ISSN: 2169-9402. DOI: 10.1002/2015JA021027.

[92] D. Procházka, "Elektromagnetické vlastnosti měsíců a planet", Research Assignment, Czech Technical University in Prague, Prague, 2021.

[93] L. Gomberoff and J. A. Valdivia, "Ion cyclotron instability due to the thermal anisotropy of drifting ion species", *Journal of Geophysical Research: Space Physics*, vol. 108, A1 2003, ISSN: 2156-2202. DOI: 10.1029/2002JA009576.

Appendix A

Figures

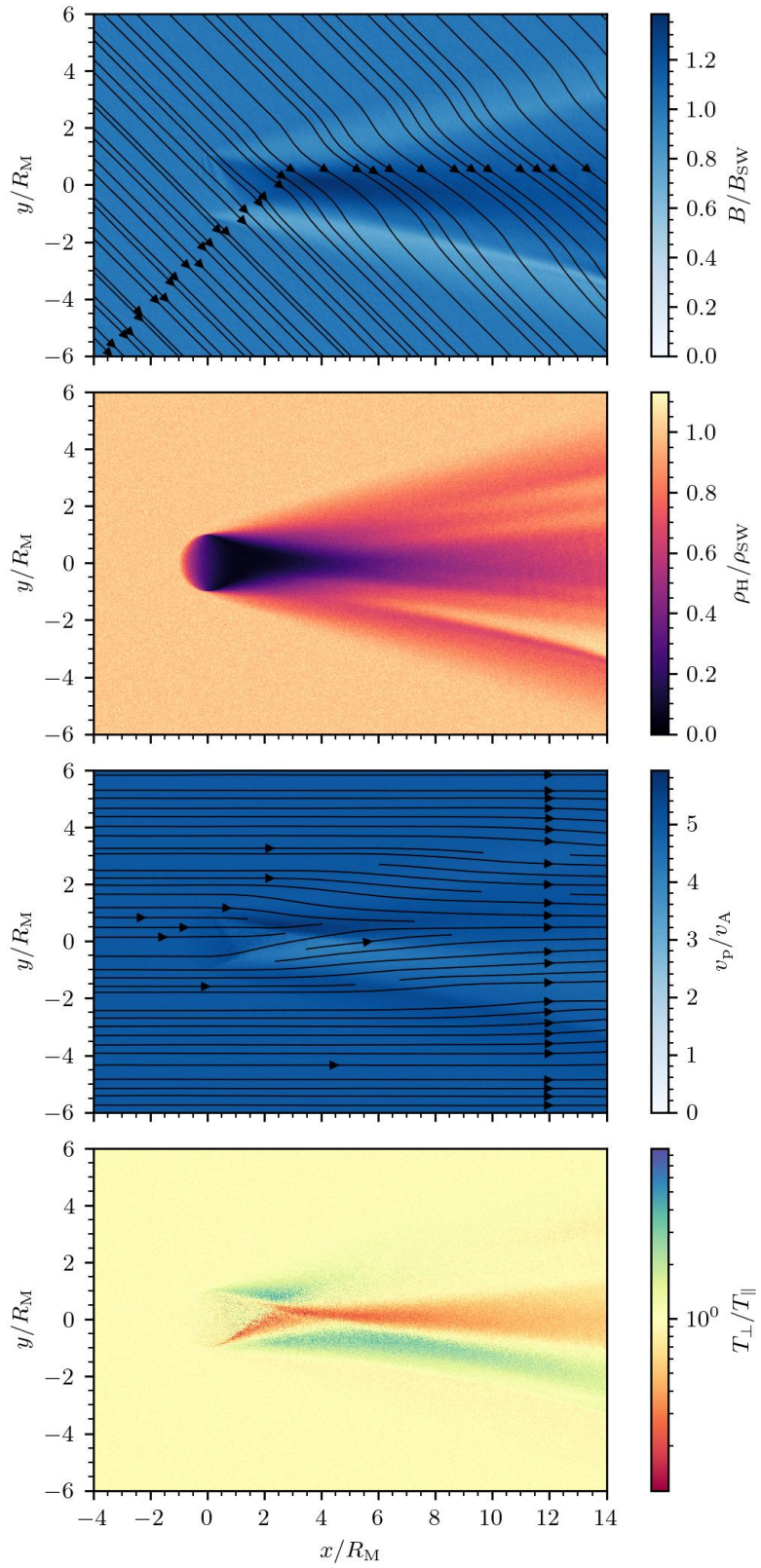

Figure A.1: Quantities (part A) at $t = 50\Omega_p^{-1}$ in the reference simulation run.

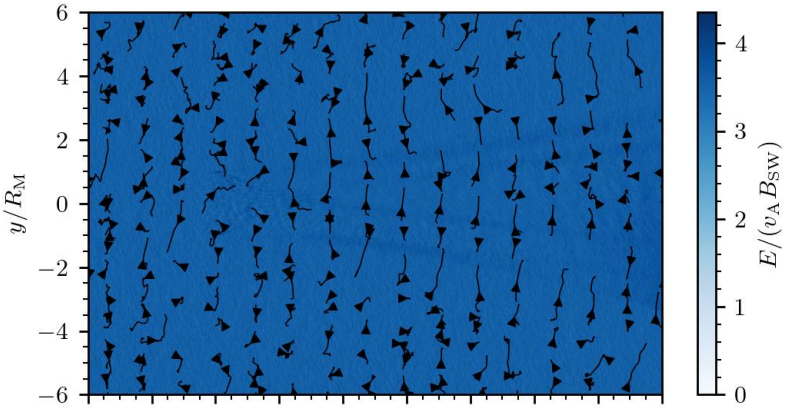

Figure A.2: Quantities (part B) at $t = 50\Omega_p^{-1}$ in the reference simulation run.

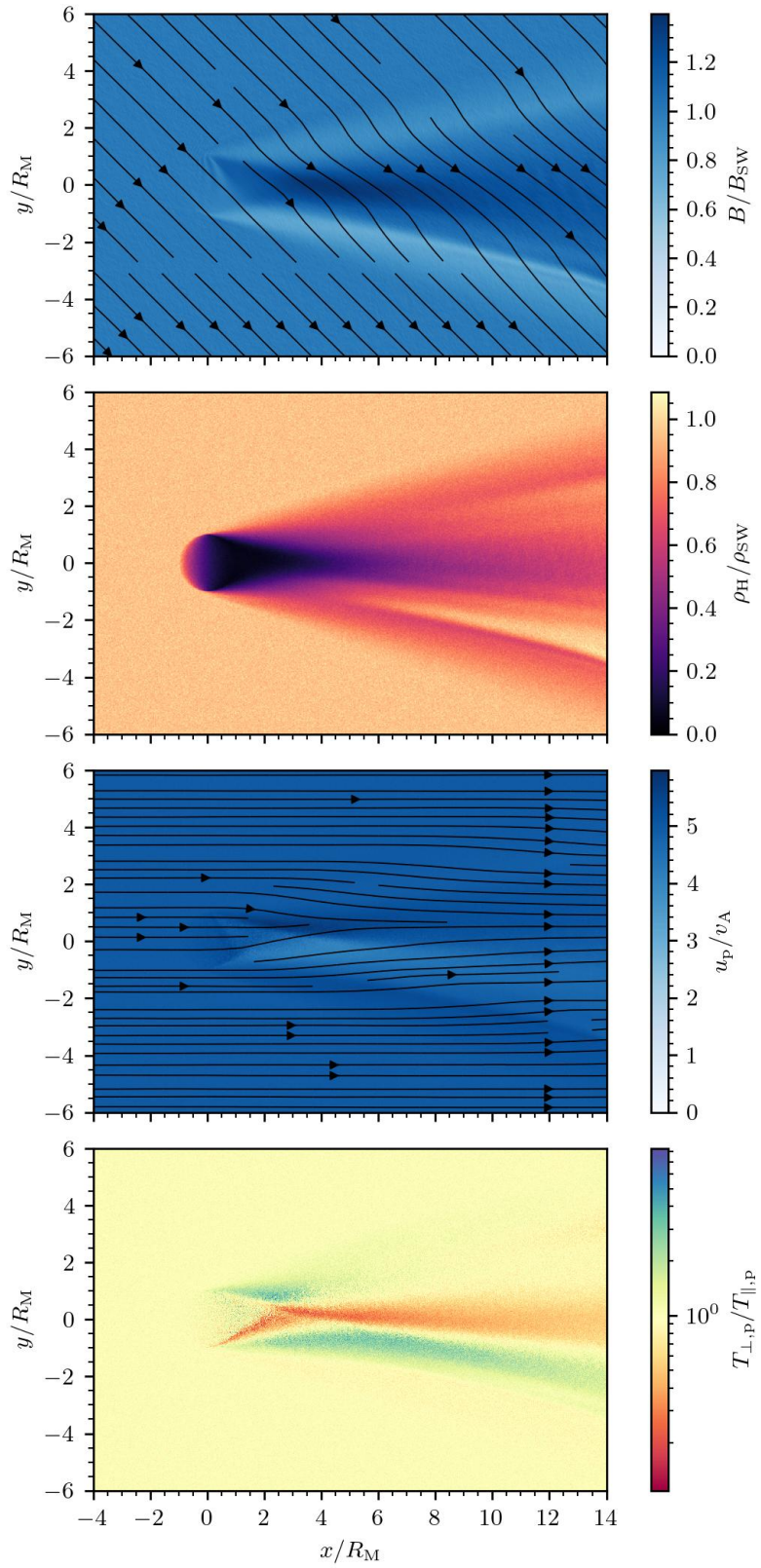

Figure A.3: Quantities (part A) at $t = 50\Omega_\mathrm{p}^{-1}$ in simulation run 1.

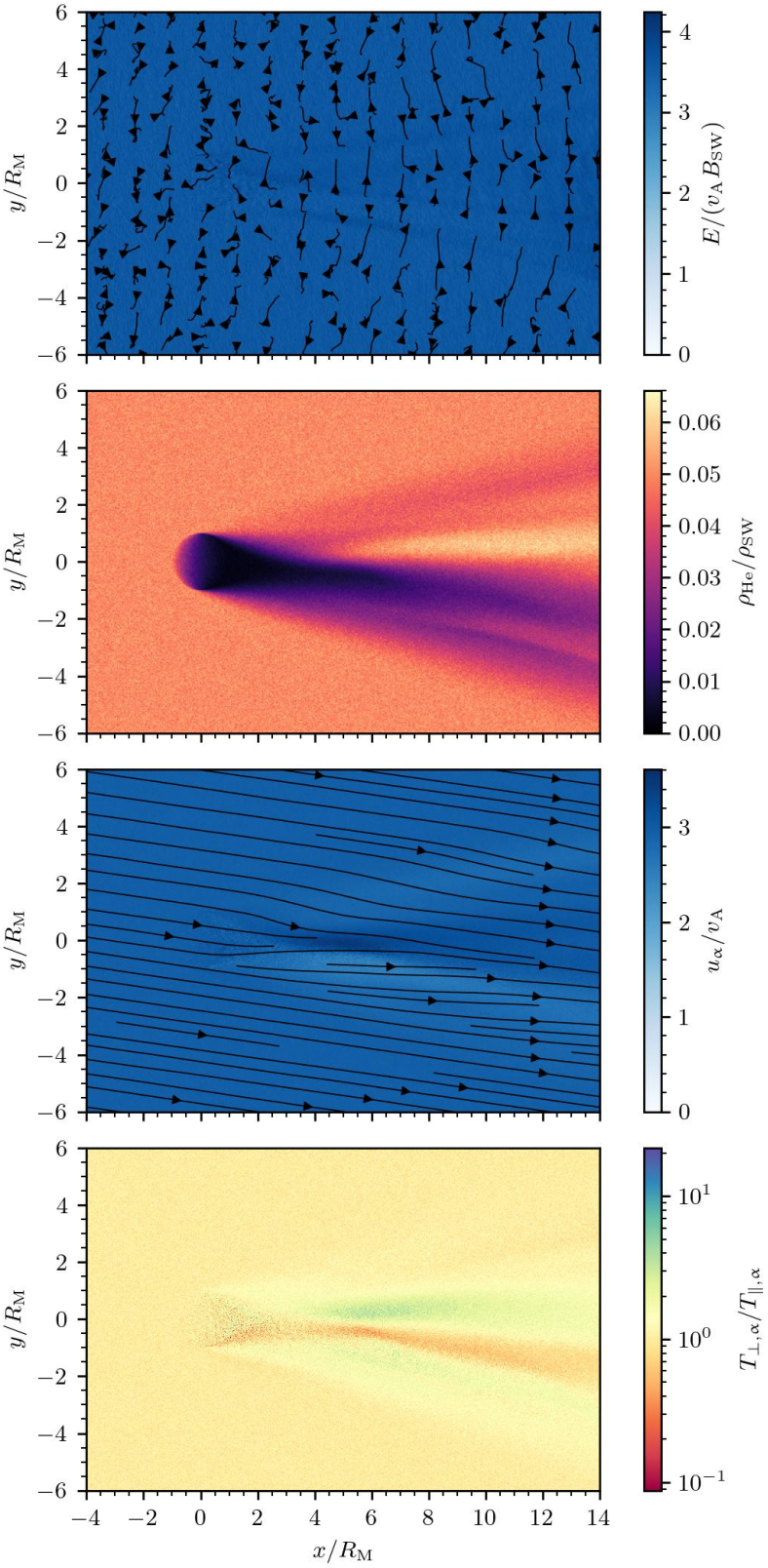

Figure A.4: Quantities (part B) at $t = 50\Omega_\mathrm{p}^{-1}$ in simulation run 1.

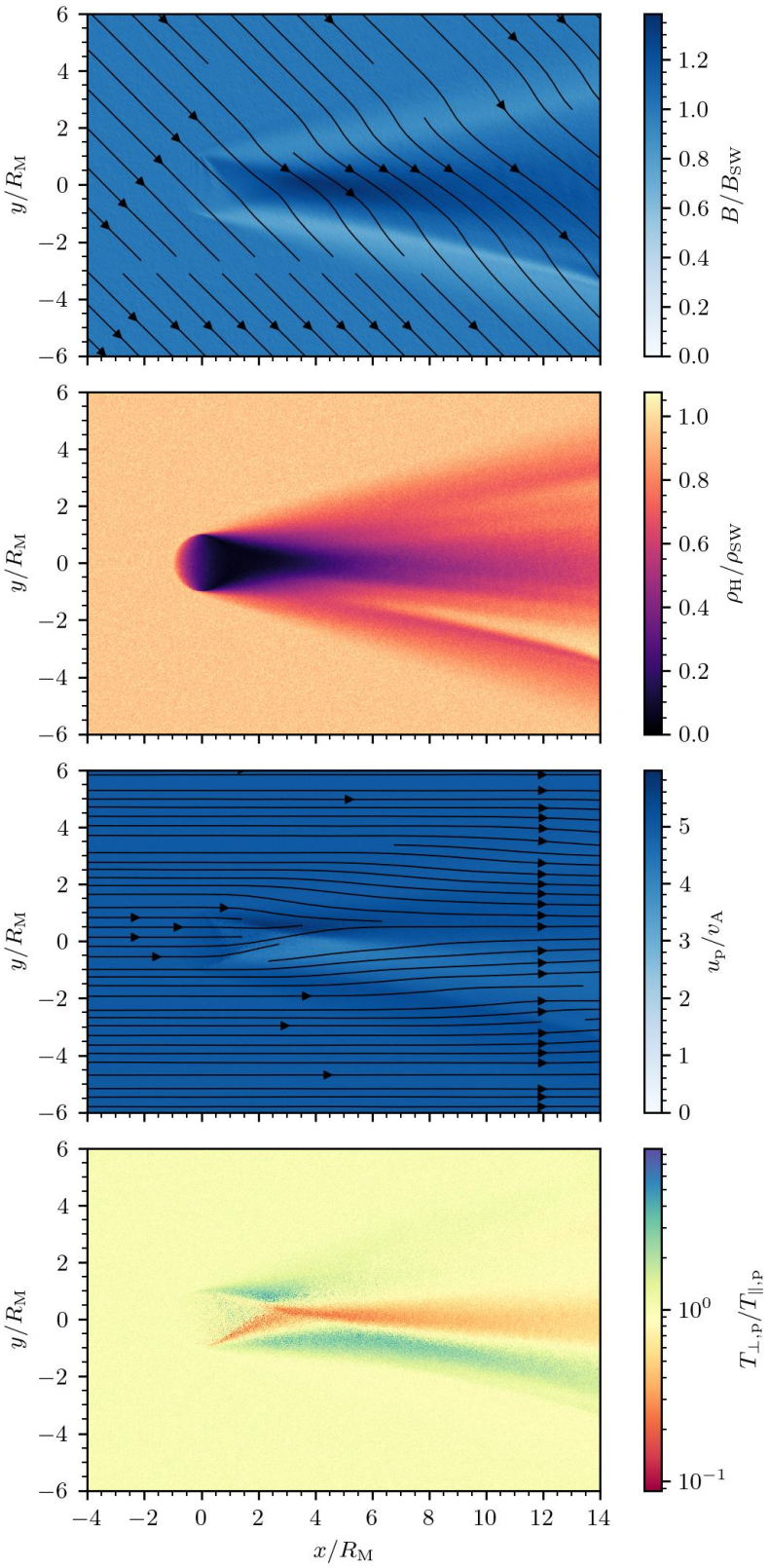

Figure A.5: Quantities (part A) at $t = 50\Omega_\mathrm{p}^{-1}$ in simulation run 2.

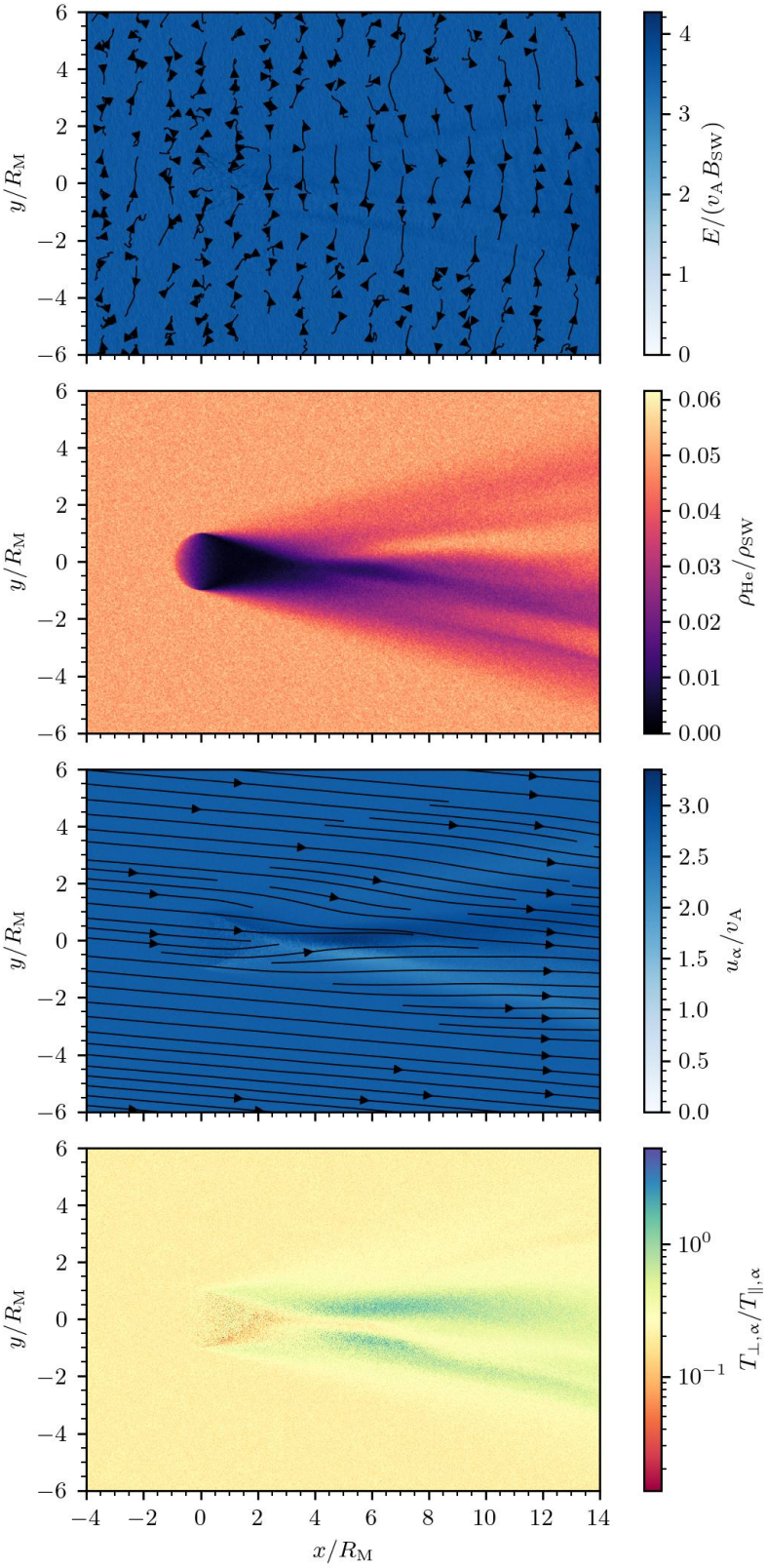

Figure A.6: Quantities (part B) at $t = 50\Omega_\mathrm{p}^{-1}$ in simulation run 2.

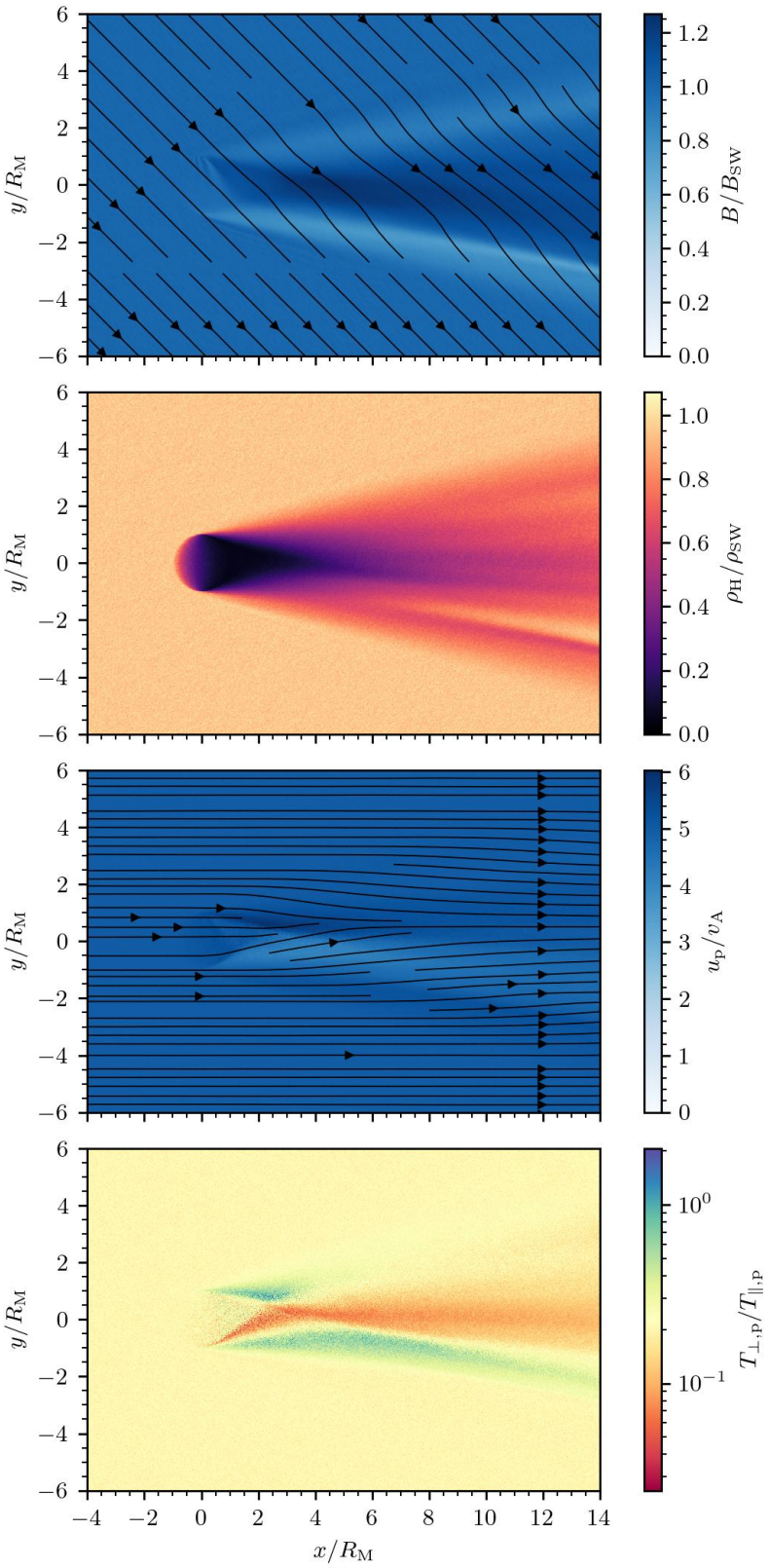

Figure A.7: Quantities (part A) at $t = 50\Omega_\mathrm{p}^{-1}$ in simulation run 3.

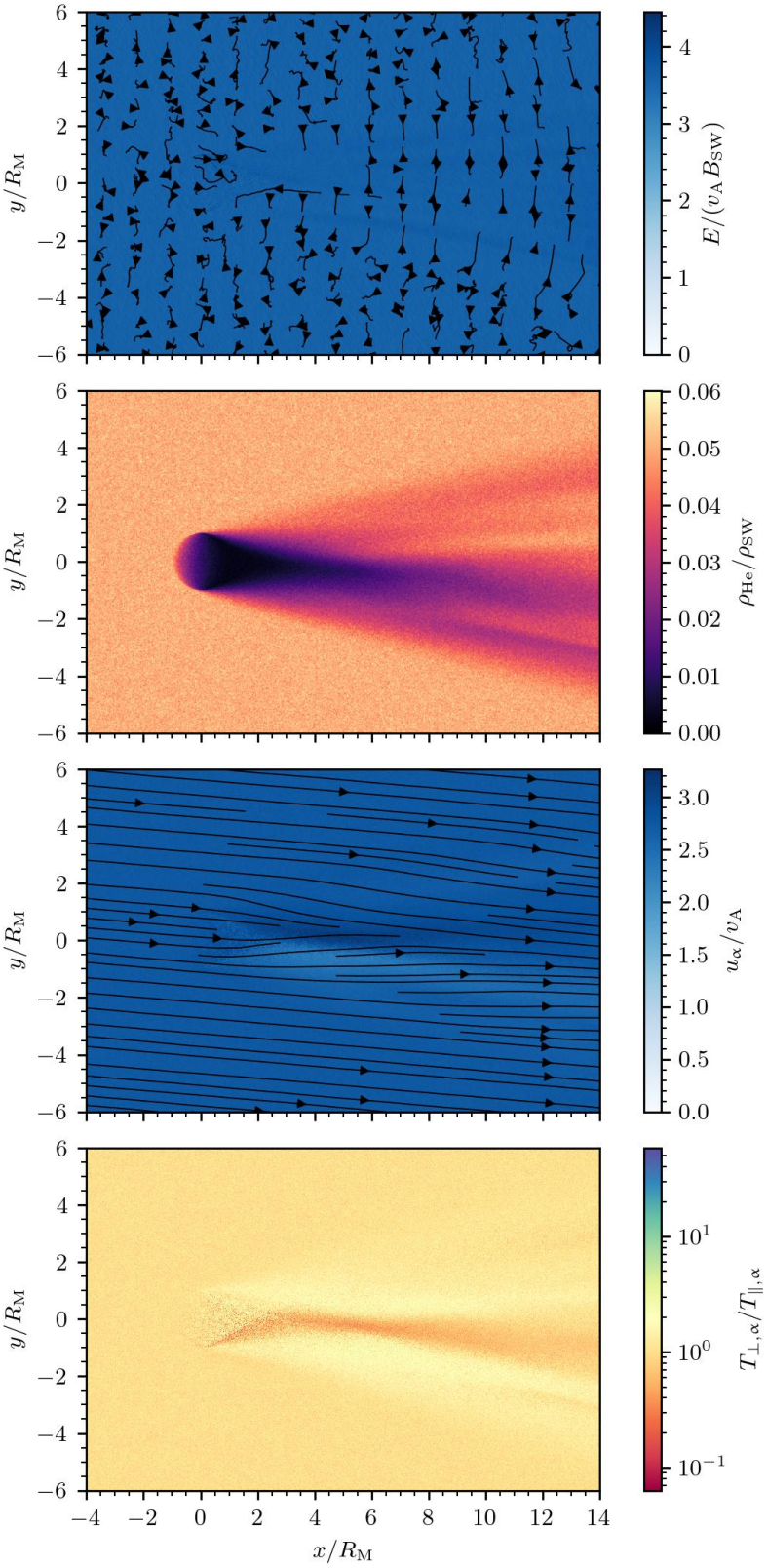

Figure A.8: Quantities (part B) at $t = 50\Omega_\mathrm{p}^{-1}$ in simulation run 3.

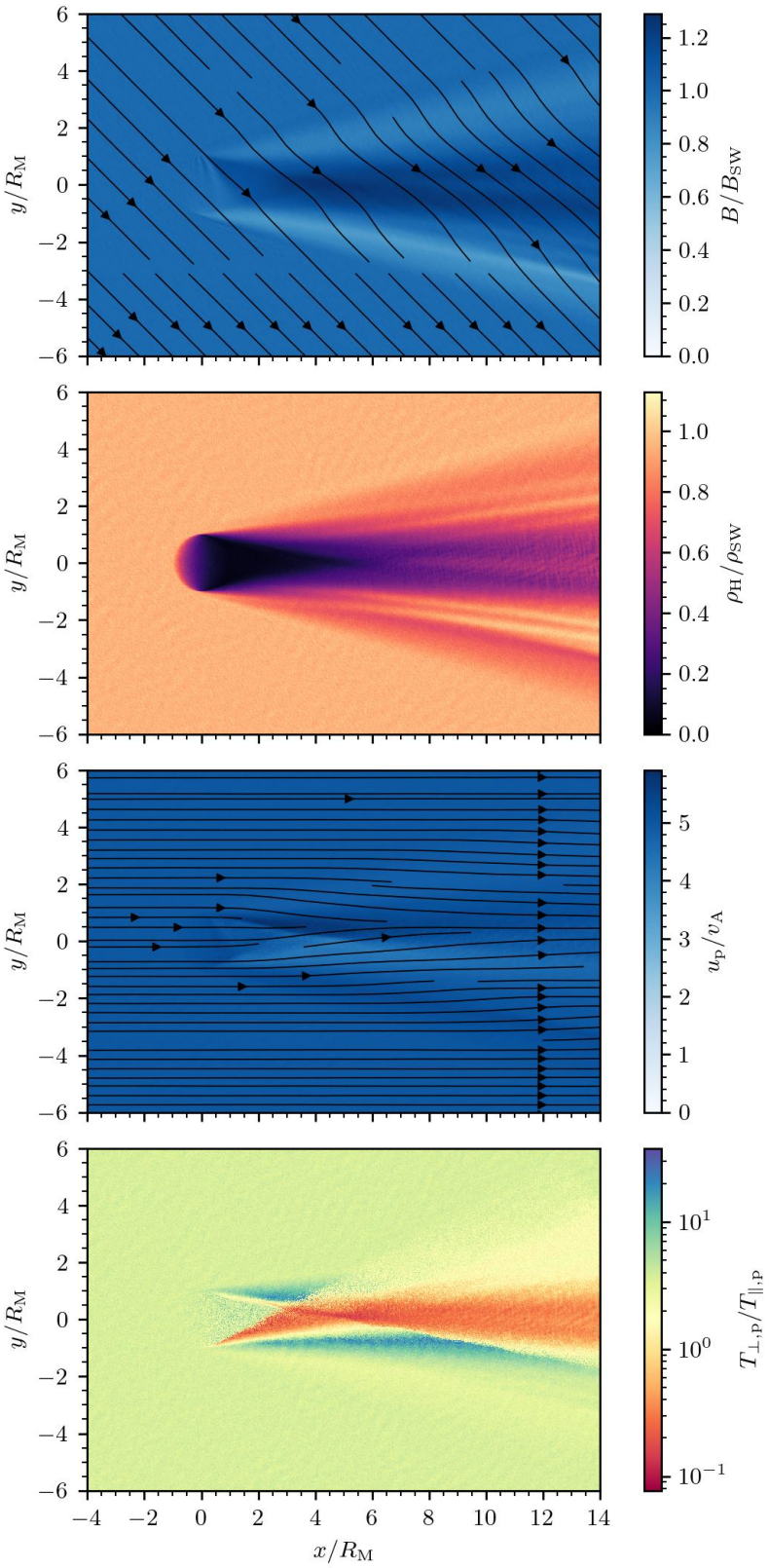

Figure A.9: Quantities (part A) at $t = 50\Omega_\mathrm{p}^{-1}$ in simulation run 4.

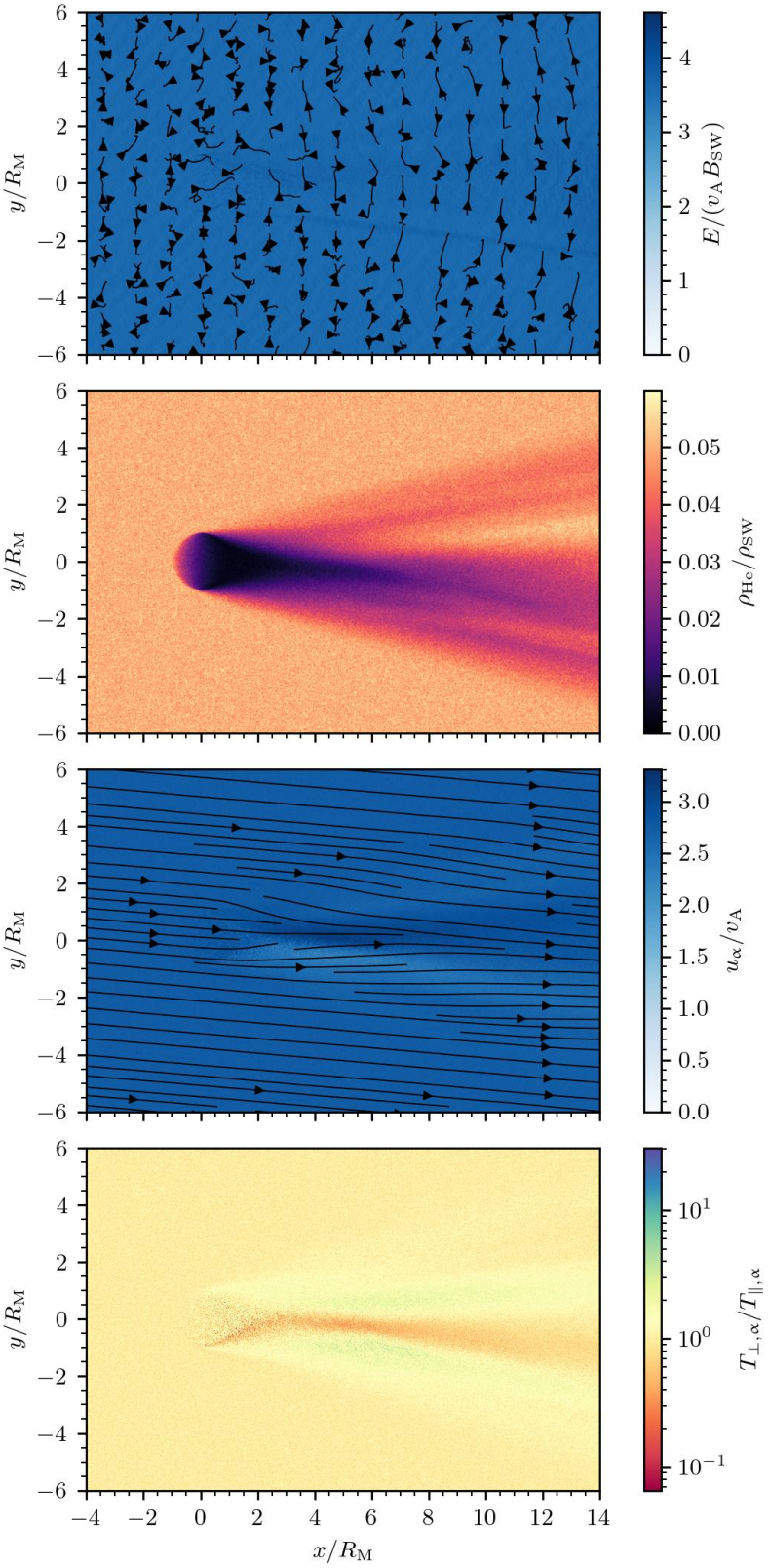

Figure A.10: Quantities (part B) at $t = 50\Omega_\mathrm{p}^{-1}$ in simulation run 4.

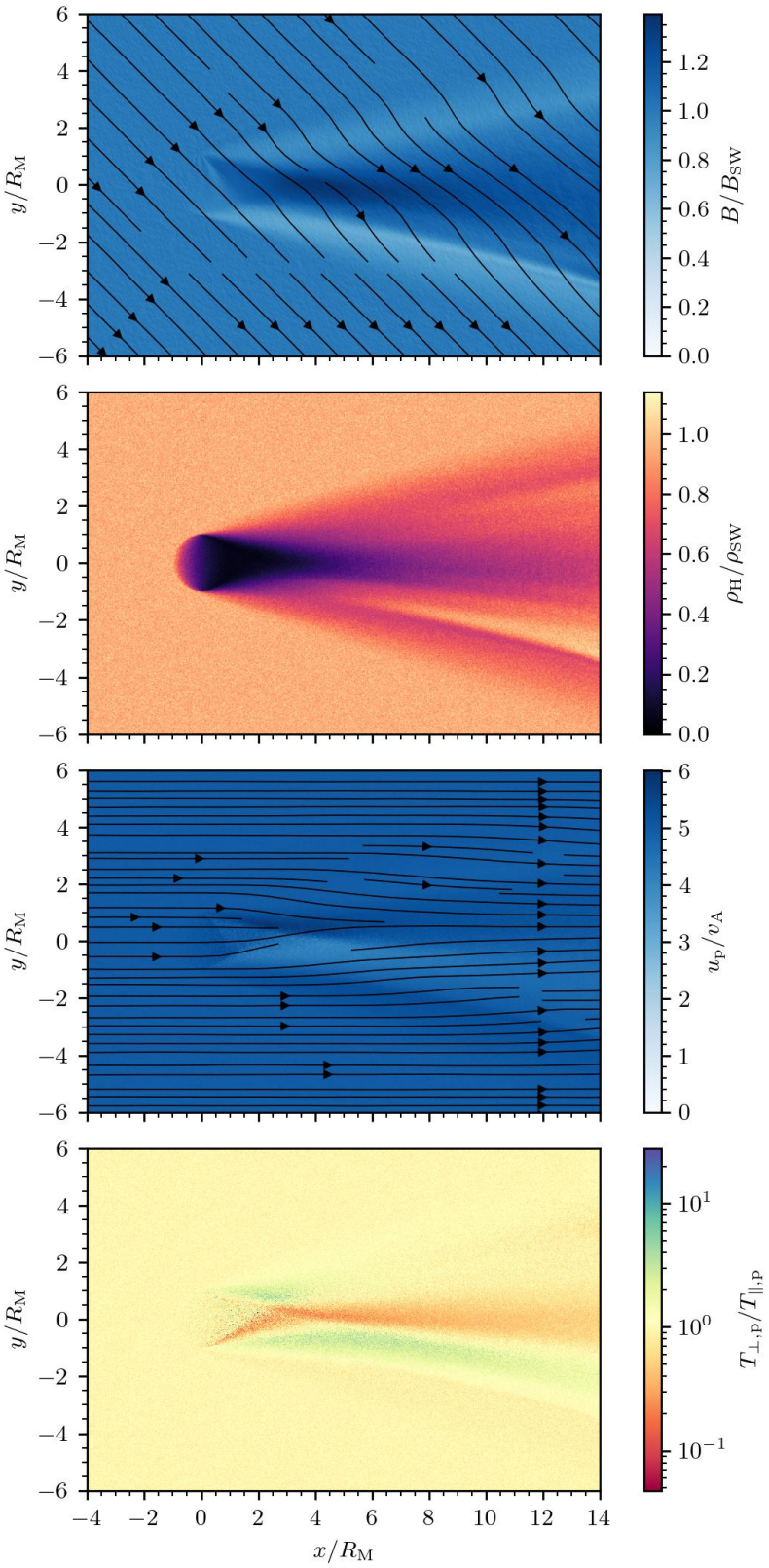

Figure A.11: Quantities (part A) at $t = 50\Omega_\mathrm{p}^{-1}$ in simulation run 5.

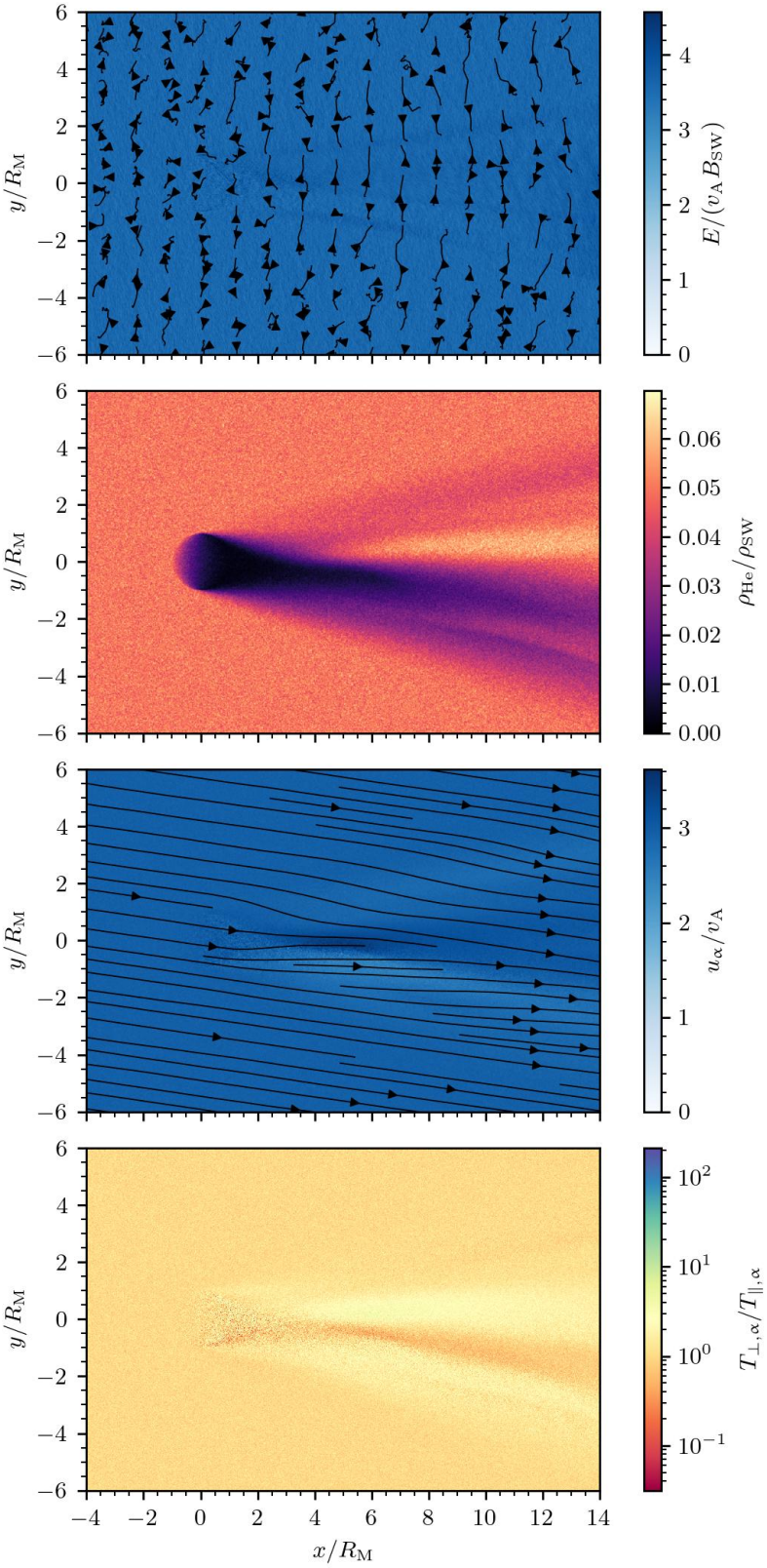

Figure A.12: Quantities (part B) at $t = 50\Omega_\mathrm{p}^{-1}$ in simulation run 5.